UNIVERSITY OF HULL

# Light Matter interaction in hybrid plasmonic/photonic nanogaps

being a thesis submitted in fulfilment of the

requirements for the degree of Doctor of Philosophy (Physics)

in the University of Hull

by

Francesco Viscomi

August 2020

# Declaration of Authorship

I declare that all the work presented in this thesis is my own original work. Where I have used results from other researchers, they have been acknowledged for their work. Some of the work has been published in the following journal articles and conference presentations.

# Acknowledgements

I would like to first acknowledge my supervisor Dr. Jean-Sebastien Bouillard, who has supported and motivated me throughout my PhD. His brilliant suggestions made me keep going even when I was close to quitting. I will always remember you like an older brother.

I would also like to thank my co supervisor Dr. Ali Adawi for keeping me on track, despite the various derailments, and making able to produce some science. I am going to remember you like an uncle. I want to thank you both supervisors for the trust you had in me since day 1 and for writing lots of projects (often at night) to buy the equipment. I could not play with all of those “expensive toys” without you and your sleepless nights.

Thank you to the collaborators from Chemistry to Dr. Graeme Stasiuk and to Mitchell Clarke for involving me in that brilliant study about ultra-bright quantum dots.

Thank you to the collaborators Dr. Pan Wang and Dr. Alexey Krasavin from Prof. Anatoly Zayats’s group at Kings College London for the collaboration on spherical metaparticles.

A big thank you to all the LNIO members for being great hosts, fine scientific advisors and friends during my brief staying at the LNIO at the UTT in France. Your incredible knowledge of optics and exquisite hospitality will never be forgotten.

A separate thank you to all the LNIO staff for welcoming me again, to the 3 lab technicians Regis Deturche, Sergei Kostcheev and Jeremie Beal. Your impressive technical skills helped me quite a lot. Working beside you in that magnificent clean room has been a pleasure and an honour.

I also thank all the postgraduate students I have lived the whole PhD adventure; Arina Mohammed, Andrew Clarke, Qassim Al-Jarwany and Alex Bridgwater, Addison Marshall.

To the two brilliant project students I had the privilege to assist: Daniel and Jonathan. Plus, our project visitor student from France Florian.

To the students I have interacted the most:

Alex Gee for all the chit chat, cups of tea, electronics and Shed heads…

Abdullah O’Hamza and Family. For being simply my Brother Peshmerga.

Jack Eden for all the AHH GRAYYYYYYY and fine conversations about spirits and lasers.

Charlotte Eling for all the great time spent both in the lab and outside. You are one of the reasons that kept me sane during this year.

To my great friend Donatello and his wife Anna for being amazing friends and sharing a little bit of Italy while in Hull.

To Scientifica Ltd for offering me a job related to my skillset and study path when I was on the verge of a financial breakdown. Thank you for trusting me building amazing microscopes and for letting me travel across Australia, Chile, China, India, Canada, USA, and Europe, just to cite few. A special thanks to all my current teammates: Ben, Lionel, Reetu, Zuzana, Michael, Joe, Marco, Stefan, Victor, and the previous members for making my office days very enjoyable.

To my co-worker and compatriot Michelangelo Colavita for being there during operation UK20592 in Michigan, those 5 days, and nights of hard work with you count more than this whole manuscript.

To Alex Stratton the travel agent who has been looking after me in the past 2 years and almost never letting me down… Except those times in Beijing, Burlington, New York, Brisbane… I am just joking Alex.

To my high school math teacher Anna Paola Nicotra for, literally, forcing me to study physics and not geology. All of this could not happen without you. Not like that “grandissimo coglione” of the Latin teacher.

To the Websters for being great housemates in the past two years. Thank you, Lou, Sam, Fin and Beth, for tolerating me and looking after me during the covid19 quarantine. Without forgetting Sophie, the dog and Beeno the cat.

Thank you to my parents Antonio and Teresa, my cheeky liberal sister Maria Pia, my loud Italian extend family and my slightly quieter Canadian one for supporting me during these five years.

# Abstract

The aim of this thesis is to study the processes of light matter interaction at the nanoscale in hybrid nano gaps that are made from both metals and dielectrics. This approach enables the possibility to use both the optical properties of a dielectric, such as low losses and high-quality factor, with the small mode volume typical of a metal. High quality factor and small modal volume together make a high Purcell factor, which is the enhancement of the spontaneous emission rate due to the surrounding cavity environment. Both the size and the time scales involved in this study range in the nanometre and nano second, respectively.

The architecture used for the study of the hybrid nano gaps consists of a substrate containing a Distributed Bragg Reflector (DBR) and a 10 nm thick emitting layer. On top of this layer lies a small concentration of gold nano spheres. Two different emitting dipole orientations have been studied, vertical and horizontal. The vertical orientation is parallel to the nano gap dipole moment while in the case of the horizontal orientation, it is perpendicular to it. These two emitting dipole orientations have been used to perform two different experiments exploiting different properties of the DBR. DBRs have been used for two purposes, reflectors and 1-d photonic crystals. These two applications are used to investigate different properties of the hybrid nano gaps. Indeed, DBRs have a highly reflective spectral region called photonic stopband, outside of it there are some highly localised reflectivity minima called Bragg modes.

The first hybrid nano gap application explored is the directional nano antenna. In this approach the DBR is used as a reflector and the nano cavity is used to control the direction of the emission. Because of the Fermi golden rule, the dipole moment of the emitter and the nano gap must be parallel to achieve the largest coupling possible. The dipole orientation parallel to the cavity dipole moment is called vertical and it has been probed using the emitter Lumogen Red. This dye exhibits a high quantum yield, low photo bleaching and a good vertical orientability when spun on a surface in form of a film. In this configuration, the light is emitted by the layer at very large angle compared to the surface, roughly 60 degrees. The system can measure up to 64 degrees since the objective numerical aperture is 0.9/1. In this nanogap the nanoparticle acts like a directional antenna and 65% of the emitted light gets redirected at angles not accessible by emitters on their own. Spectrally dispersed k-space imaging has been used to perform such a measurement. This study has demonstrated how the light emission cone is a function of the nano particle size. The narrowest emission cone observed was found to occur for a 500 nm diameter particle size. This configuration showed an enhancement emission factor ranging from 30 up to 60.

The second nano gap configuration used the DBR as photonic crystal to achieve localised Tamm plasmon generation. These results are described in chapter 6. The minimum in the reflectivity spectrum of the DBR is called the 1$^{st}$ Bragg mode. In this mode the impinging radiation can penetrate inside the stack and not propagate outside. Tamm states are surface states that can be excited at the interface between a DBR stack and a metal film. Super Tamm are more localised Tamm states that can be excited only by replacing the metallic film with a finite structure such as a micro disk. In this thesis, a new form of localised super Tamm states has been excited. This novelty state has been named Isolated super Tamm modes. The disk has been replaced with a gold nano sphere. Isolated super Tamm modes have been proved to have an intermediate spectral position between the 1$^{st}$ Bragg mode and the super Tamm .

.

# Publications and Conferences

(1) Wang, P.; Krasavin, A. V; Viscomi, F. N.; Adawi, A. M.; Bouillard, J. G.; Zhang, L.; Roth, D. J.; Tong, L.; Zayats, A. V. Metaparticles : Dressing Nano-Objects with a Hyperbolic Coating. 2018, 1800179, 1–10.

(2) Marshall, A. R. L.; Stokes, J.; Viscomi, F. N.; Proctor, J. E.; Gierschner, J.; Bouillard, J.-S.; Adawi, A. Determining Molecular Orientation via Single Molecule SERS in a Plasmonic Nano-Gap. Nanoscale 2017, 17415–17421.

(3) Eling, C. J.; Price, T. W.; Marshall, A. R. L.; Viscomi, F N. A Dual-Modal SERS / Fluorescence Gold Nanoparticle Probe for Mitochondrial Imaging. 2017, 1–8.

(4) Clarke, M. T.; Viscomi, F. N.; Chamberlain, T. W.; Hondow, N.; Adawi, A. M.; Sturge, J.; Erwin, S. C.; Bouillard, J. S. G.; Tamang, S.; Stasiuk, G. J. Synthesis of Super Bright Indium Phosphide Colloidal Quantum Dots through Thermal Diffusion. Commun. Chem. 2019, 2.

(5) Abdullah O Hamza , Francesco N Viscomi , Jean-Sebastien G Bouillard , Ali M Adawi . Foster resonance energy transfer and the local density of states in plasmonics nanogaps. J Phys Chem Lett. 2021 Feb 11;12(5):1507-1513

Posters and talks.

- Light matter interaction in a hybrid photonic-plasmonic nano-gap. SPP8 conference May 22nd -27th, Taipei, Taiwan.
- COST MEETING IC1208 MCM07 &WG MEETING Integrating devices and materials: A challenge for new instrumentation in ICT, 15th -16th April 2016, Vilnius, Lithuania.

# Contents

# Chapter 1 THEORY

## 1.1 GENERAL INTRODUCTION

In the fourth century BC, a unique wine glass was created in the Roman Empire. Known as the Lycurgus Cup and currently hosted at the British Museum, the glass is known for its dichroism -- its colour changes between green and red depending on whether it is observed under light transmission or reflection. Several centuries later, the magnificent multicoloured stained glass windows of Notre Dame and other cathedrals appeared, building upon earlier examples of dichroic glass like the Lycurgus Cup. These spectacular colour effects are due to nano- and microparticles of noble metals such as gold and silver dispersed throughout the glass. This early nanotechnology has evolved into the field of optics research referred to as plasmonics. Currently, a vast range of applications that utilize plasmonic effects are found in science, such as the Surface Enhanced Raman Spectroscopy technique used in the production of rapid pregnancy tests. When light interacts with the surface of a metal, under suitable conditions, it can generate collective in phase oscillations of the free electrons. This collective oscillation is called surface plasmon [1]. Several hybrid systems have been published combining plasmonic nanoparticles with other materials such as liquid crystals [2], polymers [3], [4], [5], biomolecules [6]-[7], semiconductor quantum dots [8]-[9], organic dyes [10]-[11]-[12] or inorganic compounds [13]. In this chapter, we are going to discuss the basics behind plasmonics, starting with some of the principles of electrodynamics such as radiative and non-radiative damping and phase retardation effects. Mathematical expressions for the near field and scattering/absorption cross sections are explained as well. The second part of the chapter is more focused on the interaction between plasmonic nanoparticles and a quantum emitter leading to the Fermi golden rule and Purcell factor. Some more complex systems such as plasmonics nano cavities and Tamm plasmons are briefly treated too.

## 1.2 SURFACE PLASMON POLARITONS (SPP)

Surface plasmon polariton (SPPs) are electromagnetic evanescent waves propagating at the interface between a metal and dielectric, arising from the coupling of surface plasmon (SP) and photon [39] [40]. The simplest structure supporting SPPs is a flat interface which separation a semi-infinite loss-less dielectric and semi-infinite metal.

In Figure 1 we have a basic representation of the SPP process. As we can see the field is confined around the interface in the form of propagating wave. At the same time exhibits an exponential decay in the z direction.

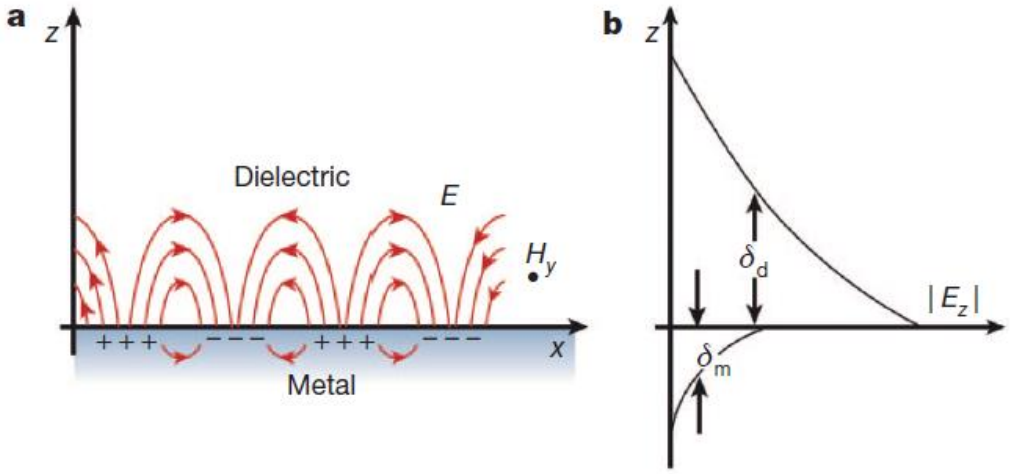


Figure 1 a) Schematic illustration of the propagation of a surface plasmon polariton. b) Field penetration into the materials [41] .

The dispersion relation o is:

$$\omega_{SPP} = \sqrt{\frac{\varepsilon_m + \varepsilon_d}{\varepsilon_m \varepsilon_d}} ck \tag{1}$$

By calculating $\varepsilon_m$ from Drude function for metals Eq. (1) one obtains the dispersion curve for SPPs as shown in Figure 2. We can see as well that the SPP is asymptotic with the surface plasmon frequency and that the dispersion of bulk plasmons lays inside the metal for frequencies higher than the plasma frequency.

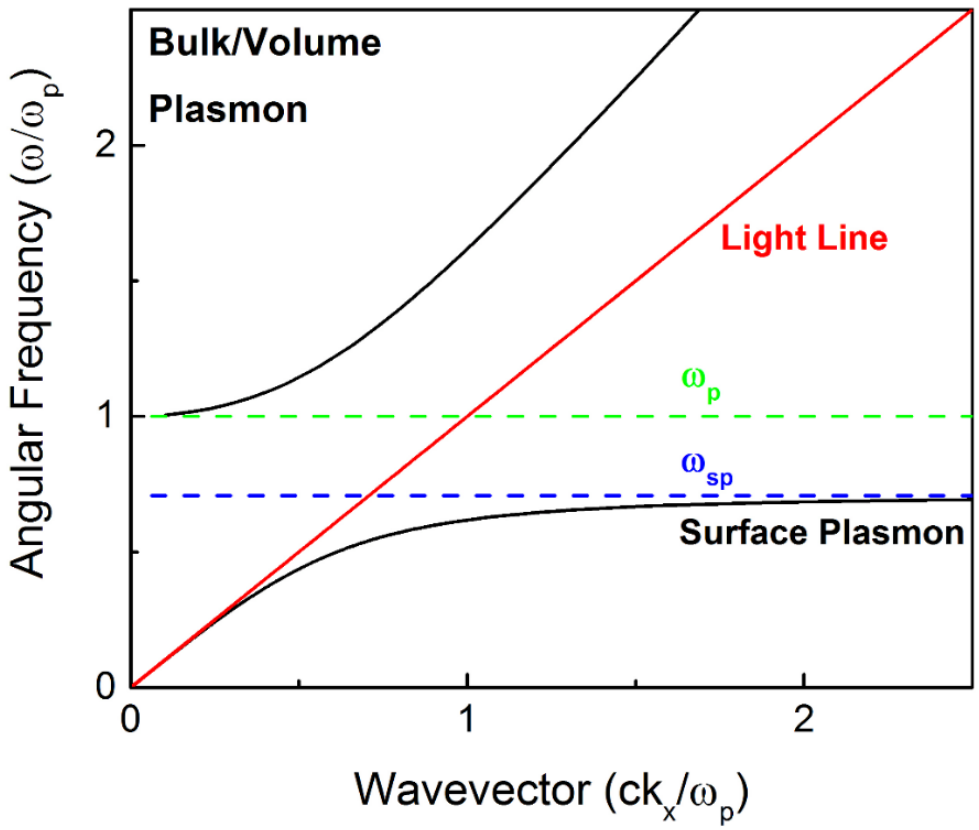


Figure 2: Representation of the dispersion curves for bulk plasmon (black line), light in vacuum (red line) and SPP (black line). The frequencies of the bulk plasmon $\omega_p$ and the SP $\omega_{SP}$ are also marked with dashed black lines. From (ref 21) .

So far, the behaviour of surface plasmon into infinite films has been described. When the size of the metal is shrunk to a dimension comparable to the wavelength of the impinging light, a new class of polaritons arise. These are called Localised Surface Plasmons (LSP).

## 1.3 LOCALISED SURFACE PLASMONS

So far, we have treated only surface plasmons taking place into infinite metal surfaces known as propagating SPP. When the surface is finite, the surface plasmon is confined to the metal surface in all directions and therefore it cannot propagate. Such surface plasmons are called as localised surface plasmons (LSPs). Therefore, LSPs are excitations of the conduction electrons of metallic nanostructures coupled to incoming light. when a sub-wavelength metallic nanoparticle is coupled to an external field with a certain frequency, the conduction electrons oscillate opposite to the restoring force of the nuclei, along the direction of the external filed, rendering the metal nanoparticle as an oscillating dipole source as seen in Figure 3.

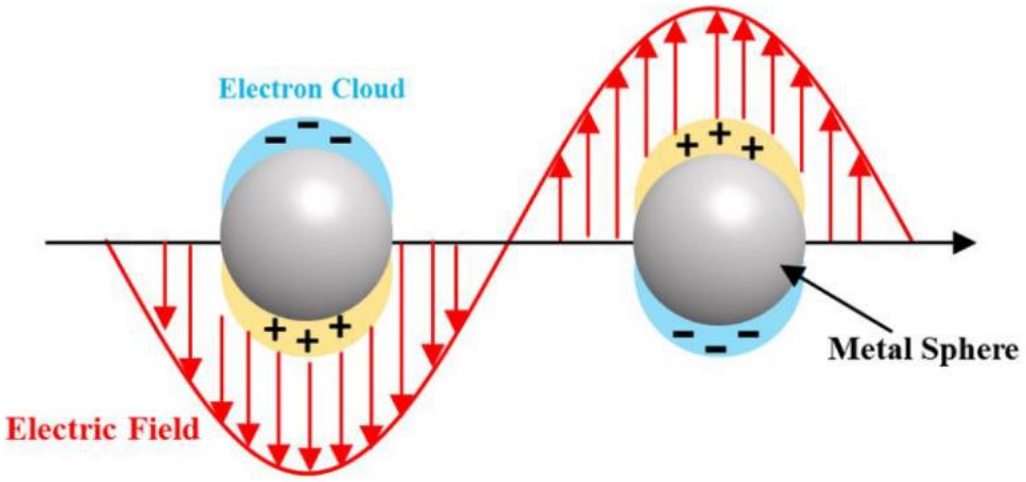


Figure 3 Representation of the LSPR principle [6].

When we put a metal directly in contact with a dielectric, the ions totally lay inside the metal, instead the electrons wave function extend through the interface for several atomic lengths into the dielectric. When interacting at the resonance with the optical electromagnetic field associated with the light, the conduction band electrons oscillate because there is an elastic recall from the nuclei, going across the interface as a collective effect. This electron oscillation goes into the metal according to the skin effect. This collective is the surface plasmon and it exhibits a particle/wave duality. When the object is a closed metallic surface wrapped with a dielectric, the collective oscillation is called localised surface plasmon. When the incident light has an angular frequency same of the plasmon oscillation frequency, the two waves go in resonance, this is called localised surface plasmon resonance (LSPR). In opposition to the surface plasmon polaritons, plasmon resonances can be directly excited by free space incident light. The effect of this resonance is that metallic nanoparticles exhibit the largest light extinction [15]. The particle edges are like a resonant cavity for the electrons, therefore making it bigger will enable higher modes of oscillation such as quadrupoles [16] and octupoles [17]. The LSPR is influenced by both internal factors, such as the shape and the material of the nanoparticle, and external factors like the refractive index of the medium surrounding the nanoparticle. Gold and Silver have an intense LSPR in the visible region, whereas Aluminium is the typical material of choice for ultraviolet plasmonics [18], because it has an higher plasma frequency than the above cited noble metals. Silver exhibits a very sharp response in the visible [19], however Silver's high chemical reactivity makes gold the most popular material for visible plasmonics [20]. Mie's theory is the main theoretical basis to describe optical scattering phenomena by nanoparticles [21]. The idea is to solve Maxwell's equations for the scattered field, but depending on the nanoparticle shape, analytical solutions do not necessarily exist.

Numerical calculation processes such as FDTD (see Chapter 2), T-matrix (Transfer-matrix) [22] or discrete dipole approximation DDA [14] are used to perform such difficult calculations.

## 1.4 QUASISTATIC APPROXIMATION

After having described the polariton propagating onto an infinite film, let us see what happens with a finite object. For sake of simplicity, let us consider a spherical surface. When the sphere radius is much smaller than the wavelength of the impinging light, we can assume the electric field to enter and leave the object at the same time. In this regime, the E field intensity can be considered constant across the whole sphere and the illumination intensity depends only on time. Another consequence is that all the electrons are vibrating in phase with the incident radiation. This important condition is called quasi-static approximation and greatly simplifies Maxwell's equations. The electromagnetic potential at any point is described by the Laplace equation [23]:

$$\nabla^2\varphi = 0 \tag{2}$$

With ϕ being the electrostatic potential. We can divide the electrostatic potential in two regions, one inside the sphere and one outside, Figure 4 shows these two areas. The gradient of the internal region will result in the electric field around the sphere (near field), the second will give the field far field. Solving Eq.2 in spherical coordinates, we obtain a split solution: one for the potential inside, and one for the area outside the nano sphere [36]:

$$\begin{cases} \varphi_{out} = -E_0 r\cos\vartheta + \dfrac{\varepsilon_m - \varepsilon_d}{\varepsilon_{m+2\varepsilon_d}} \dfrac{E_0 R^3 \cos\vartheta}{r^2} \\ \varphi_{in} = -E_0 r\cos\vartheta \dfrac{3\varepsilon_d}{\varepsilon_{m+2\varepsilon_d}} \end{cases} \tag{3}$$

Where, $E_0$ represents the incident electric field amplitude, r the distance from the sphere centre, R the radius of the sphere, $\varepsilon_m(\omega) = \varepsilon_r + i\varepsilon_i$ the dielectric function of the metallic sphere while $\varepsilon_d$ is the dielectric constant of the surrounding medium. As shown in Figure 4, two regions of electrostatic potentials are present, they are going to be used to derive both the electric field at the interface metal medium (near field) and the radiating one (far field).

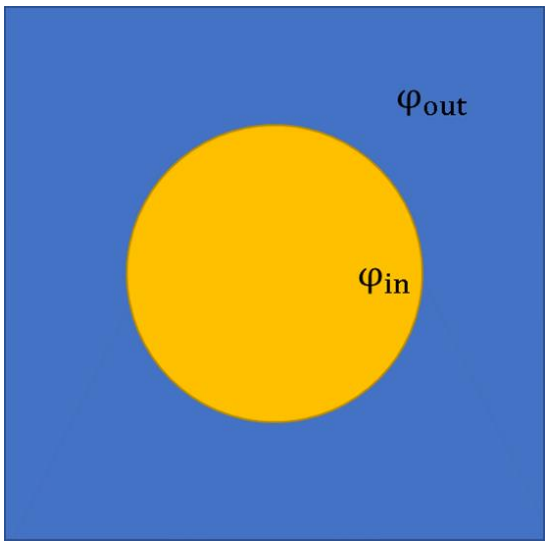


Figure 4 Schematic representation of the two potential regions coming out as solution of Eq. 2.

Starting from the potential, we can calculate the electric field, nf stands for near field:

$$E_{nf} = -\nabla\varphi_{in} = \frac{3\varepsilon_d}{\varepsilon_m + 2\varepsilon_d} E_0 \tag{4}$$

The polarizability of the metal sphere is [24]:

$$\alpha = 4\pi R^3 \frac{\varepsilon_m - \varepsilon_d}{\varepsilon_{m+2\varepsilon_d}} = R^3\xi \tag{5}$$

Where $\xi = \frac{\epsilon_m - \epsilon_d}{\epsilon_m + 2\epsilon_d} = \frac{\alpha}{R^3}$. The equation for $E_{nf}$ can be rewritten as:

$$E_{out} = |1 - \xi| E_0 \tag{6}$$

The near field induced on the metal nanosphere by the incident radiation is evanescent and spatially strongly localised and it has a very high intensity compared with the incident one. It is useful to define an electric field enhancement factor as the ratio of the two magnitudes. Consequently, the enhancement factor can be defined as:

$$F_{nf} = \frac{|E_{out}|^2}{|E_0|^2} = |1 - \xi|^2 \tag{7}$$

Once the "enhanced" polarizability has been defined Eq.(5), it is interesting to look at the scattering, absorption, and extinction cross-sections respectively, in function of the polarizability, for the nanoparticles:

$$C_{sca} = \frac{k^4}{6\pi}|\alpha|^2 = \frac{8\pi}{3}k^4a^6\left|\frac{\varepsilon_m - \varepsilon_d}{\varepsilon - 2}\right|$$

$$C_{abs} = kIm(\alpha) = 4\pi ka^3 Im\left|\frac{\varepsilon_m - \varepsilon_d}{\varepsilon_m - 2\varepsilon_d}\right| \quad (8)$$

$$C_{ext} = C_{abs} + C_{sca}$$

For small particles having $a << \lambda$ the light matter interaction process is dominated by absorption [25], in Figure 5 we can see the different cross sections plotted in function of the particle radius. From Eq(4), the generated near field is a function of the particle polarizability which itself depends on the particle size, the surrounding medium permittivity, and the dielectric function of the metal itself. From the expression of ξ, we notice that the near-field amplitude reaches a maximum when the condition $\epsilon_r \approx -2\epsilon_d$ is fulfilled, which is known as Fröhlich condition [26]. This condition is called resonant regime. The quasi-static approximation is convenient for deriving the field distribution, in this case, of a small nanosphere [27]. When the size of the particle increases, the quasi-static approximation is not applicable and effects of phase retardation appears, causing a dynamical depolarization of the electric field during the propagation. In Figure 5, the cross sections for different nano spheres sizes are calculated. For 30 nm radius or smaller spheres, the extinction is due exclusively to absorption, but with increasing the size, a scattered component appears. In the next we are going to see the Mie theory.

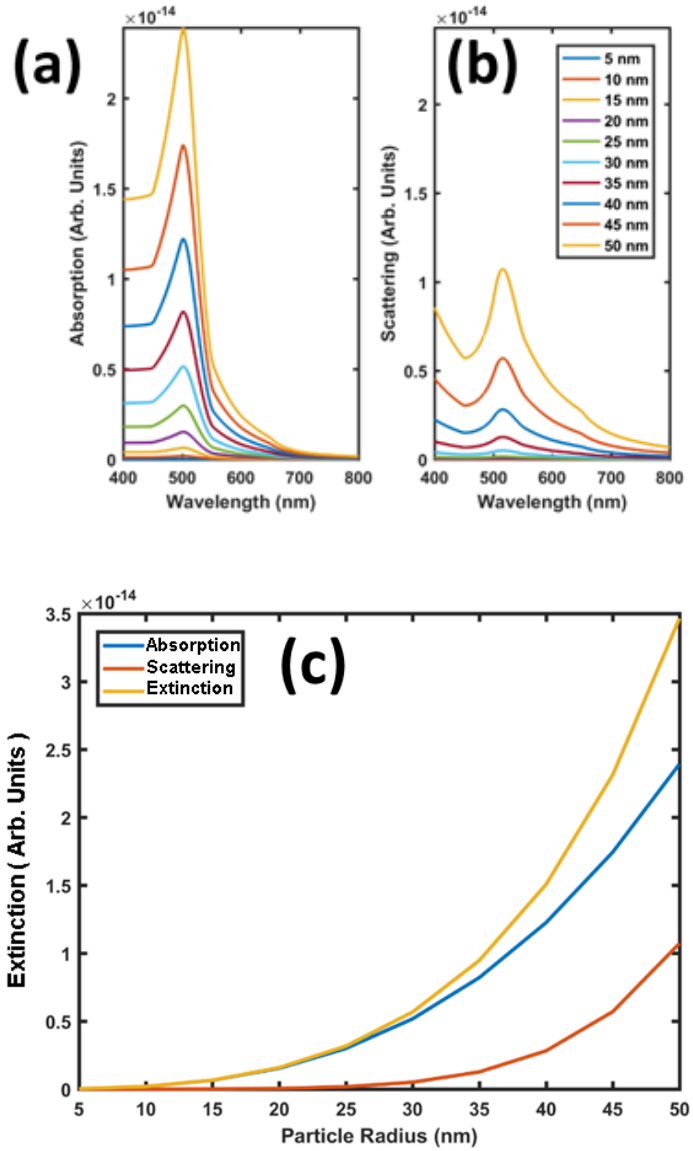


Figure 5 a) Absorption and Scattering cross section calculated in quasistatic approximation for gold spheres having a radius ranging from 5 to 50 nm. b) Cross sections peak intensity versus nanoparticle size. Label represent the radii. c) Maximum extinction value versus of the particle radius.

#### 1.4.1.1 VARIOUS MODES AND PARTICLE SHAPE

A nano particle can be treated like a resonant cavity. Increasing its size, the cavity can support different resonant modes. The simplest mode a nano sphere can support is a dipolar resonance. Increasing the size, we can have higher order modes such as quadrupole and hexapole. In the quadrupole the electric field shows four lobes around the nanoparticle, instead the hexapole six. So far, we have analysed nano particles having a spherical shape only. The spherical symmetry helps in finding an analytical solution to both extinction cross section and near field

pattern. For more complex shapes we need to recur to computational techniques such as FDTD which will be object of the next chapter. In the next paragraph we are going to discuss the light emission and how the emission can be controlled by using plasmonic nano structures.

## 1.5 FLUORESCENCE

The absorption process for a molecule can be described by

$$\gamma_{abs}=\sigma_{abs}\frac{S}{\hbar\omega} \tag{9}$$

Where $\sigma_{abs}$ stands for the absorption cross-section and S for the incident power density in free space, which is directly commensurate to the intensity of the electric field. Fluorescence is a process of relaxation, from a high energy state to the ground state, accompanied by emission of light which takes place in case of a class of molecules called fluorophores or in semi-conductor's nanoparticles called quantum dots. The emitted light is usually at a longer wavelength than the one that has been absorbed by the molecule and provided the energy needed for its excitation, this is known as Stoke shift. In Figure 6 we have the Jablonski energy diagram with all the processes involving absorption and emission from a molecule.

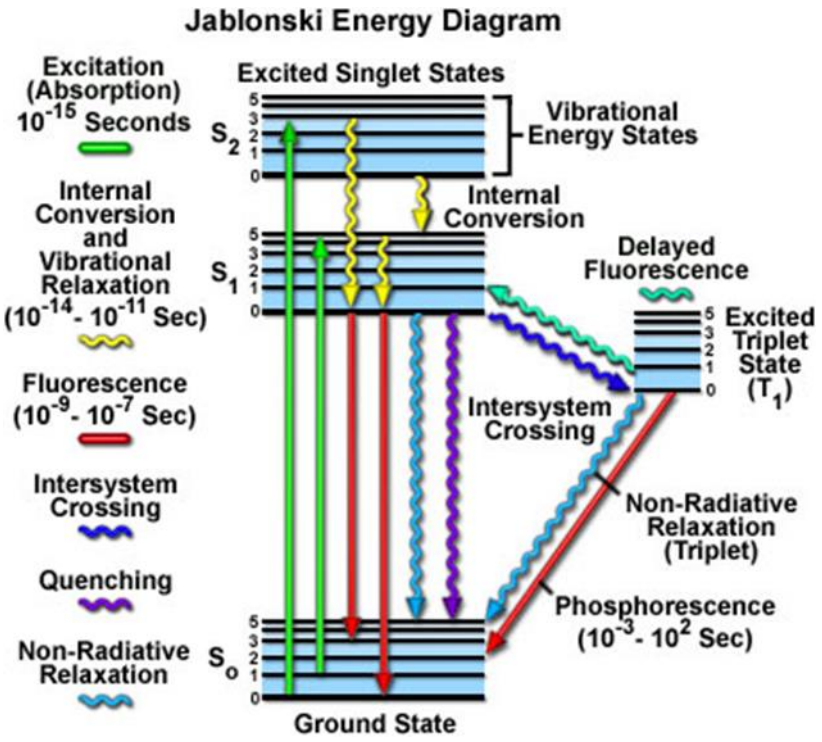


Figure 6 Jablonski diagram for the fluorescence related processes, the wavy lines represent non-radiative processes.

### 1.5.1 EMISSION IN FREE SPACE

After absorbing a photon, a fluorescent molecule in the exited state |e> can transit to the ground state |g>. The emission rate is given by the Fermi's golden rule [43]:

$$\gamma_{rad} = \frac{2\pi}{\hbar^2} |< g|E(r,\omega) \cdot p|e >|^2 \rho_g \tag{10}$$

Where p is the transition dipole moment and E(r,ω) the electric field of the exciting radiation and $\rho_g$ is the density of states, namely, the number of states per interval of energy at each energy level that are available to be occupied [1]. In vacuum the density of states is:

$$\rho_e(\omega) = \frac{\omega^2 V_0}{\pi^2 c^3} \tag{11}$$

This physical quantity represents the density of states is the density of photonic states available to the emitted photon (at frequency ω). From the Fermi golden rule, we can observe that the free-space emission rate depends on the intensity of the electric field and by the angle between the field and the transition dipole moment. In particular, the rate is zero when the electric field and the dipole moment are perpendicular to each other, while it is maximum when they are parallel. The energy accumulated in the excited state can be dissipated via two kinds of possible transitions: radiative and non-radiative decay. The radiative decay rate $\Upsilon_{rad}$ is defined by the Fermi Golden rule related to the probability of the transition of the event which is linked to Einstein's coefficient, is related to the reciprocal alignment between dipole moment and incident electric field as well as the density of states.

An important parameter that characterizes each fluorophore is the quantum yield, namely the ratio between the radiative decay rate and the total decay rate ($\Upsilon_{nr} + \Upsilon_{rad}$), with $\Upsilon_{nr}$ non-radiative decay rate. The $\gamma^0$ parameters are the quantities expressed above, but in vacuum.

$$q = \frac{\gamma_{rad}^0}{\gamma_{tot}^0} = \frac{\gamma_{rad}^0}{\gamma_{rad}^0 + \gamma_{nr}^0} \tag{12}$$

A parameter used to describe fluorescence is the average lifetime, defined as the average time that the molecule stays in the excited state before decaying. Lifetime is defined as the inverse of the total decay rate: $\tau = \frac{1}{\gamma_{tot}}$. The equation above are valid for the vacuum, but when considering fluorophores dispersed in matter, the quantum yield is accordingly modified (e.g. by the solvent medium where the molecules are dispersed). The typical lifetime, for fluorescence, can range from $10^{-9}$s to $10^{-12}$s. The emission intensity is given by the formula:

$$I(t) = I_0 e^{-\frac{t}{\tau}} \tag{13}$$

Where $I_0$ represents the maximum fluorescence, intensity reached during the excitation.

### 1.5.2 PHOTOBLEACHING

Photo-bleaching is an inhibition of the fluorescence that takes place under a strong resonance excitation. This phenomenon is provoked by cleaving of covalent bonds or non-specific reactions between the fluorophore and surrounding molecules [44]. In this case, the dye passes many times through an inter-system crossing procedure to transit from the triplet to the singlet and then to the ground state. It is known that the fluorescent molecules standing in the triplet state are more chemically reactive, especially with oxygen [46]-[47]. Oxygen ground state is triplet, and it is highly reactive with fluorophores standing in the triplet state, their interaction leads to the formation of free radicals (singlet oxygen). When the reaction takes place, the molecule disrupts its inner structure stopping the emission. The photobleaching can be divided into two different steps: excitation to the triplet state and destruction of molecules by chemical reaction. The probability for the photobleaching has the functional form [48]:

$$\phi_{bl=p_{ISC}p_D=\frac{\gamma_{ISC}\,\gamma_D}{\gamma_{tot}\gamma_{tot}}} \tag{14}$$

Where $p_{ISC}$ and $p_D$ are the probability of intersystem crossing and chemical destruction, respectively. $\Upsilon_{ISC}$ is the transition rate from singlet state to triplet, $\Upsilon_D$ destruction rate and $\Upsilon_T$ the triplet to ground state transition rate. The complete expression for the photobleaching probability [40]:

$$\gamma_{bl} = \phi_{bl}\gamma_{abs} = \phi_{bl}\sigma_{abs}\frac{|E^2|}{\hbar\omega c} \tag{15}$$

As expected from this last equation, we can notice that the bleaching depends on the incident power value. In the presence of field enhancement, due for example to a plasmonic resonance, the enhanced near field also contributes to the absorption cross-section and must therefore be considered when considering photobleaching.

## 1.6 SURFACE PLASMON DAMPING: FINITE SIZE EFFECT

Surface plasmons can mainly decay via three processes, namely: radiative decay, non-radiative decay, and dynamic depolarization, schematically represented in Figure 7.

### 1.6.1 RADIATIVE DECAY

Radiative decay is the main decay mechanism for large diameter nanoparticles [28]-[29] and results in a conversion of plasmon into photons leading to scattered light. This phenomenon creates an additional radiation field [14]:

$$E_{rad} = (\frac{k^2}{R} + i\frac{2}{3}k^3)\mu' \tag{16}$$

Where $k = \frac{\omega}{c}$ is the wavevector of the incident light and $\mu'$ the dipole moment induced on the nanoparticles by the illumination field:

$$\mu' = \alpha(E_0 + E_{rad}) = \alpha' E_0 \tag{17}$$

$\alpha'$is called the effective polarizability and is related to the electrostatic polarizability α by:

$$\frac{1}{\alpha'} = \frac{1}{\alpha} - \frac{k^2}{R} - i\frac{2}{3}k^3 \tag{18}$$

We can therefore rewrite the field enhancement factor as:

$$F'_{nf} = |1 - \xi'|^2 \tag{19}$$

Where $\xi'$ is the modified coefficient?

$$\xi' = \frac{\alpha'}{R^3} = \frac{\xi}{1 - k^2R^2\xi - i\,{}^2/_3\,k^3R^3\xi} \tag{20}$$

According to equation (20) above, an increase of the radius R corresponds to a reduction of the near field enhancement $F'_{nf}$ since $\xi'$ decreases (Since the polarizability for a metal is larger than one and R ~$10^{-8}$m).

### 1.6.2 NON-RADIATIVE DAMPING

The non-radiative damping of a surface plasmon results in the formation of an electron-hole pair via either intra-band excitation in the conduction band or inter-band excitation between other bands and the conduction band [30]. It is related to the light absorption of a metallic nanoparticle which results in phonon excitation and heat generation. This decay process is the main one in nanostructures where the surface-to-volume ratio is not negligible [31], such as small particles. When the diameter of the nanoparticle is smaller than the mean free path of the electron in the bulk (about 40 nm in gold [32]), the electron scattering contributes in a

considerable way to the energy loss. The total non-radiative damping rate is a function of both the inter-band damping rate and the rate for the electron scattering [33]:

$$\gamma = \gamma_{bulk} + \frac{A v_f}{R} \tag{21}$$

Where $\gamma_{bulk}$ is the non-radiative damping rate; $v_f$, the Fermi velocity; R, the particle radius and A is a factor proportional to the geometry of the system. The non-radiative damping changes the near-field enhancement via the dielectric function given by the Drude model [1]:

$$\varepsilon_m(\omega) = \varepsilon_\infty - \frac{\omega_p^2}{\omega^2 + i\omega\gamma} \tag{22}$$

Where $\varepsilon_\infty$ is the dielectric function in the limit of high frequency; ω, the angular frequency of the incident light and $\omega_p$, the plasma oscillation frequency of the free electrons, given by the expression:

$$\omega_p = \sqrt{ne^2/m_e\varepsilon_0} \tag{23}$$

where, n is the free electrons density; e, the electron charge; $m_e$, the effective mass of the electron.

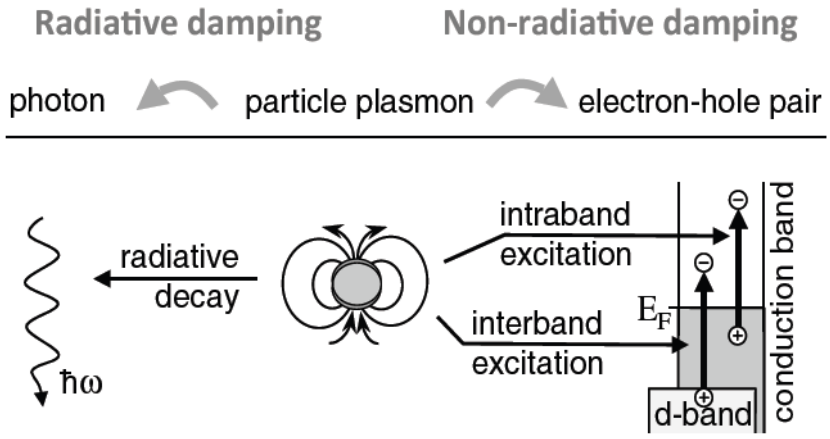


Figure 7 Scheme of the radiative and non-radiative damping of a surface plasmon in a metal nanoparticle from ref [34].

### 1.6.3 DYNAMIC DEPOLARIZATION

The near field always accumulates some phase retardation with respect to the incident field, but this is negligible when the particle is small. The depolarization field generated by the polarized matter is given by [35]:

$$E_{dep} = -\frac{4\pi}{3}(1 - k^2R^2 - i\,{}^2/_3\,k^3R^3)P \tag{24}$$

With P indicating the polarization inside the matter, assumed homogeneous over the whole spherical surface that can be expressed as:

$$P = \frac{3(\varepsilon_m - 1)}{4\pi(\varepsilon_m + 2) - (\varepsilon_m - 1)k^2R^2 - i\,{}^2/_3\,(\varepsilon_m - 1)k^3R^3}E_0 \tag{25}$$

If the nanoparticle is small compared to wavelength of the incident field (kR<<1), the component proportional to $k^3R^3$ can be neglected. Moreover, at the resonance frequency, the real part of P is zero leaving just:

$$P_{res} = \frac{3}{4\pi}\frac{\varepsilon_{res} - 1}{\varepsilon_i(1 - k^2R^2)}E_0 \tag{26}$$

Where $\varepsilon_{res}$ represents the value of $\varepsilon_m$ at the resonance, $\varepsilon_i$ imaginary part of $\varepsilon_m$

As the radius increases, the damping in the medium decreases. When the nanoparticle is larger, we cannot neglect the term in $k^3$ anymore. In this case the polarization under resonance condition is:

$$P_{res} = \frac{3}{4\pi}\frac{\varepsilon_m - 1}{i\varepsilon_i(1 - k^2R^2) - i\,{}^2/_3\,(\varepsilon_r - 1)k^3R^3}E_0 \tag{27}$$

For resonance we have the condition of vanishing denominator of Eq. (27)

$$\varepsilon_r(1 - k^2R^2) + 2 + k^2R^2 + {}^2/_3\,\varepsilon_i k^3R^3 = 0 \tag{28}$$

As soon as R increases, $\varepsilon_r$ must go more negatively, this results in a red shift and broadening of the plasmon resonance [27].

## 1.7 QUANTUM YIELD

Quantum yield of the fluorophore is defined as the number of emitted photons relative to the number of absorbed photons. Mathematically it is defined as:

$$\phi = \frac{\Gamma_{rad}}{\Gamma_{rad} + \Gamma_{nonrad}} \tag{29}$$

Where the Γ is the decay rate and it is the inverse of the lifetime. The quantum yield can be as high as 1. However, due to Stokes losses the fluorophore's quantum yield is always less than 1. The surrounding environments of the molecule can heavily modify both the radiative and the non-radiative decay rates. In the next paragraphs we are going to describe how the plasmonic nano particles can change the fluorescence properties.

## 1.8 MIE THEORY AND FLUORESCENCE IN PRESENCE OF NANOPARTICLES

Above a certain nanoparticle size, the quasi-static approximation is no longer valid and in this situation the Mie theory needs to be used to derive the equations for the scattering and absorption cross-sections. The Mie theory has been extended to study the interaction of a single dipole near a particle. The behaviour of an isolated emitting molecule near a nanoparticle is governed by the near field. Here, Mie theory is used to provide an analytical approach to these processes. A single emitter is placed a distance, $z_0$, from a spherical particle of radius a. The surrounding medium has a refractive index, $n_B$. In this model, the fluorescent dipole has power $P_0$, oscillating at a frequency $\omega_0 = {}^{2\pi c}/_{\lambda_0}$ in vacuum. The refractive index of the metal nanosphere, $n_s$, is assumed to be the same as the bulk metal materialThe decay rates of the molecule in the presence of a particle using the Mie formalism can be normalised with respect to the decay rate of the molecule in vacuum $\Gamma_0$. For a dipole perpendicular to the sphere.

$$\frac{\Gamma_{\perp}}{\Gamma_0} = n_B \left\{ 1 + \frac{3}{2} \mathrm{Re} \sum_{n=1}^{\infty} n(n+1)(2n+1) B_n \left[ \frac{h_n^{(1)}(u)}{u} \right]^2 \right\} \tag{30}$$

And parallel to the sphere.

$$\frac{\Gamma_{||}}{\Gamma_0} = n_B \left\{ 1 + \frac{3}{2} \mathrm{Re} \sum_{n=1}^{\infty} (n + \frac{1}{2}) \left[ B_n \left[ \frac{\zeta_n'(u)}{u} \right]^2 + A_n h_n^{(1)}(u)^2 \right] \right\} \tag{31}$$

Where $u = k_B z_0 = {}^{2\pi n_B}/_{\lambda_0}$ and $A_n$ and $B_n$ are the analytical expressions of the Mie coefficients described as:

$$A_n = \frac{j_n(k_B a)\psi_n'(k_S a) - j_n(k_S a)\psi_n'(k_B a)}{j_n(k_S a)\zeta_n'(k_B a) - h_n^{(1)}(k_B a)\psi_n'(k_S a)} \tag{32}$$

$$B_n = \frac{\varepsilon_B j_n(k_B a)\psi_n'(k_S a) - \varepsilon_S j_n(k_S a)\psi_n'(k_B a)}{\varepsilon_S j_n(k_S a)\zeta_n'(k_B a) - \varepsilon_B h_n^{(1)}(k_B a)\psi_n'(k_S a)} \quad (33)$$

Where $j_n$ and $h_n^{(1)}$ are the spherical Bessel and Hankel functions, and $\psi_n(z) = z j_n(z)$ and $\zeta_n(z) = z h_n^{(1)}(z)$ the Ricatti-Bessel functions. In equations (23)-(24) the n[th] mode relies on $A_n$ and $B_n$, the Mie scattering coefficients. These give an exact description of all particle modes responding to an external electromagnetic field [36]–[38]. Equations (25) and (26) are the total decay rate enhancements of the molecule when in the presence of a sphere. To analytically describe the coupling process of the emitter to the sphere, both the radiative and non-radiative decay rates are needed. The enhancement of the radiative rates with respect to vacuum can be written as [37]:

$$\frac{\Gamma_\perp^{rad}}{\Gamma_0} = \frac{3n_B}{2}\sum_{n=1}^{\infty} n(n+1)(2n+1)\left[\frac{j_n(u) + B_n h_n^{(1)}(u)}{u}\right]^2 \quad (34)$$

$$\frac{\Gamma_{||}^{rad}}{\Gamma_0} = \frac{3n_B}{4}\sum_{n=1}^{\infty}(2n+1)\left[\left| j_n(u) + A_n h_n^{(1)}(u)\right|^2 \left|\frac{\psi_n'(u) + B_n\zeta_n'(u)}{u}\right|^2\right] \quad (35)$$

The total decay rate is equal to the sum of the radiative and non-radiative decay rates. Therefore, the non-radiative decay rates for parallel and perpendicular dipole orientations are [38]:

$$\frac{\Gamma_\perp^{NR}}{\Gamma_0} = \frac{\Gamma_\perp}{\Gamma_0} - \frac{\Gamma_\perp^{rad}}{\Gamma_0} = \frac{3n_B}{2}\sum_{n=1}^{\infty} n(n+1)(2n+1)\left|\frac{h_n^{(1)}(u)}{u}\right|^2 [-Re(B_n) - |B_n|^2] \quad (36)$$

$$\frac{\Gamma_{||}^{NR}}{\Gamma_0} = \frac{\Gamma_{||}}{\Gamma_0} - \frac{\Gamma_{||}^{rad}}{\Gamma_0} = \frac{3n_B}{2}\sum_{n=1}^{\infty}\left(n+\frac{1}{2}\right)\left[\left|\frac{\zeta_n^{(1)}(u)}{u}\right|^2 [-Re(B_n) - |B_n|^2] + \left|h_n^{(1)}(u)\right|^2 [-Re(A_n) - |A_n|^2]\right] \quad (37)$$

These equations are simplified to take into consideration the particle size and distance between the emitter and the particle. A complete theory can be found in [38].

The presence of plasmonic nanoparticles can enhance or quench the fluorescence. The fluorescence intensity varies as a function of excitation rate, quantum efficiency, metal particle size, excitation wavelength and molecule and distance between particles. In any case, the essential point to consider in the treatment of this problem is that the emission rate is modified as [49]- [50]:

$$\gamma_{em=}\gamma_{ex}Qm \tag{38}$$

Where $\Upsilon_{ex}$ is the modified excitation rate and Qm the modified yield. For a single dye molecule that is moved from free space to the vicinity of a nanoparticle, the modified excitation rate can be written as [51]:

$$\frac{\gamma_{ex}}{\gamma_{ex}^{0}} = |\frac{E(r)\cdot\hat{p}}{E_0(r)\cdot\hat{p}}|^2 \tag{39}$$

where $\hat{p}$ is a unit vector in the direction of the transition dipole, $E_0$ is the amplitude of the incident electric field while E is the amplitude of the nano-particle local near field. As the local electric field depends on the position r, so does the enhancement. The relative orientation of the dipole with the near field changes the enhancement rate: as can be seen from the previous formula, when the orientations are parallel, the enhancement is maximum, whereas when they are perpendicular, the enhancement is minimum. Let us consider the quantum yield Q now: the energy transfer from the dye molecule to the nanoparticle contributes to the excitation of the surface plasmon. Because of this, the modified quantum yield can now be written as [51]:

$$Qm = \frac{\gamma_{rad}}{\gamma_{rad}+\gamma_{nr}} = \frac{{\gamma_{rad}}/{\gamma_{rad}^{0}}}{{\gamma_{rad}}/{\gamma_{rad}^{0}} + {\gamma_{ET}}/{\gamma_{rad}^{0}} + {(1-q)}/{q}} \tag{40}$$

With $\gamma_{nr=}\gamma_{nr}^{0}+\gamma_{nr}^{ET}$ modified non-radiative decay rate of the molecule, $\gamma_{nr}^{ET}$ energy transfer from the molecule to the nanoparticle while $\gamma_{rad}$is the modified radiative rate and q is the original quantum yield (molecule quantum yield in vacuum). The nanoparticle presence changes $\gamma_{rad}$ by coupling radiative LSP modes to the emission of the fluorophore.

The fluorescence lifetime changes in presence of a nanoparticle as:

$$\tau = \frac{1}{\gamma_{rad}+\gamma_{nr}^{0}+\gamma_{nr}^{ET}} \tag{41}$$

Since the expression of the lifetime of a molecule in the free space and in proximity to a nanoparticle are different, the measurement of the lifetime can provide information about the

relative distance between particle and molecule. The emission intensity I(t) will be characterized by the presence of two exponential functions having different characteristic times [52]:

$$I(t) = \alpha_F e^{-t/\tau_F} + \alpha_B e^{-t/\tau_B} \tag{42}$$

The $\alpha_j$, with j=B, F coefficients are weights that depend on the molecule's concentration [23].

When the dye molecule is in the vicinity of a nanoparticle, different decay processes can happen pure quenching, namely, when the molecule energy is transferred to the metal and subsequently it decays via electron- hole pair excitation inside the metal. Coupling to the photons of the excitation electric field or coupling to the LSP modes. Subsequently the modes coupled to the LSP can be reconverted in photons by additional process, scattering for instance. It is worth noting that the fluorescence is strongly modified by the presence of metal nanoparticles since the plasmonic near-field interacts with the fluorescent molecules enhancing the quantum yield. These modifications are due to the introduction of extra decay channels (both radiative and non-radiative) thank to the nano particle presence (chapter 1.6.2).

## 1.9 PURCELL FACTOR AND MODE VOLUME

As we have seen in equation (40), an emitter's quantum yield is modified by the presence of the nanoparticle. The two elements need to be treated like a coupled system. A plasmonic particle can be modelled like a resonant cavity. The emitter-cavity mode coupling is measured with the so-called $Q/V_{eff}$ ratio, where Q is the mode quality factor and $V_{eff}$ is the mode volume.

The quality factor Q is related to the energy balance, and it is defined as the energy stored over the energy lost. This is the mode lifetime in the cavity, namely the temporal representation of the mode itself. The volume mode $V_{eff}$ instead is defined as the energy stored over the maximum energy. This represents the electromagnetic confinement, namely it is the spatial representation of the mode.

Weakly coupled systems are described by the Purcell factor and the energy dissipation into the mode is irreversible. The Purcell factor is defined as:

$$\frac{\gamma}{n_b \gamma_0} = \frac{3}{4\pi^2} \left(\frac{\lambda}{n_b}\right)^3 \frac{Q}{V_{eff}} \tag{43}$$

where γ is the emitter spontaneous decay rate into the cavity compared to its free-space value $\gamma_0$, $n_b$ is the optical index inside the cavity, and λ is the emission wavelength. This description is

just a more specific case of the more general Fermi's Golden rule. In case of strong coupling, we need to add a Rabi oscillation, revealing cycles of energy exchanging between the emitter and the cavity [53]. The quality factor Q can therefore be expressed as:

$$Q = \frac{\omega_1}{\Gamma_1} \tag{44}$$

The expression for the mode volume for a dipolar resonance is determined from the Purcell factor and more specifically via the ratio $\frac{\gamma}{\gamma_0}$ (assuming the surrounding refractive index is equal to 1) and the dipole perfectly perpendicular to the particle surface, we obtain, from [54]:

$$V_1^{\perp} = \frac{\pi z_0^6}{R^3} \tag{45}$$

Where $z_0$ is the distance to the particle centre and R the radius of the particle.
The Purcell factor is also a measurement of how efficient the radiative process from the cavity is, the strategies used to increase it, are either increase the Quality factor Q or decrease the mode volume V.

## 1.10 PURELY METALLIC NANOCAVITY

There are commonly two strategies used to increase the quantum yield of a dipole-particle system, one increasing the quality factor, two reducing the mode volume. One of the simplest ways to reduce the mode volume is to use highly coupled systems, such as nanoparticles on a mirror (NPOM) and to place the emitter in the near field hot spot. Placing nanospheres onto a metallic substrate is a relatively easy task in terms of sample preparation, which is why the NPOM are a very popular solution [55]-[56]. Our group in the recent past [57] managed to achieve a mode volume as small as:

$$V = 0.02\left(\frac{\lambda}{2n}\right)^3 \tag{46}$$

This value is almost 50 times smaller than the diffraction limit. Typical values to sub diffraction limit breaks are in the order of 2-3 times.

On the counterpart, the quality factor can be orders of magnitude higher if using dielectrics. We tried to improve this system by replacing the metallic mirror with a dielectric one to reduce the losses typical of the metals without losing the small mode volume. The mirrors chosen for this purpose are the Distributed Bragg Reflector.

## 1.11 DISTRIBUTED BRAGG REFLECTOR

A Distribute Bragg Reflector is 1D photonic crystal for which the stopband forms a dielectric mirror formed from multiple layers of two alternating materials with different refractive index. Each interface causes a partial reflection. When the optical thickness of the dielectric pair is around a quarter of the wavelength of the impinging light, all the reflections combine with constructive interference. The DBR reflectivity can be expressed with the expression [58]:

$$R = \left[\frac{n_0(n_2)^{2N} - n_s(n_1)^{2N}}{n_0(n_2)^{2N} + n_s(n_1)^{2N}}\right]^2 \tag{47}$$

The range of wavelengths that are highly reflected from the structure is called photonic stopband and can be described by [59]:

$$\frac{\Delta f_0}{f_0} = \frac{4}{\pi} arcsin\left(\frac{n_2 - n_1}{n_2 + n_1}\right) \tag{48}$$

Where $n_1$, $n_2$ are the refractive indices of the different layers, $n_0$ the surrounding medium index, $n_s$ the substrate index, N the number of pairs and $f_0$ the central frequency of the reflection band. In Figure 8 we have the calculated reflectivity of two DBRs used in the experimental studies. In Figure 8 some typical DBR reflection spectra calculated by setting the central wavelength at 600 nm and consisting of 13 pairs of alternating layers of silicon dioxide (n = 1.45 [60]) and Titanium dioxide (n = 2.5 [61]). The second spectrum instead, it has 500nm as central wavelength is made by Niobium pentoxide (n = 2.3 [62]) and silicon dioxide (n = 1.45 [60]).

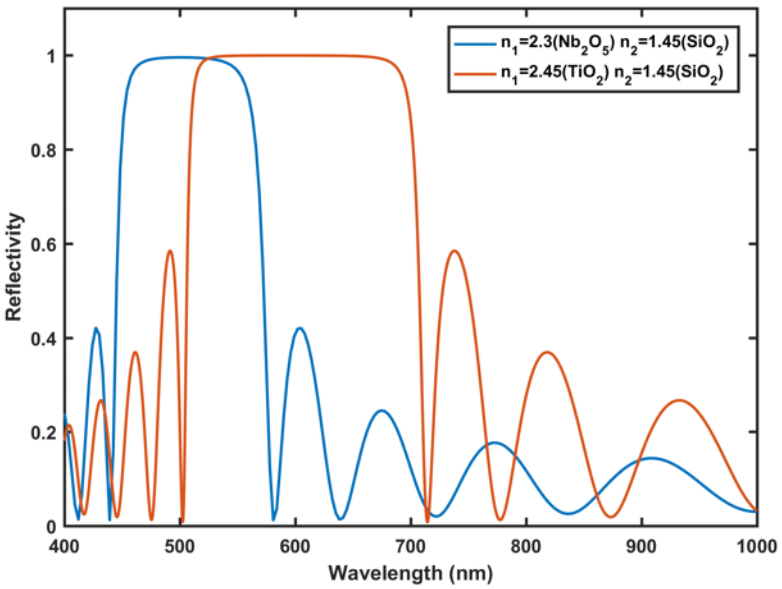

Figure 8 Calculated Reflectivity for a 600nm (orange) and 500 nm (blue) centred DBR with angle of incidence perpendicular to the surface.

The DBR reflectivity is highly dependent on the polarization of the impinging light [63], [64], indeed TE modes, or S polarised modes, are well reflected by the Bragg mirror, whereas TM, or P polarised modes, tend to penetrate inside the structure. A new class of polariton phenomena can take place at the interface between a DBR and a metal film since we are coupling a one-dimension photonic crystal (DBR) mode with a plasmonic resonance, these are known as Tamm Plasmons.

## 1.12 TAMM PLASMONS

A Tamm plasmon is a type of plasmon that exist at the interface between a metallic layer and a Bragg stack. It can be excited both by TE and TM polarizations and its dispersion lays into the light cone [65]. A Tamm plasmon usually appears blue-shifted with compared to the first Bragg mode of the DBR Figure 9 (d).

It is a common misconception to believe that the mode confinement in a DBR takes place because of the multiple reflections taking places at the various interfaces of the stack. The confinement, instead, takes place because of the impossibility for a specific mode to travel through the stack due to destructive interference.

The confinement inside the DBR multilayer is therefore due to a photonic stop band of the Bragg mirror and not to total internal reflection [66].

Tamm states can be coupled with different emitters and have been used to control the emission properties [67]. Confined Tamm plasmons are used to get lasting effect both in metal/semiconductor [68] and organic molecules [69]. Tamm plasmons are still optical phaenomenon that involve the loss of a metal, namely the quality factor is still orders of magnitude lower than dielectric resonators. Recently a milestone paper [70] has proved that an intermediate resonance between the conventional Tamm mode and the first Bragg mode can exist. This new mode is name Super Tamm with a quality factor up to 5000. This mode is less shifted from the Bragg mode and spatially it is localised much further into the DBR compared to the Tamm mode Figure 9 (a-b).

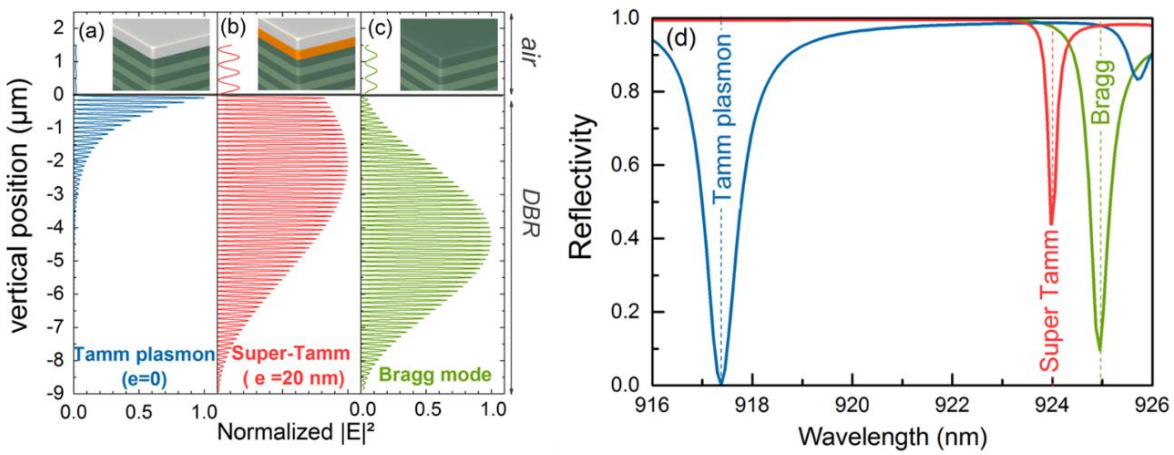


Figure 9 Spatial repartition of the normalized d electric field intensity calculated for the (a) Tamm plasmon mode (λ = 917.4 nm); (b) super Tamm mode (λ = 924 nm); (c) first Bragg mode (λ = 925 nm). (d) Calculated reflectivity for the same systems. From [70]

## 1.13 CONCLUSION

In this chapter, we discussed the basic theory behind surface plasmons the radiative damping, non-radiative damping, and depolarization. We have seen that, as the particle size increases, the radiative decay plays a more important role on the energy loss while non-radiative becomes less important. The phase retardation, it helps in increasing the enhancement for small sized nanoparticles while in decreasing it in the case of larger sizes. In the next chapter we are going to see how these properties characterize the interaction between a nano particle and an emitter modelled as a dipole. In this chapter we have seen the basics of the light matter interaction at the nanoscale, we focused on the emission modifications induced in presence of a plasmonic entity, and particular care has been given to the fluorescence. Both enhancement of the emission process and inhibition, such as quenching and photobleaching, have been described. Based on the plasmon enhancement, the fluorescence of a dipolar molecule is modified by a metallic nanoparticle nearby. The emission intensity is influenced by the modifications to excitation rate and quantum yield of the emitter. Those factors depend on local electric field, molecular orientation and separation distance between molecule and nanoparticle.

# Chapter 2 SIMULATIONS AND CALCULATIONS TECHNIQUES

In this chapter the modelling techniques are presented. In the specific both the theory and some basic application of Finite Domain Time Domain FDTD are presented. Extensive use of this technique has been done in the experimental chapters.

## 2.1 FINITE DOMAIN TIME DOMAIN CALCULATION

The Finite Domain Time Domain (FDTD) method was introduced by Yee [71], nowadays it is widely used into computational electromagnetism. This numerical technique provides a good and simple way to simulate the electromagnetic behaviour of a system in situations where an analytical solution is too difficult to determine. This algorithm discretises the time and the space and then calculates the time evolution of the Maxwell's equations. [72].

The technique still works on anisotropic media. The FDTD method has been used to model a wide range of plasmonic structures [73]-[74] and a variety of software is available to perform FDTD calculation. In this work, we use the commercial software called FDTD Solutions provided by Lumerical [75].

### 2.1.1 PROCESS ALGORITHM

Like everything else in electromagnetism, Maxwell equations are used to describe every phenomenon. FDTD works in the time domain, so we are interested into the two equations containing the time:

$$\frac{\partial \boldsymbol{H}}{\partial t} = -\frac{1}{\mu}\nabla \times \boldsymbol{E} - \frac{1}{\mu}(\boldsymbol{M}_{source} + \sigma^{*}\boldsymbol{H})$$
$$\frac{\partial \boldsymbol{E}}{\partial t} = \frac{1}{\varepsilon}\nabla \times \boldsymbol{H} - \frac{1}{\varepsilon}(\boldsymbol{J}_{source} + \sigma\boldsymbol{E}) \quad (49)$$

With the extra factor proportional to σ* due to magnetic losses into the medium. This term is included as M and J can act as independent sources into time domain calculation and might have associated losses. The two equations above represent six coupled differential equations, which are the starting point for the Yee algorithm [71]. This algorithm begins dividing the space into a uniformly spaced rectangular grid in all the three dimensions Figure 10.

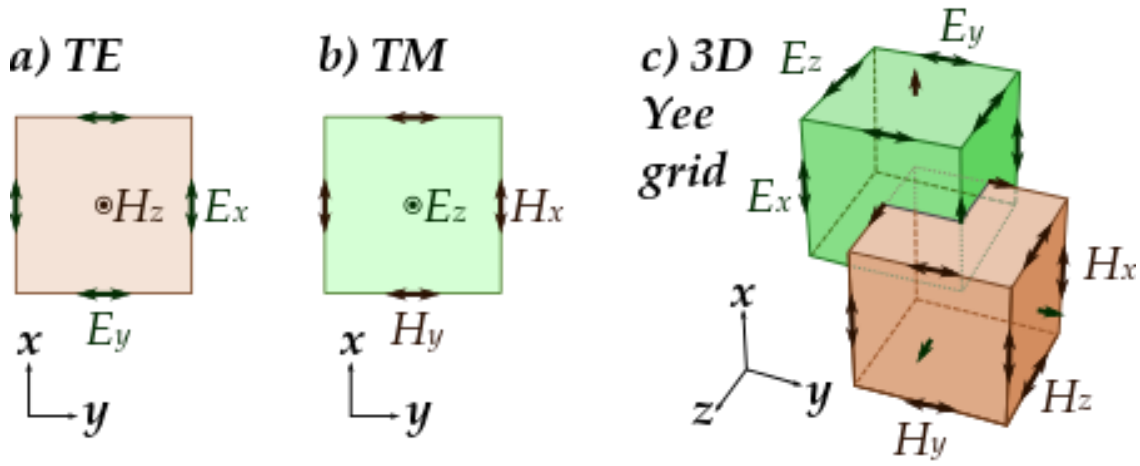


Figure 10 Electric and Magnetic field distribution over the Yee cell. From ref [76]

The magnetic field is sampled parallel to the edges of the cell, instead the electric one it is recorded at the centre of the cell perpendicular to the surface. Figure 10c shows such a grid, magnetic field projections circulating about the normal electric field vectors in such a way that a curl operation can be calculated using Maxwell's curl equations. A similar discrete projection can be generated for the vectorial electric field about the normal magnetic field vectors. The six coupled differential equations from the curl are discretized using the grid, the partial derivatives are approximated and solved with numerical schemes.

All the detailed equations behind the 3-d calculations can be found in literature [77],[78],[79]. The solutions to these equations express the future unknown fields in terms of the known past fields and are described as update equations. This process is repeated for all the cells of the grid until the whole simulation time has passed. The steps for the computations are the definition of the computational domain, mesh, material definition, definition of the light source, data collection. The space into the simulation domain is divided into equally spaced cells, then the material must be specified for each cell of the domain. Any material can be used if its permittivity, permeability, and electrical conductivity are specified. Once the geometry of the problem is defined, the light source must be defined. Different kinds of sources can be used such as plane wave, dipole, or Gaussian beam. In FDTD all the light sources are pulsed as we want to see how the electric and magnetic fields evolve in time. This technique allows to calculate the electromagnetic fields for all the frequencies in one shot, but it does not allow any parallelization as the solution at a given time depends on the fields at a previous time.

### 2.1.2 PRECISION

The discretisation of both space and time is one of the largest sources of error. The discrete step must be arranged in such a way that the fields must limit on how far the electromagnetic

energy can propagate within one timestep. Assuming the electromagnetic energy can travel maximum at the speed of light, c, the longest propagation possible in vacuum is $c \cdot \Delta t$. The Courant Factor S is the coefficient connecting space and temporal step:

$$\Delta t = \frac{S\Delta x}{c} \tag{50}$$

Where Δx is the spacial step and c the speed of light in vacuum.

The simulation stability is deeply influenced by S.

In a unit cell, in one-time step, the field can travel maximum the longest distance possible. Assuming Δx to be the side of the cubic cell, the farthest distance is $\sqrt{3}\Delta x$.

The spatial resolution is crucial in the simulation. The only parameter that can distinguish an object from the other one is the permittivity. Each cell of the grid needs to have a permittivity associated with it. Shapes that can be divided into cubes are easy to map, however sphere or other non-square geometries cannot be divided into cubes, therefore a unique permittivity cannot be associated with the cell. This creates a discontinuity at their boundaries, which is called staircase effect. Lumerical has some tools to correct it, called mesh refinement [80].

The idea is to confine these inaccuracies via a smoothing carried out by averaging the dielectric function for that given grid point with its neighbours. This sub-pixel smoothing partially removes the staircase in the dielectric function assignment [81]-[82]-[83]-[76].

The Yee lattice introduces other forms of error since the electric and magnetic fields are shifted by half a cell in space and half a time step apart. This effect is mitigated by choosing the appropriate mesh size. Indeed, a mesh step smaller than the light wavelength will make the shift between the fields negligible. So, the simulation must be designed in a way that the Courant obeys the following relation: $S \leq 1/3$ this is known as stability condition.

### 2.1.3 MATERIALS

The materials in each cells of the computational grid are specified via their relative permittivity ε(r), magnetic permeability μ(r) and conductivity σ. This works immediately for isotropic, linear, and non-dispersive materials. The anisotropies come from materials, such as liquid crystals, where the permittivity function is different for different directions. This is solved in FDTD by applying the material in a tensorial form.

The non-linearities are introduced by materials which electro-magnetic behaviour change with the intensity of the electric or magnetic field. Material dispersions are really evident when using metals. It happens when the permittivity changes with the frequency of the electric field. The

implementation of a dispersive material is performed by fitting the experimental data to a mathematical model. The modelling is needed since the experimental data are a function of the frequency and FDTD calculations are performed in the time domain. The most common models are Drude, Lorentz, Debye or so-called critical points terms. Noble metals, such as gold, is usually approximated with a combination of Drude-Lorentz since of the interband transitions.

### 2.1.4 BOUNDARY CONDITIONS AND SYMMETRY

The simulation cannot be infinitely wide since the computational memory is finite. The edges of the calculation domain can be complicate for the FDTD. Boundary conditions are needed to spatially confine the calculation without artefacts. Different solutions exist depending on the system to be modelled: for instance, periodic boundary conditions, Bloch periodic boundary conditions, perfect matching layers (PML) and metallic walls. The metallic wall consists in imposing the field inside the material to zero because of the phenomenon of the skin effect. Perfect matching layers were developed in and consist of multiple layers of material that allow the wave to penetrate through the layer while being absorbed with lower reflections [84].
The periodic boundary conditions require the condition:

$$E(x + l) = E(x) \tag{51}$$

Where x represents the vector position and l the lattice periodicity. Namely the field at the edge of the domain must be the same at the other side. This technique is widely used to simulate regular arrays where the calculation window corresponds to one-unit cell that can then effectively be repeated infinitely by the periodic boundary condition. By calculating the fields into the basic cell is possible to get immediately the field distribution in the whole array. If a phase shift between each period is involved, $E(x + l) = e^{ikx}E(x)$, for a Bloch periodic condition must be used for each wavevector k. Photonic crystals and waveguides are excellent applications for Bloch conditions [85]. Periodic conditions work only because there is a symmetry into the structure. When simulating an object with mirror symmetry, we can calculate just half of the domain and extend the results to the other half. If the system has another axis of symmetry, the calculation domain becomes a quarter. For high symmetry objects like spheres, using symmetry, the simulation domain can be reduced to 1/8” of the original geometry.

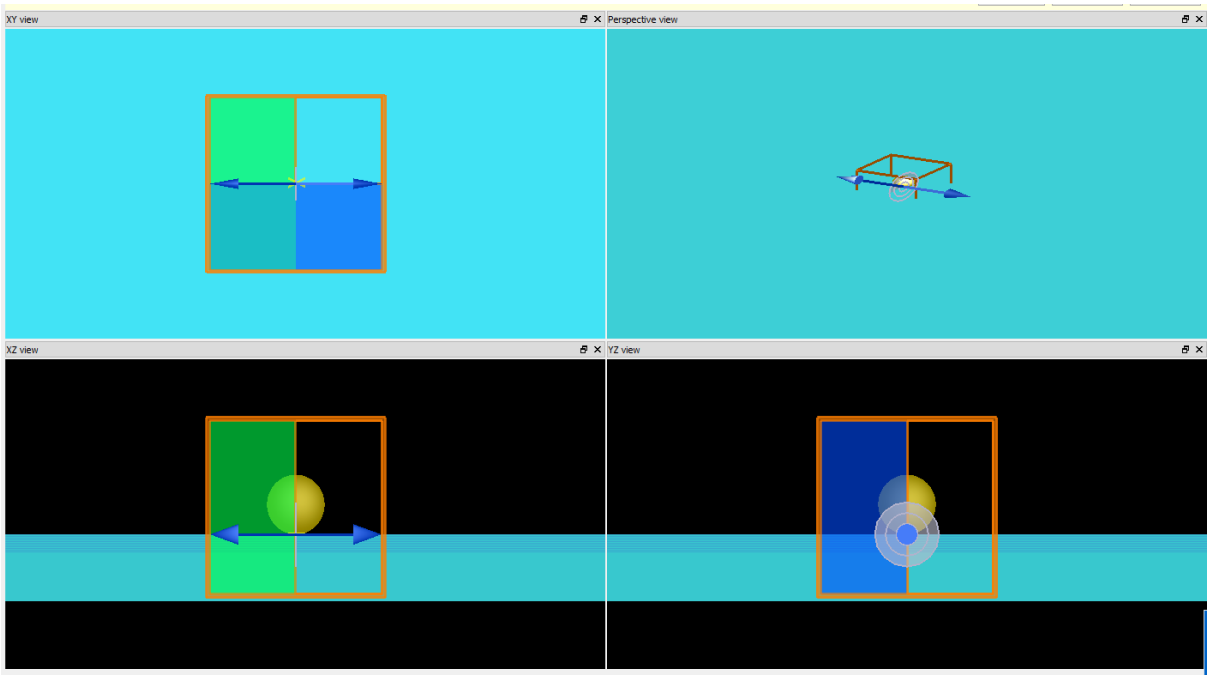


Figure 11 Example of a 4-fold symmetric system. Only the little quadrant in the north east corner is computed. This is system will be discussed thoroughly Chapter 4.

In Figure 11, we can see how a sphere on top of a dielectric mirror has two axes of symmetry parallel to z. Using symmetries, only the sector in the north east corner of the domain needs to be computed. The original simulation, namely without using the symmetries, required about 48 Gb of RAM, whereas, using symmetries, only 12 Gb are required.

To correctly use the symmetries, we must account for the symmetry of the source as well. In blue we have the portion of the domain where the field is symmetric, in green where it is anti-symmetric. The symmetry or antisymmetric of the field depends how the axis is oriented with the polarization axis of the source.

### 2.1.5 SOURCES

Different kind of sources are used for finite domain simulations. In the progress of this thesis, we have used plane wave, dipoles, and total field scattered field (TFSF). Plane waves are useful to measure the reflectivity from a structure or a film. Dipole sources enable to simulate a quantum emitter and therefore have many applications. In the work presented here we used them to calculate the near to far field projections and radiative enhancement. See Chapter 4 for real applications. The TFSF source is a plane wave-based source that is used to calculate scattered and absorbed fields from a structure with arbitrary shape. Using the additivity of the Maxwell equations we can split the total electromagnetic field into scattered and incident fields. By recording the field around the structure (total) and the field around the source surrounding the source (scattered), it is possible to obtain the absorbed field by simply subtracting the

scattered from the total. In Figure 12 An example of a gold sphere scattering setup, in grey the source, instead the field monitors in yellow.

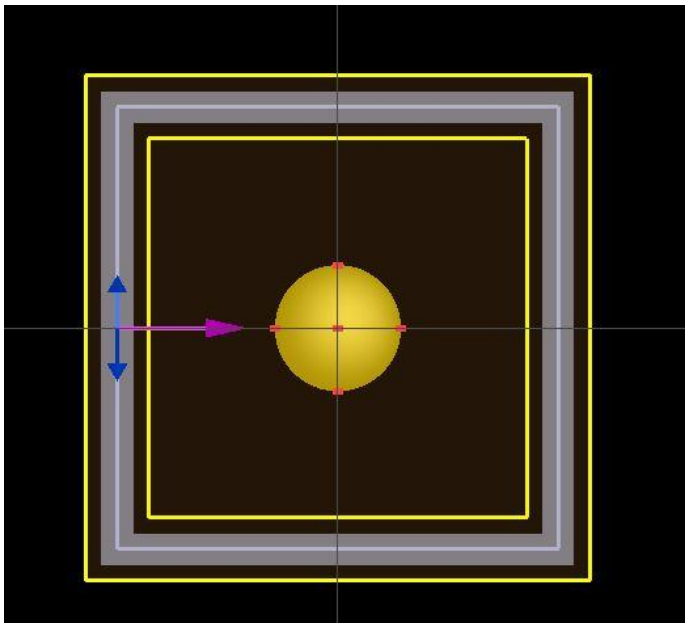

Figure 12 XY plane from a 3d scattering calculation. The blue arrow shows the polarization, the purple the direction of propagation.

### 2.1.6 LUMERICAL FDTD

We have seen in the boundary condition paragraph that symmetries help in reducing the computational time to get the results. Lumerical has an in-built function that helps to truncate the calculation once the results have converged enough to the real results. The duration of the simulation is the time length on which we would like to study the phenomenon. We will reach this time in steps of Δt. Once a time cycle has been completed, the software checks which percentage of the total energy is still present in the simulation domain. We can set a triggering threshold before launching the calculation, the simulation will stop once the total energy is less than the threshold set. This parameter is called "autoshutoff" and it is defined as the fraction of the maximum energy injected into the system. To obtain steady state results, we need to carry out the simulation until all the energy has dissipated. Typical values for the minimum autoshutoff range from $10^{-5}$ to $10^{-9}$ depending upon the application. In Figure 13 we can see how a simulation got shut at 45% of the total time with an autoshutoff of $10^{-8}$. A decreasing autoshutoff is index of convergence as well since the injected energy has been converted. Instead, a fluctuating one is evidence of instability, due to a PML reflection for instance.

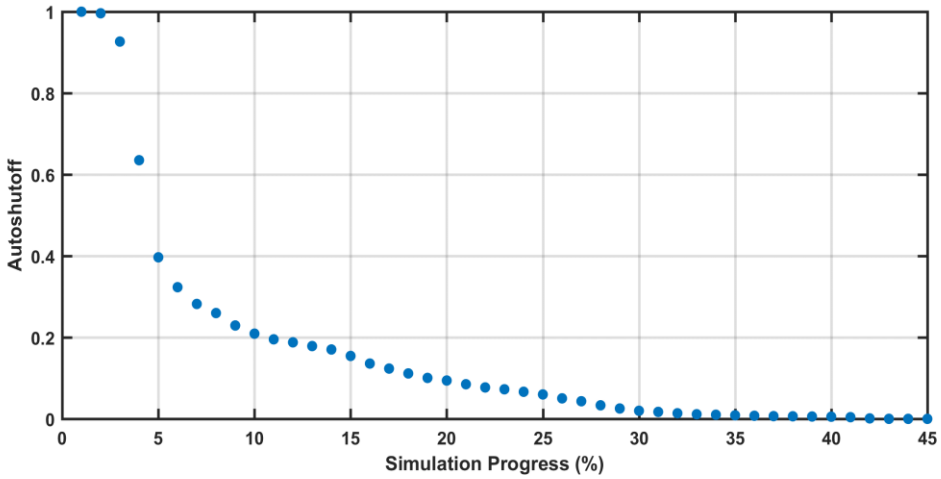


Figure 13 Autoshutoff progress in a very slow decay simulation.

### 2.1.7 NEAR TO FAR FIELD PROJECTION

The simulation domain cannot extend too long, otherwise the required memory will quickly outnumber the available one. To calculate the electric field far away from the structure, a distance equal to several wavelengths, we need to use a dedicated tool, the near to far field projections.

Near to far field projection increases the versatility of the FDTD by recording the electric field onto a surface the near field and project the equivalent electric and magnetic current to any point in space. An algorithm for this process was firstly introduce by [86]. Lumerical FDTD has a tool to calculate the near to far field projection at given wavelength. The theoretical basis for this calculation process come from [14] and from the book [129] and essentially projects the near field recorded by a monitor onto a hemispherical surface 1 meter away. Subsequently I created a script (in APPENDIX A) to batch automatize the far field extraction for each wavelength and generate the wavelength vs angle raw maps like in Figure 14.

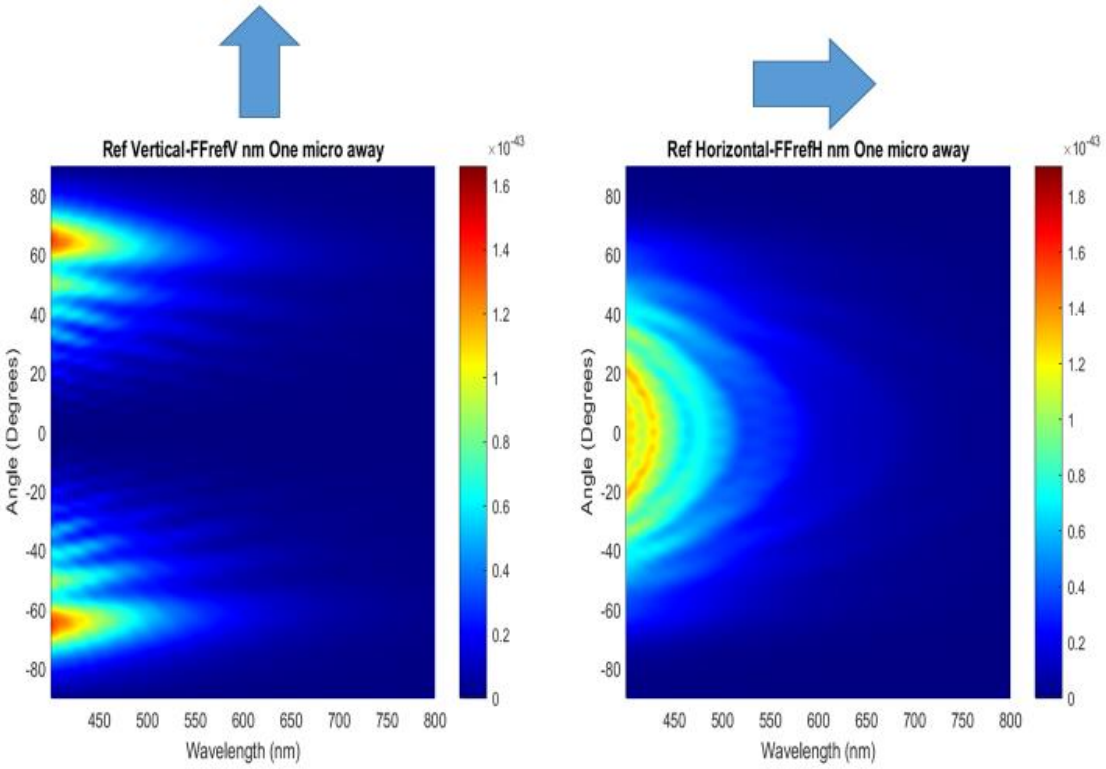


Figure 14 Left: Angle vs wavelength far field raw map for a vertical dipole in vacuum; Right: far field raw map for a horizontal dipole. Both showing the far field projections of an isolated dipole in vacuum.

These raw maps have not got any sort of processing, even the standard Lumerical CW normalization [130] is disabled. Our main purpose for using the near to far field projection is to understand the directivity of the radiation. To do so, we had to develop our own procedure to post process the raw data. The results of these calculations are shown in chapter 5. Only the test and validation method for an isolated horizontal dipole is illustrated here. We know that the radiated dipole power in vacuum is:

$$P = \frac{p_0^2 \omega^4}{12\pi\varepsilon_0 c^3} \tag{52}$$

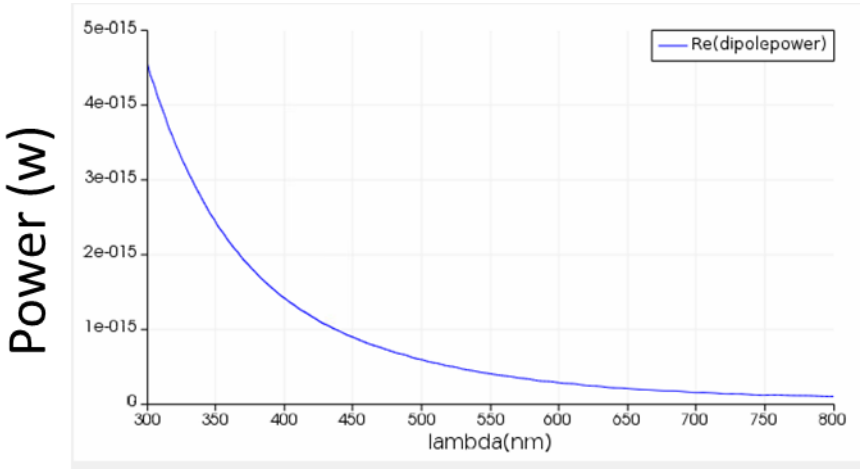


Figure 15 Plot of Equation (52) as seen in Lumerical. This curve represents the theoretical power radiated by the dipole in vacuum. Since the automatic normalization is disabled, we need to remove the $1/\lambda^2$ source dependence like in Figure 15 to see how the real radiation pattern. The steps are the following an example step by step is shown in Figure 16:

1. perform a Reference simulation with only a dipole in vacuum with the same orientation,
2. integrate such a reference across all the angles
3. divide each line of the map with this reference curve to get the directivity.

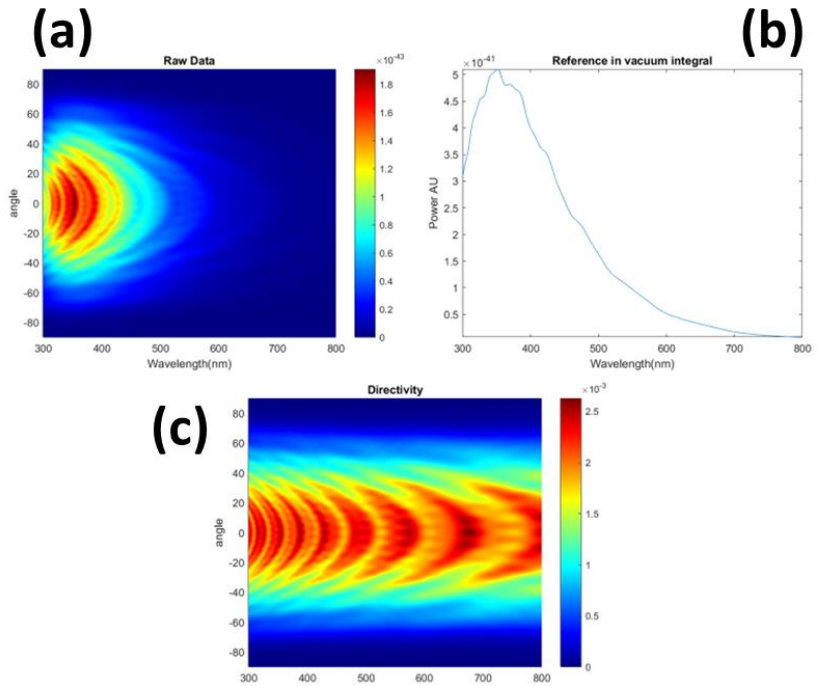


Figure 16 Near to far field projection normalisation essential steps. (a) raw data of the dipole emission in vacuum, (b) reference dipole emission spectrum in vacuum, (c) directivity normalised data

# Chapter 3 EXPERIMENTAL SETUP

A large portion of this PhD work involved developing and validating the necessary optical characterisation set-up for the study of nanophotonic samples. In this chapter we are going to present the instrumentation we developed to probe the interaction light-matter. The various techniques developed with the setup cover a wide spectral range (visible and near infrared) and include spectrally resolved intensity mapping, spectrally resolved k-space imaging, and spectrally resolved fluorescence lifetime imaging. We describe the experimental set-up developed throughout this PhD, including the development of a LabView based software to integrate all the components in a single graphical user interface. Basic calibration measurements were carried out to check the correct working of our custom-made instrument before doing any novel experiment. Once validated, this instrument was used to perform measurements on samples for other projects and collaborators across the university: those results are going to be described in chapter 4.

## 3.1 CONFOCAL MICROSCOPE STRUCTURE

The core of our setup is a home-built confocal microscope designed to work from the blue 400nm to the NIR 2200nm. The microscope allows to select the area to investigate with a resolution imposed by the objective diffraction limit. The set-up has been designed and built to work both in the visible and near infrared part of the spectrum. We can divide the whole optical setup in three parts: excitation optics, microscope, and signal collection path and detection as shown in Figure 17.

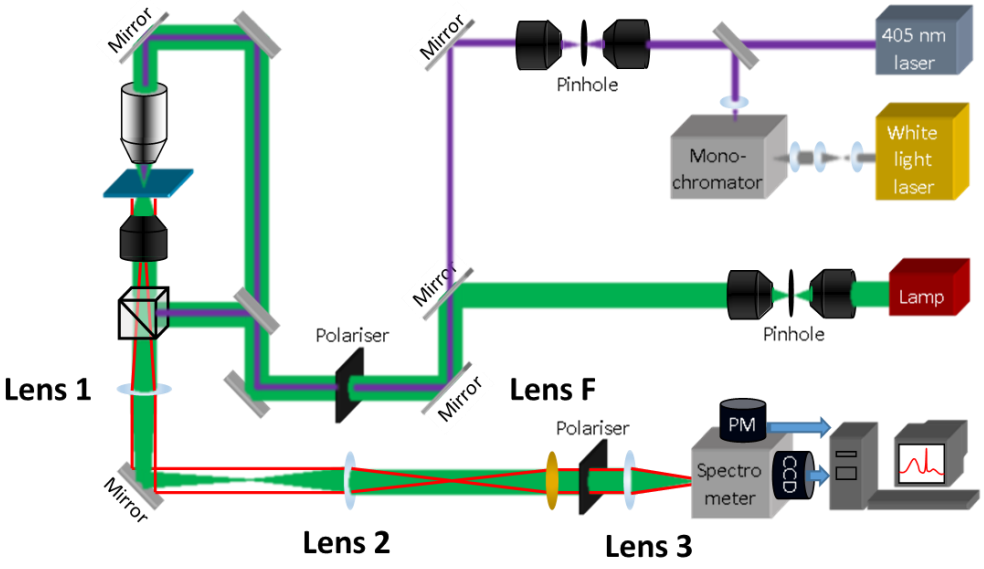

Figure 17 Schematic representation of the whole setup installed, all the optics designed in blue are fixed, instead the ones drawn in red are mobile.

## 3.2 EXCITATION PATH AND LIGHT SOURCES

We can observe the sample with white light and probe the interactions with three different laser sources. In Figure 18, we see all the hardware involved into the sample excitation positioned on the table. We have three lasers and one halogen lamps as light source on the table. The halogen is used when we need to visualise the sample as well as to measure transmission/reflection spectra. The white laser is another broad band source available on the table and it can be used both as an alternative white light source and as a tuneable laser source. The 405nm diode laser is a wavelength that falls out of the white laser range and it can be used both as continuous and pulsed light source. The last laser on the table is a 532nm pulsed laser, this laser has a repetition rate from few kHz to Hz range and it is very useful in experiments involving pumping ang gaining.

### 3.2.1 HALOGEN LAMP

A halogen lamp (Thorlabs SLS201L) is used to illuminate the sample, to navigate through and to find the right focal plane. The white light emitted but the bulb is injected into 600 micrometres core step index multimode optical fibres (Thorlabs FT600EMT). The fibre aperture acts as a secondary source, the diverging light is re-collimated by one-inch achromatic doublet f=80mm (Thorlabs AC254-080-Ac). The collimated light beam is then redirected onto a tiltable mirror and then sent into the microscope by using a periscope arrangement. The mobile mirror allows to choose between laser excitation and halogen lamp illumination.

### 3.2.2 BLUE LASER

A diode laser (Becker & Hickl BDL-405 ps/cw diode laser) λ= 403.5 nm, is coupled with our home-made microscope. This device can work either in continuous wave C.W. mode or in pulsed mode, with a pulse duration down to 60ps. The repetition rates available are fixed at 80, 50 and 20 MHz. The light once emitted is redirected by two mirrors into a beam cleaning system.

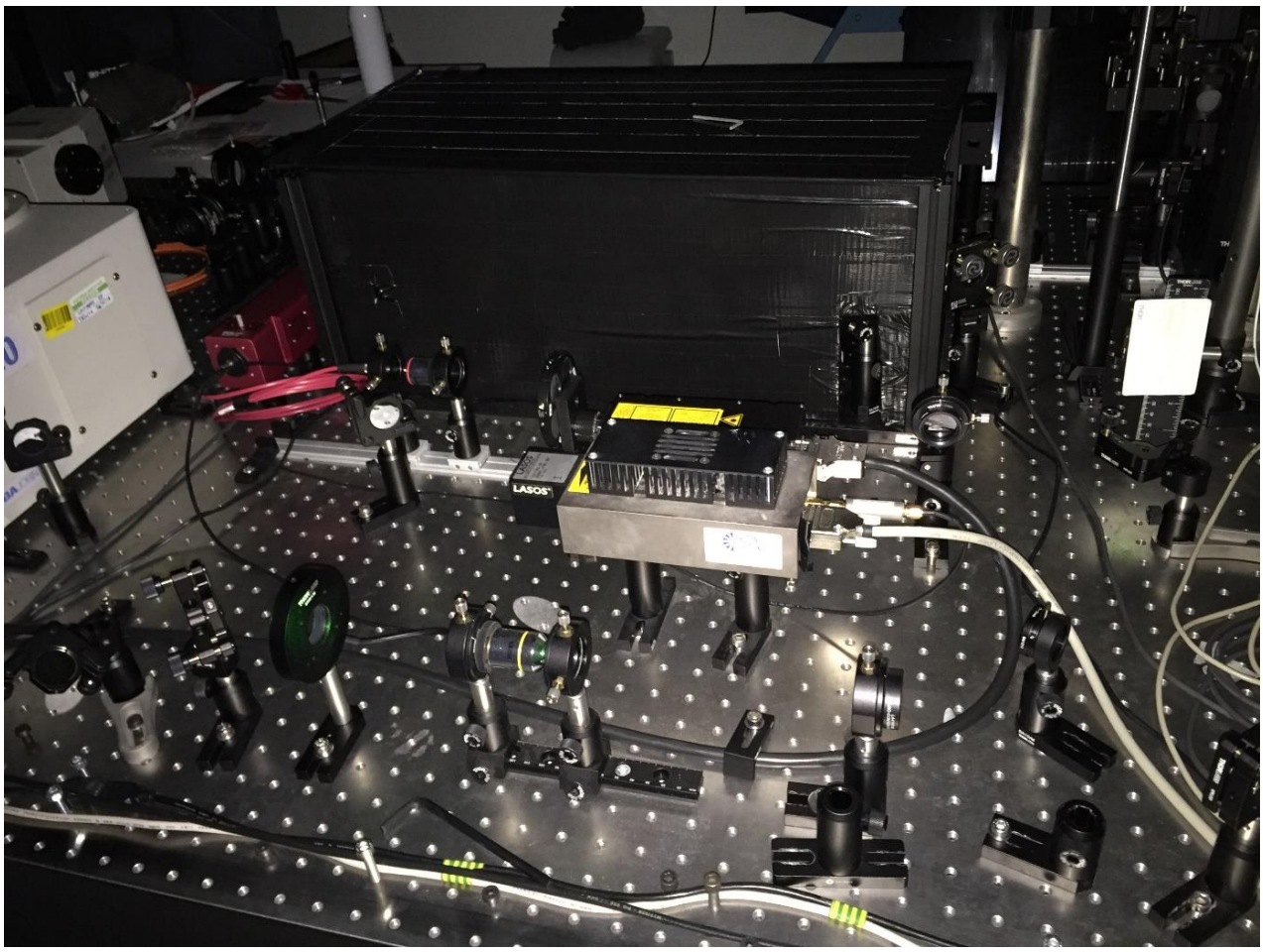

Figure 18 View of the excitation path, namely the halogen lamp, the two laser diodes and the black box containing the super continuum laser and its own splitting group.

### 3.2.3 WHITE LASER

To expand the range of excitation wavelengths, the set-up also includes a supercontinuum fibre laser (Fianium WL-SC-400-15) connected to a monochromator allowing for the selection of a single wavelength. In parallel, the monochromator can be by-passed to take advantage of the whole spectral bandwidth of the supercontinuum laser, depending on the application. The laser has a base repetition rate of 40 MHz, and is equipped with a pulse picker, which makes it is possible to work with repetition rates down to 0.1 MHz. The repetition rate is crucial for application where the phenomenon has a characteristic time much longer than the laser pulse, such has lifetime measurement. The laser spectrum is visible in Figure 19, the large peak around 1100 nm is due to the seed laser.

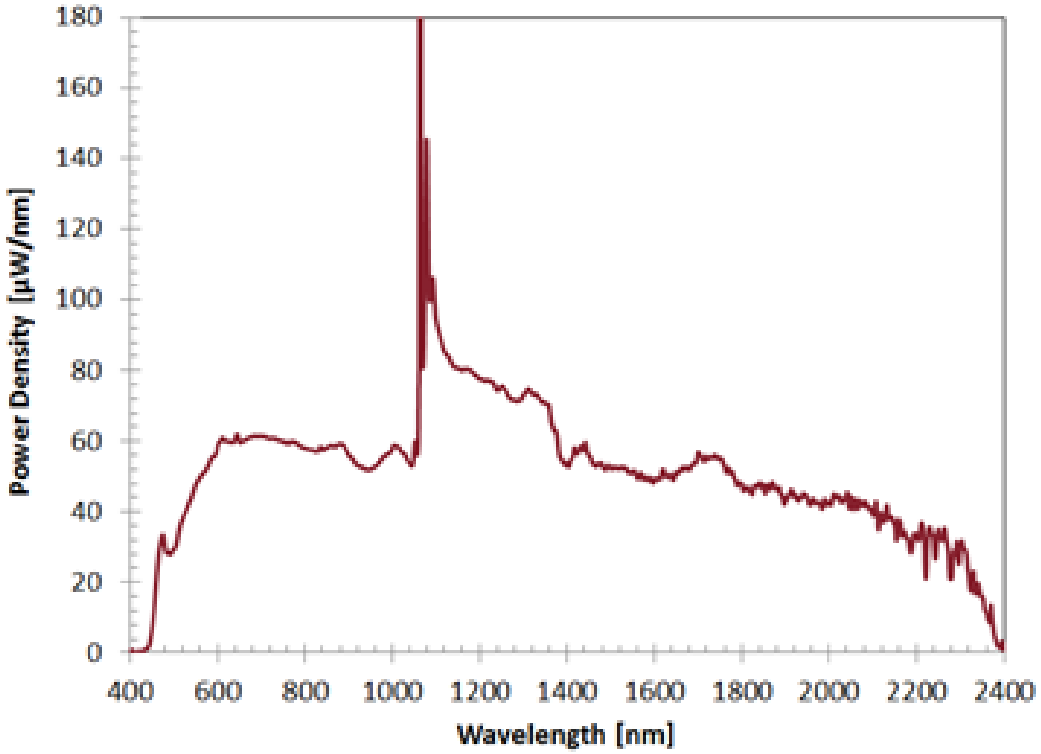


Figure 19 White laser spectrum [1]

The desired laser wavelength can be chosen thanks to a monochromator (Horiba MicroHR single output) or to keep the white light when the monochromator dispersive element is set to zero. In Figure 20 we can see the white light being diffracted inside the excitation monochromator. The laser output fibre is focused onto a MicroHR monochromator entrance slit by a lens f=200mm (Thorlabs LA4102-ML). We intentionally chose a fused silica lens to preserve the broadband spectrum as much as possible. Inside the monochromator two diffractions gratings are installed. The first one has 1200 lines/mm and exhibits the blazing wavelength at 500 nm, the second one instead, it has 300 line/mm and has a blazing at 1200 nm. After this "wavelength selector" device the light in output is collimated by another lens, same model as the one used to inject the light into the monochromator, namely, to obtain an expansion factor of 1. This monochromator system, with the injection and collection lenses, is enclosed into a class 3R laser resistant box for safety purposes. After the monochromator, the laser is safer as a considerable amount of power has been dissipated by the diffraction grating. At this point the laser beam can be either directed with two mirrors into the cleaning system or exit on the side of the enclosure by flipping the last mirror. This side exit is very useful for applications where

[1] https://www.nktphotonics.com/lasers-fibers/2020/01/30/new-superk-fianium-supercontinuum-white-light-laser/

the laser beam shape is not crucial, but the excitation power is, for instance lifetime measurements from liquid samples with low quantum yield.

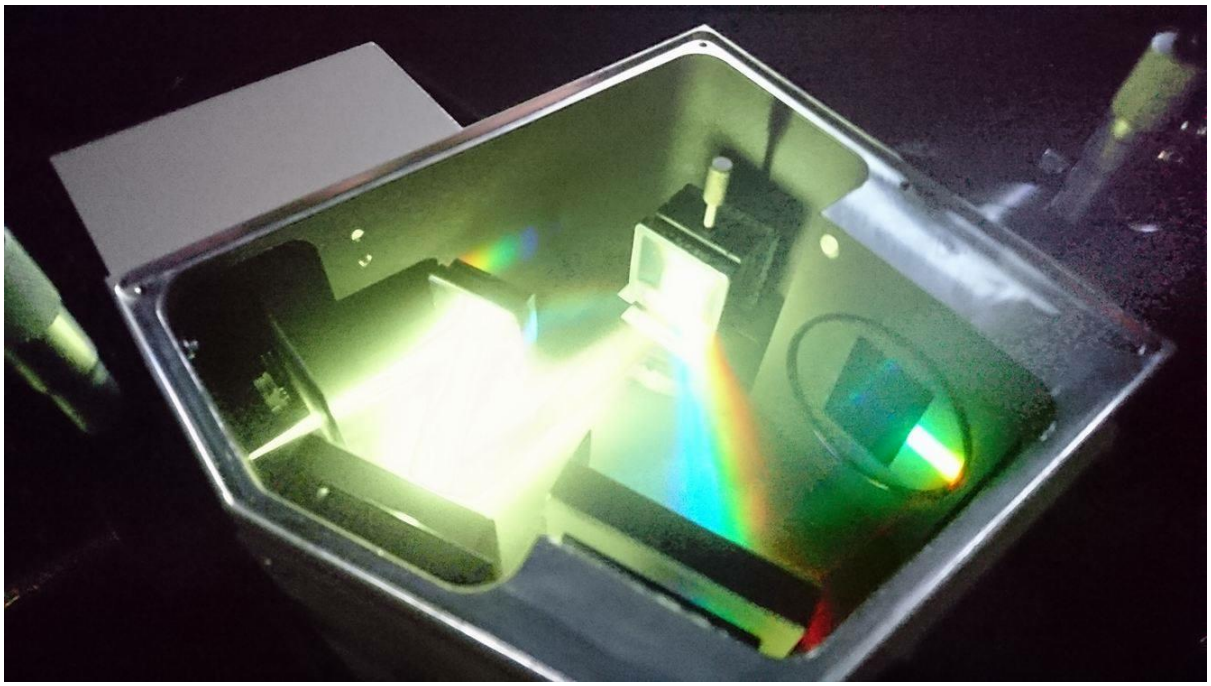

Figure 20 White laser diffraction happening into the monochromator.

### 3.2.4 GREEN LASER

A 532nm Pico laser has been put in place between the two sources described above. This laser is Q-switched with a Nd: YAG/Nd: YVO4 crystal and it has a tuneable repetition rate ranging from a fraction of a Hz to a kHz. The pulse duration is about 1 ns. All these characteristics combined with the high-power output of 2 W make it particularly suitable for experiments involving optical pumping and gaining. All the three lasers described so far are injected into the cleaning system one at time. The selection between the sources is possible by using tiltable mirrors. A more stable solution would have been to use dichroic mirrors, but this has been avoided for three reasons: cost, multiple beams illumination never needed, white laser. A diaphragm shutter (Thorlabs SHB1) is installed before the entrance of the expansion system to protect the sample from the laser light when the illumination is not needed. The shutter aperture is triggered with a TTL trigger pulse sent by the camera or stage. The cleaning system has two functions. The first is to clean the laser beam shape, namely, to remove the ellipticity typical of laser diodes. The second function is to expand the beam to 7mm in diameter to obtain a flat intensity profile across the entrance pupil of the illuminating microscope objective. A 10x Olympus objective focuses the laser onto a 25-micron pin hole (P25D), the diverging beam in output is collimated by a quartz lens f=200 mm (Thorlabs LA4102-ML). For applications in which the laser beam is required to be smaller, a 5x objective can replace the lens above cited.

## 3.3 MICROSCOPE BODY COLUMN

The microscope frame, Figure 21, is made with vibration damped pillars, diameter 2 inch, supporting a manual stage (Newport M-406) with micrometre screws for coarse movements. Onto this manual stage, we have positioned a piezo stage (MADCITY LAB Nano-LP100) with a nominal resolution of 0.2nm for fine positioning and scanning. The remaining components of the microscope are the reflection path, transmission, and collection path.

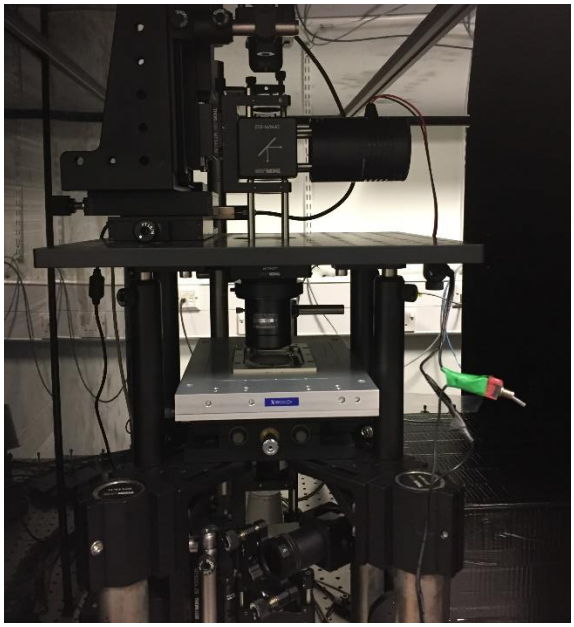

Figure 21 Microscope frame

### 3.3.1 REFLECTION

The heart of the setup is the microscope tower that can work either in reflection or in transmission. The light coming from the sources described before is injected into the microscope objective with a periscope. The periscope has mirrors assembled on a 90 degrees tilter to choose between illumination of the sample in reflection or in transmission. In reflection the light is brought into the bottom objective by using a beam splitter with a reflection transmission ratio of 70% to 30%. Between the periscope and the beam splitter a fused silica plano convex lens f=200mm (LA4102-ML) can be placed in order to inject the light into the back focal plane of the illuminating objective to have the largest field of view (FOV) possible. This injection lens (not shown on the diagram) is assembled on a rail to facilitate the remote focusing into the objective when working with different microscope objectives and it must be removed when working with lasers. To achieve this action the lens holder is assembled with a tilt mount. It is crucial the laser illumination is done without this lens otherwise we would not get a tightly focused spot since the light entering into the objective is not collimated anymore .The condensation lens can be used to increase the size of the Field of View when the sample is

illuminated with white light. The objective holder is obtained by milling to grooves onto a U-bench cage (Thorlabs CB1/M) and it is mounted onto a motorised linear translator (Thorlabs MTS 25-Z8). Moving this linear stage up and down is possible to focus onto the desired surface. The Beam splitter is free to swing in and out from the objective holder since the operation of objective change requires to move the motor to the upper to lower limit. The sample is hold onto a 3D piezo electric stage (Madcitylabs Nano LP100) which allows a lateral resolution on the main axis of 0.1 nm. The Z axis of the stage is used for focussing fine tuning with a keyboard application supplied by the manufacturer. We will see in the detectors paragraph how the piezo stage can trigger the data acquisition while raster scanning the sample.

### 3.3.2 TRANSMISSION

In transmission instead, the beam can be focused onto the sample by using different microscope objectives or plane wave illumination. The top part of the inverted microscope is made of 30x30 $cm^2$ tapped optical breadboard into which a square aperture has been cut in the centre. This part of the frame is versatile and can be configured for the required application. The objective lenses are mounted on a linear motorised stage for increased stability.

### 3.3.3 TOTAL INTERNAL REFLECTION

In addition to the standard reflection/transmission illuminations, an additional mirror (not shown on diagram) positioned on the periscope allows for the laser beam to illuminate the sample with roughly an angle of 25 degrees respect to the slide plane. By placing carefully, a dovetail prism (Thorlabs PS990) onto the sample slide and matching the prism/slab interface with a proper index oils is possible to obtain Total Internal Reflection illumination on the other side of the slide. The lights leaked thorough the sample is scattered into the collection optical path leading to the detectors to be analysed.

## 3.4 K SPACE

The Fourier plane, or back focal plane, of a lens is where the object rays incoming in the same directions are focused in the same point of the plane [88] Figure 22. This plane is located inside the objective for high numerical aperture objectives, but with a system of lenses is possible to extract and expand it Figure 22.

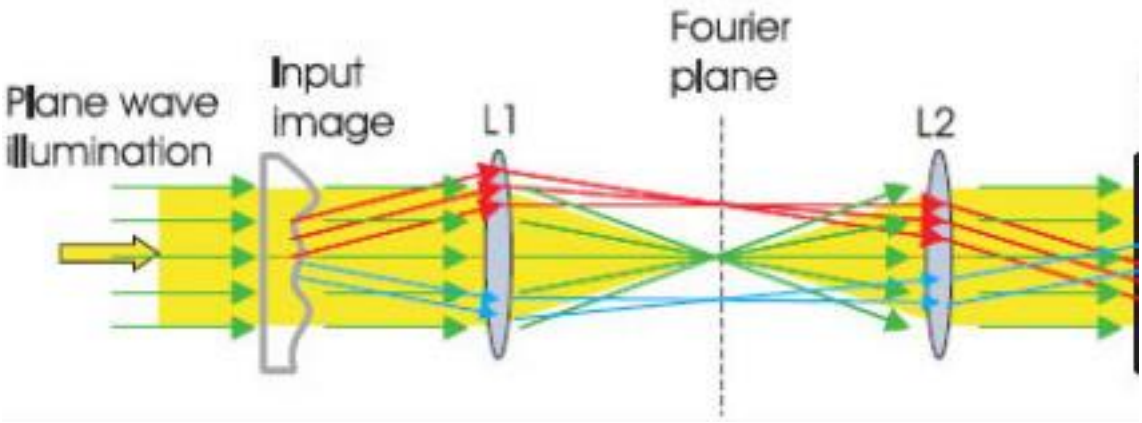


Figure 22 Simple explanation of the Fourier plane, as we can see all the rays impinging the lens from the same directions are focused on the same spot on the Fourier plane [89]

The re-imaging and magnification of the k-space is crucial in case we want to filter some components of the plane, for instance removing the transmitted order. This technique allows us to visualise an angular dependence into a spatial one, which is useful to study the emission or scattering diagrams of nanostructures, fluorophores, or complex photonic or plasmonic nano-antennas. The numerical aperture of the collection objective determines the angular range detectable. The collected light corresponds to a cone of angle 2 NA, and the k-space appears as a circle on the CCD screen. The axis represent angles, and by knowing the wavelength, it is possible to get the in plane component of the wave vector Eq.(53), the z component is missing because it is in the propagation direction of the light. It has been recently proven that k-space imaging can be used to resolve the polarization state of light scattered by a single nanostructure as function of the wave vector [90]. By closing the slit of the spectrometer, and limiting the angular imaging to only one direction, it is possible to resolve spectrally a given part of the k-space. In doing so we can determine which wavelength is scattered/emitted at which angle. In Figure 23 we have a n example of the whole k-space dispersion process. From the relation wavelength- angle (λ, θ), not only do we get information about the directionality of the light but applying a simple mathematical transformation we can easily get the dispersion relation wavevector- frequency (k, ω).

$$\omega = \frac{c}{\lambda} \quad k = \frac{2\pi}{\lambda} \sin\theta \tag{53}$$

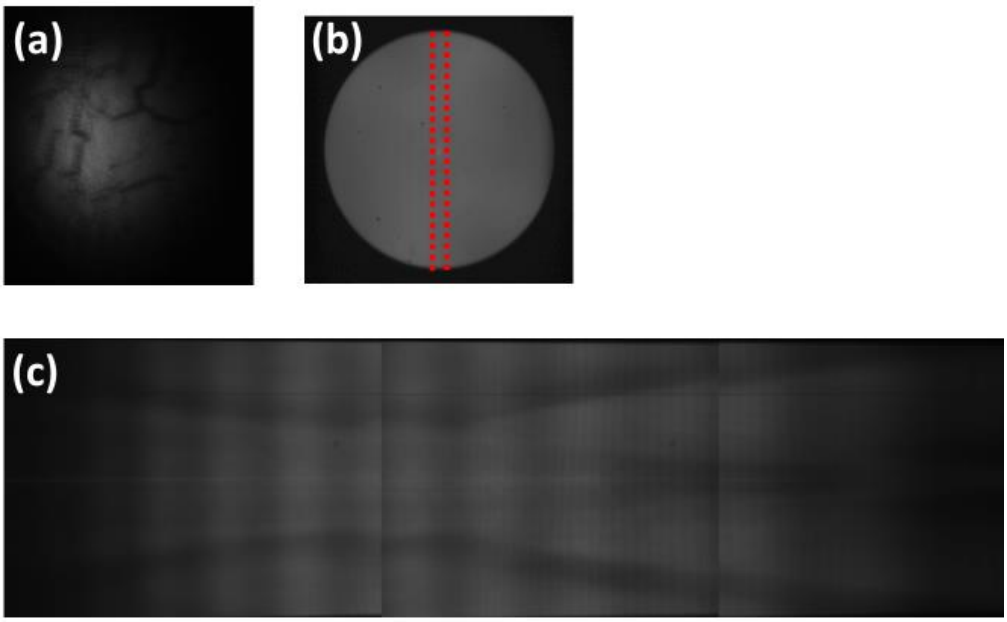


Figure 23 Different views of a polystyrene microsphere monolayer self-assembled on glass. (a) Sample real image. (b) K-space image. The red lines represent the monochromator slit. (c) Spectral dispersion of (b). Three images have been stitched together to cover the range 400-800 nm.

## 3.5 COLLECTION PATH

The collection path is common for all the illumination modes afore described Figure 25. At the other end of the U bench holding the objective is carefully vertically placed a tube lens, achromatic 2" doublet, (Thorlabs AC508-200-A-ML) f=200mm labelled as Lens 1. The lens is connected with a 30mm to 60 mm cage system for maximum stability. The choice of bulky 2" optics comes from the need to minimise the spherical aberration typical of imaging systems using optics with high curvature radius, the so-called fisheye effect. The cemented doublets instead of simple lenses to get rid of the characteristic chromatic aberration of single lenses when working with multiple wavelengths. All the collection optics lenses have these characteristics. Lens1 is used to focus the image the focal plane onto the so labelled Real plane where a CMOS camera can be placed and to extract and collimate the objective back focal plane. This plane represents the object of the imaging system from the lens 2 into the detection system. A pinhole can be placed in the Real plane, doing so, it is possible to shrink the collection area, effectively transforming the system into a confocal microscope. The lens 2 (Thorlabs AC508-300-A-ML) f=300mm collimates the real image plane and re-images the Fourier plane into the Fourier planeKF Figure 17. In this plane different wavelengths are focused on different angles.

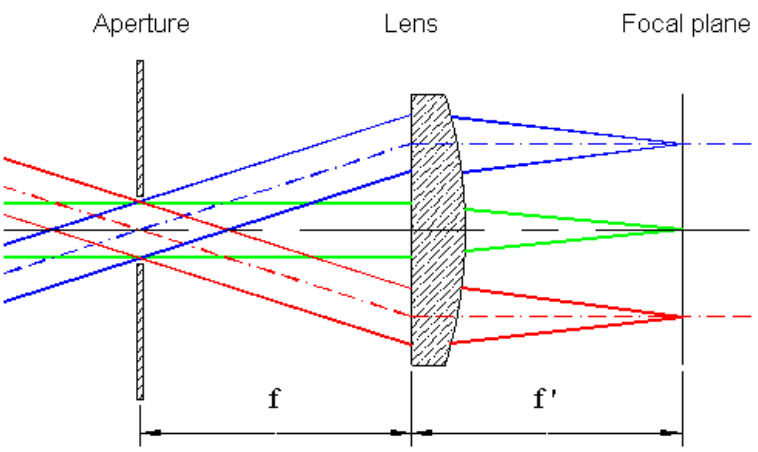


Figure 24 Representation of the Fourier plane for a ray bundle coming from the real plane passing through a pin hole filter.

In KF, it is possible to carry out spatial filtering to eliminate unwanted objective collection angles. The Fourier lens (Thorlabs AC508-350-A-ML) f=250mm collimates the k space, this lens is assembled onto a rail and it is mobile, when it is in, the k space is imaged, when it is out the real plane. The last lens L3 (Thorlabs AC508-300-A-ML) f=300mm images whatever plane sent onto the entrance slit of the detection monochromators where the detectors are attached. The collection path has been designed with free space optics; therefore, it is highly accessible making the spatial filtering easy. All the collection optics are optimised for visible applications, but it is possible to change them to work in the near infrared without affecting the whole alignment.

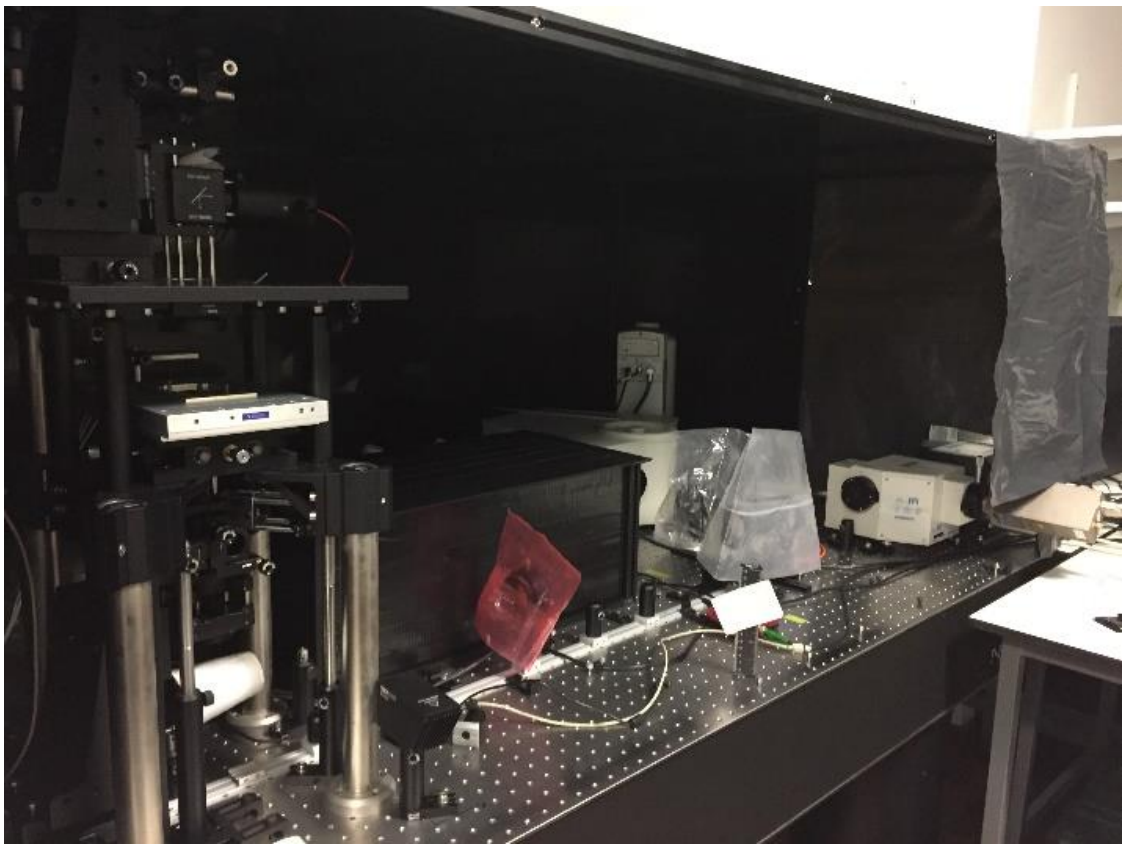

Figure 25 Overview of the collection path and the final detectors.

## 3.6 DETECTORS

The setup has been designed to work both in the visible and in the near infrared, therefore both kinds of detectors are present. To sweep from NIR to visible mode it is needed to remove a cube mirror. For both spectral range we have a system to measure the spectra and a single photon counter for time resolved applications. The visible path is made of a Horiba microHR connected to a photomultiplier (Becker & Hickl HPM100) and a high- resolution EMCCD (Princeton Instruments ProEM-HS 512). The NIR detectors are connected to another monochromator (Horiba iHR320), we have a linear array spectrometer (Horiba Synapsys II) on the side exit and a fibre-coupled single photon detector (PicoQuant) on the front exit.

## 3.7 EXPERIMENTAL TECHNIQUES

With the set-up described above, many types of measurements are possible such as k space imaging, confocal detection, fluorescence emission, fluorescence emission hyperspectral imaging and lifetime.

### 3.7.1 SCANNING MEASUREMENTS

The xyz piezo electric stage allows to raster scan the sample and during it is possible to probe the sample in multiple way such as reflection, transmission, scattering, absorption. A spectrum can be collected at each point, in this case we are talking about hyperspectral imaging. The sample can be observed in fluorescence as well. Fluorescence Lifetime Imaging Microscopy (FLIM) is possible too both in spectrally resolved mode or in "plain mode" if using the monochromator grating at zero degree. It is possible to resolve the emission spectrally and measure it as hyperspectral image. This technique is particularly useful when we want to study spectral changes across the scan. These measurements are possible both in real and Fourier plane.

#### 3.7.1.1 HYPERSPECTRAL IMAGING

This imaging technique consists in scanning the sample with the piezoelectric stage and collects a spectrum on each point of the scan. The confocal detection reduces drastically the collected area from the sample; therefore, the scanning step must be carefully chosen. We want a total area coverage, so the stage step must be the same order or smaller of the laser spot. Every time the piezo stage moves the x axis, a trigger pulse is sent to the trigger input of the PI CCD, which records a spectrum. The TTL output of the camera sends a 5 V pulse to the laser shutter to open before acquiring the first frame and one at the end of the scan to close it. The number of pixels in the raster scan must be equal to the CCD frames to acquire. The data from these kind of measurements are recombined to generate hyperspectral images by arranging into an image where all the points represents the intensity detected at single wavelength per scanned point.This specific feature of the experimental setup has been widely used by my colleague and friend Dr. Abdullah O'Hamza in his thesis [87]. Photobleaching is the main issue when working with this technique, the optimal laser power needs to be determined before scanning the sample. This method works for white light measurements, fluorescence, scattering etc. All the data are elaborated through a homemade GUI MATLAB code. With this instrument it is possible to map an area and extract the spectrum measured in that point, significantly simplifying the experimentalist work.

#### 3.7.1.2 FLUORESCENCE LIFETIME

Fluorescence Lifetime Image Microscopy (FLIM) is widely used to investigate the interaction between plasmonic entities and the surrounding environment [91], quantum emitters for example. It is an imaging technique based on the differences in the exponential decay rate of the fluorescence [92]. In this this kind of microscopy the pixels of the image are made by the lifetime of the fluorophores in that spot rather than the number of photons itself. The main advantage of this technique is to reduce the photons scattering [93] other than obtaining an

image from samples with low Quantum yield. The features on the image are visible only because there is a contrast, in terms of decay rates between the different features into the image. This principle works even if the imaged features have fluorescence at the same wavelength. The operative workflow of lifetime measurement is based on counting the number of photons emitted by the sample after interacting with a laser pulse. The detector signal measured with an oscilloscope is totally different with the expected waveform Figure 26a. We can see how it consists of only few pulses arbitrarily spread over the time axis Figure 26a-c. Each of the pulse represents the single photon detection event of the fluorescence signal. Doing so, the fluorescence waveform Figure 26 (a-c) must be considered a probability distribution [94]. The raw traces as seen by the detector consists of a train of randomly distributed pulses corresponding to the detection of the individual photons.

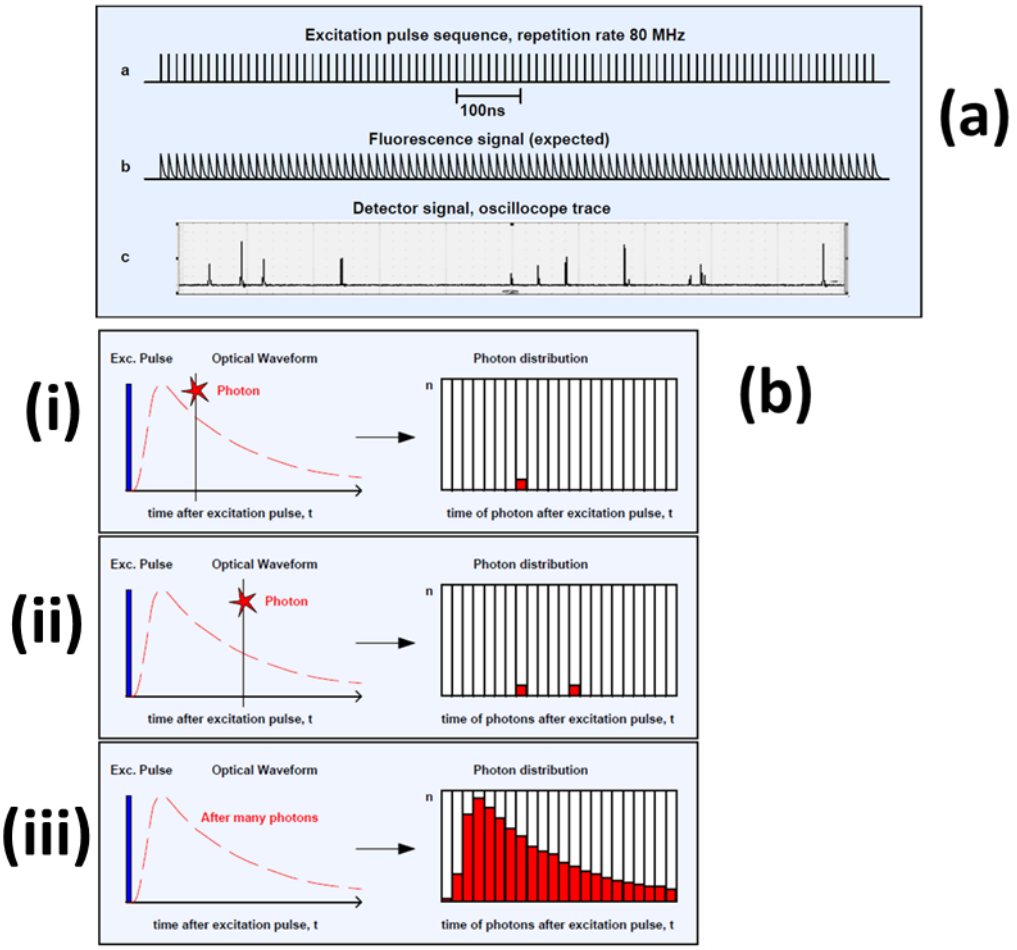


Figure 26 (a) Detector signal for a fluorescence detected with a pulse rate of 80 MHz from [94], (b) Principle of TSPC, (i)Original waveform, (ii) Single photon detection over different excitation-emission cycles, (iii) Histogram built at the end of N cycles [94]

Few of the collection periods are with no detected photons Figure 26 b, other signal periods contain one photon pulse. When a photon is detected, the arrival time of the corresponding

laser pulse in the signal period is measured. After many signal periods many photons have been detected, and the statistical distribution of the photons over the time in the signal period builds up [94].

The lifetime curve is mapped using data acquired through many excitation-emission cycles to build the decay histogram. Exciting an ensemble of emitters with an ultrashort, ideally a delta like pulse of light, the fluorescence signal in the time domain decays exponentially. However, it is impossible to produce a delta pulse, since we are limited by the number of harmonics we can sum experimentally. The pulse always has a certain duration (roughly hundred picoseconds in our system), therefore the observed time signal fluorescence, d(t), is going to be the natural fluorescence exponential decay convoluted to other components due to the hardware limitations. To solve this issue, it is necessary to measure the so-called Instrument Response Function (IRF) which allows to determine all those unwanted components in the detected fluorescence lifetime signal. The IRF is the pulse shape the FLIM system records for an infinitely short fluorescence lifetime [94], it needs be convolved with the decay function, F(t) to get the real measured fluorescence d(t):

$$d(t) = IRF(t) \otimes F(t) \tag{54}$$

The curve so obtained needs to be fitted with the proper mathematical model to obtain the lifetime. The more widely used models are single, double and, sometimes, triple exponential decay. The number of exponentials needed depends on how many lifetimes there are in the photon's population. There are several techniques to measure the population of photons after the pulse, our system is equipped with a Time-Correlated Single-Photon Counting (TCSPC). This tool is basically a photomultiplier that measures the photocurrent induced by the incoming photons coupled with the pulsed laser and the control electronics. The time resolution of such a device can be up to 4 ps and the collected data obeys Poisson statics, where the $\chi^2$ parameter is used to evaluate the goodness of the fit. The TCSPC records the times at which all individual photons are detected with a delay after the single pulse. Repeating the counting for many pulses and after enough recorded events, we can finally have a statistic. We build a histogram of the number of events across all these recorded time points. This curve is the d(t) described earlier. This histogram is therefore fit to a single or multi exponential functions containing the exponential lifetime decay function of interest. The lifetimes are the coefficients of the exponential factors.

All this process must be repeated for each pixel of the image. To build a 2D image, this procedure is repeated at different points on the sample using a galvanometric-mirrors pair or

resonant/galvo to raster scan the excitation spot or, as in our case, a piezo electric scanning stage that sends a pulse to trigger the acquisition after the sample has been moved to the next position. A piezo-electric scanning stage was chosen over scanning mirrors as, despite being slower it allows to keep the illumination k-vectors constant throughout the scan as opposed to the angular deflection induced by the galvo-mirrors. This consideration is important when dealing with photonic systems, especially plasmonic ones, where the optical response can be highly dependent on the incident wave vector.

#### 3.7.1.3 FLUORESCENCE AND CONFOCAL DETECTION

The fluorescence is excited by focusing the laser onto the sample, the light collected it is made by both the reflected laser and the fluorescence signal. The laser trace is cut with a low pass filter to allow just to the emitted light to reach one of the detectors. The confocal detection is realised with a pinhole mounted in correspondence of the real focal plane. This technique is still diffraction limited, but it allows to improve the microscope resolution as the area from which the signal is significantly smaller. The confocal detection can be used either to collect a very precise spectrum or to reconstruct an image with the technique of the hyperspectral imaging.

### 3.7.2 PHOTOLUMINESCE EXCITATION SPECTROSCOPY

The monochromator coupled to the white laser offers a wavelength selection which is used to record Photoluminescence in excitation (PLE) 2d maps. In this technique we record the emission from the sample as a function of the excitation wavelength. The different excitation wavelengths are provided by white laser combined with its own monochromator. Once acquired the first spectrum the Labview code increases the excitation wavelength by the wanted delta until reaching the final desired wavelength. The data is arranged into a 2D map, like in Figure 27, with the emission spectra on the x-axis and the corresponding excitation wavelength on the y-axis. This technique is particularly useful when determining the best excitation wavelength for a fluorophore.

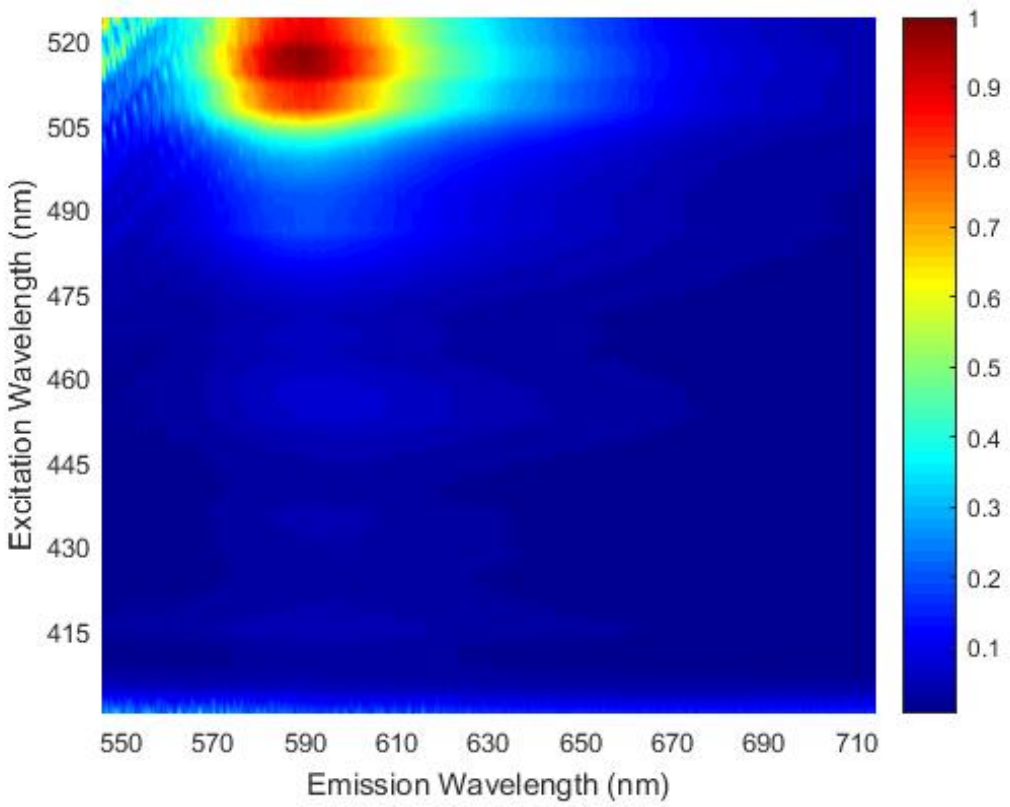


Figure 27 PLE measured onto a hybrid nano cavity made by a layer of Lumogen red onto a DBR. Excitation sweeping from 405 to 520 nm.

### 3.7.3 MEASUREMENTS FROM LIQUID SAMPLES

The same set-up can be used to directly study samples in solution which do not necessarily demand a high spatial resolution. Our collaborators often synthetize innovative quantum dots or plasmonic systems in liquid solution which we study on this set-up by positioning a standard quartz cuvette to contain the liquid into the focal point of lens 2, the same location where we filter with the pinhole. The collection configuration remains unchanged, acting as a 2-lens system to collect the emission from the sample and focus it onto the spectrometer entrance slit. The sample excitation is provided with side illumination, though a flip mirror that makes the laser bypass all the periscope group. With this technique we can measure fluorescence spectra, lifetime, and scattering spectra. This part of the setup has been used to validate the setup configuration Figure 28. During my PhD, I have been performing measurements for collaborators (amongst others, Dr Charlotte Elling and Dr Mitchell Clark, which led to several publications [95]-[96], [97]). In Figure 28 an example of measurements from samples in liquid.

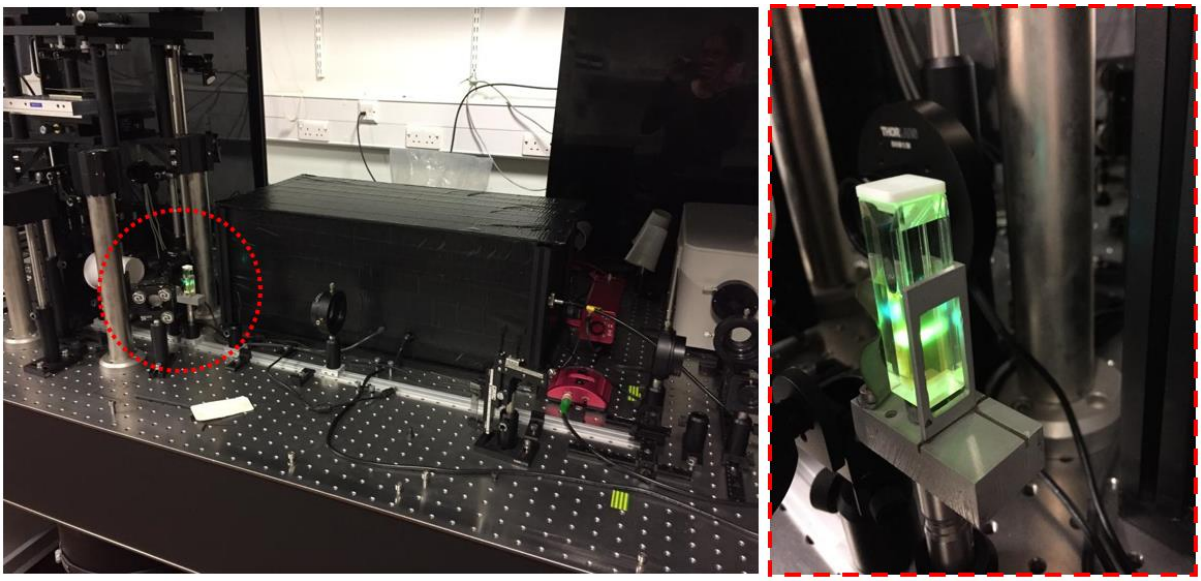

Figure 28 Fluorescence from green quantum dots in Hexane solution, inset zoom on the cuvette. Green QDs, laser at 403nm. The results of these studies are reported here: [96]

## 3.8 INTEGRATTION INTO A SINGLE GRAPHICAL USER INTERFACE, CONFIGURATION, AND CALIBRATION

In this section we describe all the software written to integrate the various hardware (monochromators, lasers sources, detectors, motorised translation stages… etc) into a single graphical user interface, as well as the necessary calibrations measurement, necessary for the validation of the system.

### 3.8.1 SINGLE GUI SOFTWARE

To integrate all the microscope components, LabView was used due to being a well-established platform as well as enabling simple communication between all the elements. In a single piece of software, it is possible to control all the objectives focus manipulators, all the three monochromators, the CCD data acquisitions, the laser shutter, and the white laser options such as power and repetition rate. The lifetime setup, the stage and the 405 nm laser are installed on another computer, the two separate parts are connected via external triggers. The software frame is a standard State Machine. For the sake of simplicity, only the front panel is shown here Figure 29, which is what the standard user has access to.

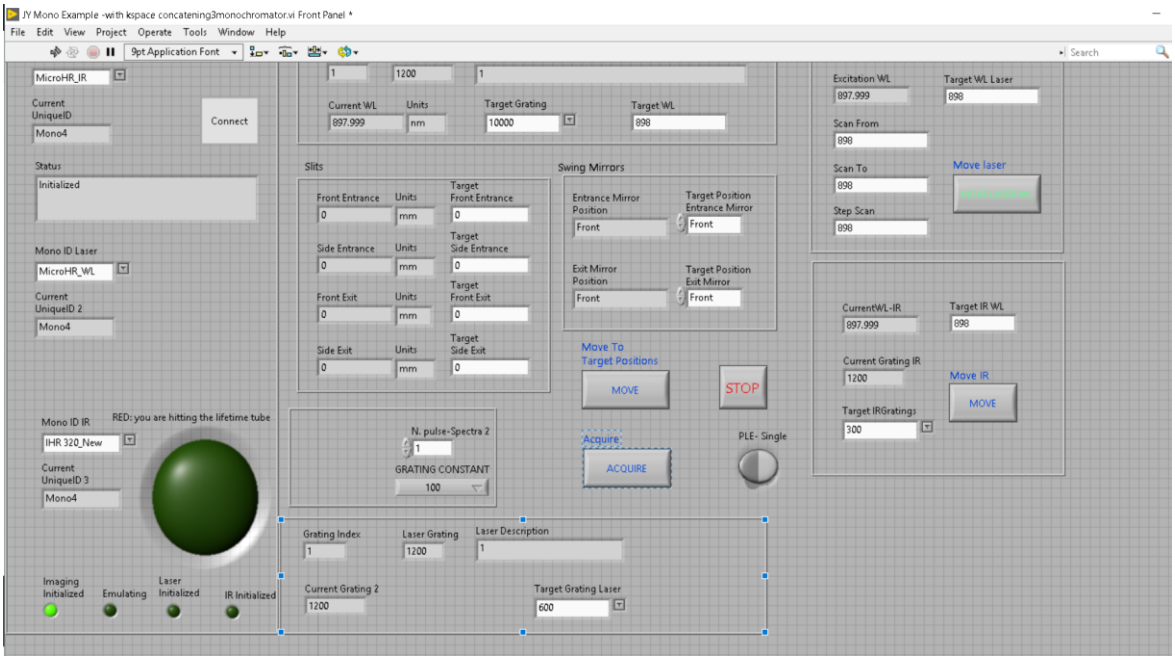


Figure 29 Front panel of the LabView control code for the microscope.

### 3.8.2 INSTRUMENTS CALIBRATION

The spectral calibration process was performed for all monochromator gratings and CCD. A Na lamp is used to calibrate the high-resolution grating (1200 lines/mm) as the Sodium has an emission doublet at 580 nm with a spacing of only 0.9 nm between the two lines [98], commonly called Sodium doublet Figure 30. Knowing the spectral shift between the lines and the number of pixels on the CCD, we can easily get the calibration factor, 0.06nm/pixel. The visible and NIR diffraction gratings are calibrated using a Cd-Hg lamp which exhibits multiple emission lines in the visible and near infrared part of the spectrum. Life-time instruments are calibrated by the supplier companies by default, but before performing any research measurement we double checked their correct functioning using a dye with a well-known decay: we regularly used Lumogen Red, Rhodamine 6G, or Rhodamine B in specific solvents. The values measured are then compared with the ISS fluorescent lifetime list available here [2]. In Figure 31 the lifetime measurement of Rhodamine B in aqueous solution was measured as 1608ps, with excitation at 405nm. This obtained value is very close to the 1680ps exhibited in the ISS list cited above.

[2] http://www.iss.com/resources/reference/data_tables/LifetimeDataFluorophores.html

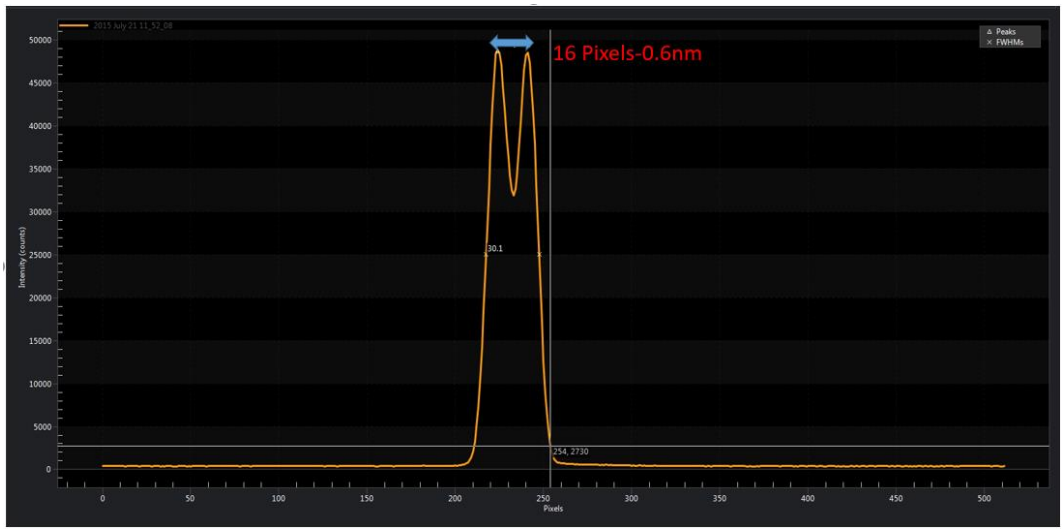


Figure 30 Example of spectrometer calibration spectrum. In this case Na lamp. This is the spectrum as shown on the Light Field screen.

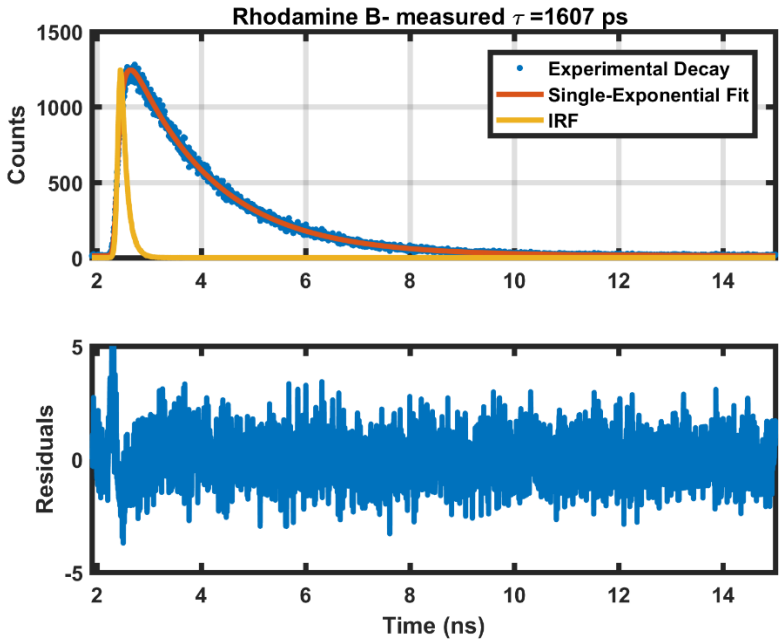


Figure 31 lifetime validation measurement. Rhodamine B dissolved in water. In the top graph: blue dots experimental decay, in orange the fit, in yellow the IRF. Bottom graph residuals

## 3.9 CONCLUSIONS

In this chapter, the experimental setup used to probe the light-matter interactions have been discussed.

All the components of the setup such as excitation path, microscope, and detectors have been discussed. Each single technique used this thesis such as the hyperspectral imaging, fluorescence, PLE (photoluminescence excitation), k-space imaging, FLIM and lifetime and

confocal detection has been widely described. The front panel of the LabView control code has been shown as well. Some calibrations measurements have been showed as well especially for the Sodium doublet to deduct the diffraction grating/ccd pixel calibration factor. A cuvette filled with Rhodamine B dissolved in water was used to double check the lifetime calibration. These calibration steps were an obliged step before carrying out any novel physics related experiment.

# Chapter 4 VALIDATION AND APPLICATIONS OF THE MICROSCOPE

In this chapter we present a range of applications, peripheral to the main work reported in this manuscript, that have been investigated in collaborations with other members of the research group and that used the instrument developed as part of this PhD work, described in chapter 3. The work described in this chapter led to two publications. In this chapter we present some innovative InP/ZnS ultrabright quantum dots both in organic solvents and water. We then present a dual Fluorescence/Raman nano probe that can be used both for bioimaging and as pH sensor with optical response. We will describe studies of FRET modifications process that occur inside a silver nanogap. The chapter ends with a study of silicon nitride micro resonators. The original purpose of this system was to generate nano lasing with some organic polymers, and we present here their optical isolated response using hyperspectral imaging.

## 4.1 SUPER BRIGHT INDIUM PHOSHIDE QUANTUM DOTS

This work was carried out in collaboration with Dr Stasiuk's group in the Department of Biomedical Sciences at the University of Hull with Dr. Mitchell Clarke. Quantum dots are usually made with heavy metals such as Lead or Cadmium. These metals are heavily toxic therefore rendering the resulting QD unsuitable for bio-medical application. Recently bio-compatible quantum dots have been developed to fulfil this lack of nontoxic QD. One alternative material that can be used for such systems is Indium Phosphide [99], [100]. QD are synthetized in organic solvents such as Hexane, however for biological application a transfer to water is required. A huge drawback of quantum dots is their low photoluminescence quantum yield when they are phase transferred to water, usually less than 5%. In a collaborative study, Dr. Mitchell Clarke synthetized novel InP/ZnS QDs based. This low value is due to solvent quenching and surface states. This is typically mitigated with a shell to passivate the surface defects. If the shell is not covering completely the core, the whole surface is not passivated, and the core is not completely protected from the solvent quenching. Four different fabrication techniques have been compared in this study: (core InP only, 1st growth named InP/ZnS(1) , 2nd growth after cooling step InP/ZnS(2), and growth of thick shell in one step InP/ZnS(3). In InP/ZnS(1) a ZnS shell is added to the InP core, with InP/ZnS (2) a cooling step is added to the fabrication process before adding a second ZnS shell to the already coated InP/ZnS quantum dot. The last sample InP/ZnS(3) a thicker shell is grown in one step for a total thickness of first and second shell together.

The difference with the previous fabrication method an extra cooling step was added to equilibrate the ZnS shell across the core. This step allowed us to obtain the highest reported quantum yield so far for those QD, with 85% in hexane and 57% in water. The quantum yield was measured using the technique of the integrating sphere coupled with a Horiba Fluoromax spectrofluorometer [101]. Knowing that the lifetime is the inverse of the total decay rate, it is possible to calculate both the radiative and non-radiative decay rates using the relations:

$$\Gamma_{nr} = \frac{\Gamma_{rad}}{QY} - \Gamma_{rad} \qquad \tau = \frac{1}{\Gamma_{rad}+\Gamma_{nr}} \tag{55}$$

Where $\Gamma_{rad}$is the radiative decay rate, QY the quantum yield and $\tau$ the quantum dot lifetime. The synthesis is detailed in the corresponding publication [96]. The contribution given by this thesis was to characterise the lifetime. Synthesis of the InP core requires the use of both $Zn_2$+and $In_3$+ precursors. It has also been demonstrated that the emission ranges from 525 nm to 620 nm [102]. The $Zn_2$+precursor ($ZnCl_2$) is used in the initial reaction solution to passivate surface defects and trap states during InP core growth [103]. It was proved that it is possible to grow ZnS shells 10 nm thick around InP cores using an aminophosphine [104]. This is possible because there is not a thin layer of oxide onto the surface of the InP which is the main responsible for not allowing the growth of the shell. The novelty of this study was to have a cooling step in between the two shell fabrication processes. This extra step allows to the atoms to diffuse on the core surface and to create a more homogeneous shell by passivating the surface defects. At the beginning of the process the InP cores have an average diameter of 2.48 nm.

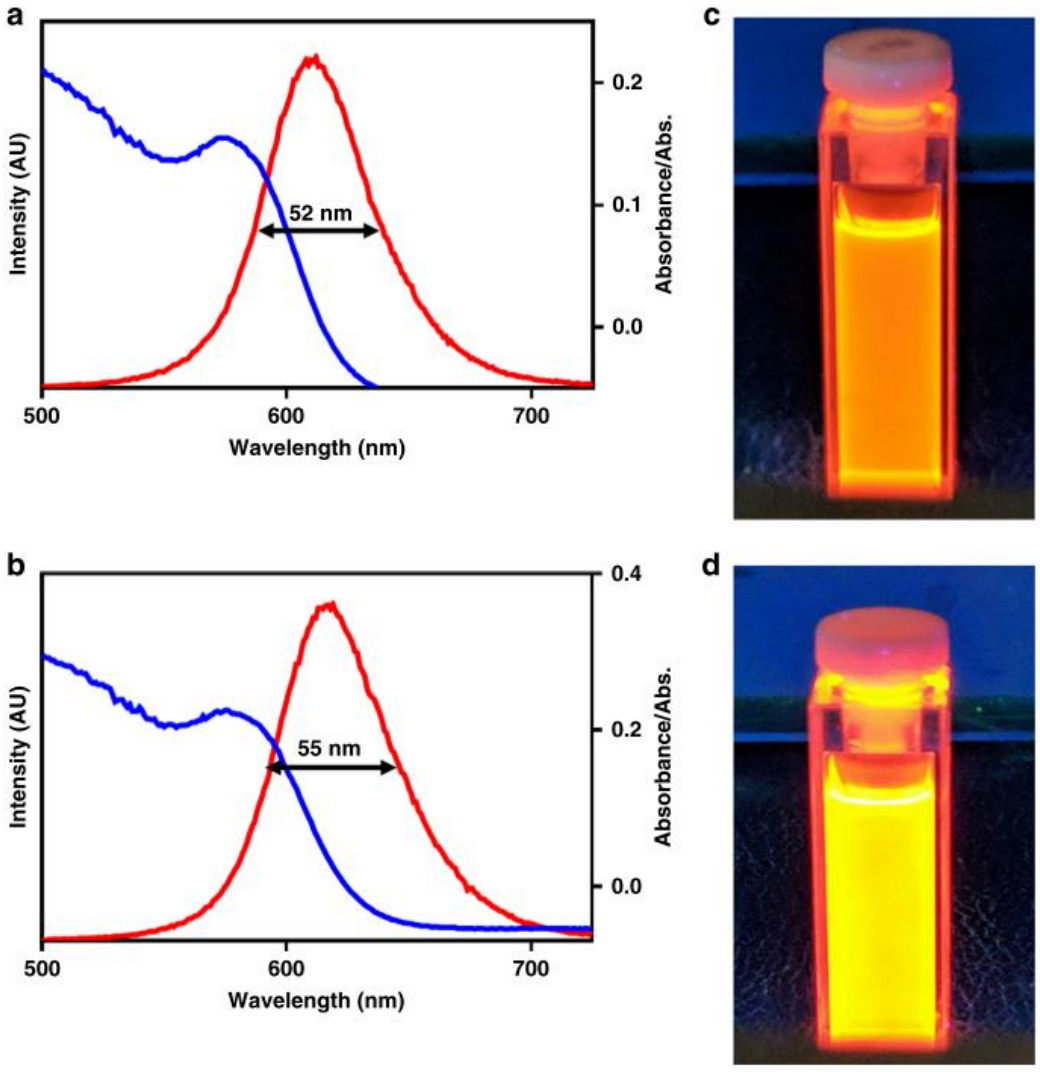


Figure 32 Photophysical properties of InP/ZnS (1) and InP/ZnS (2). a, b Absorption (red) and emission spectra (blue), along with the full width at half maximum InP/ZnS (1) (a) and InP/ZnS (2) (b). c, d luminescence of (c) InP/ZnS (1) and (d) InP/ZnS (2) under black light illumination (365 nm). Image from [96].

After growth of a first ZnS shell, the peak emission for InP/ZnS (1) was observed at 613 nm with a full width at half maximum of 52 nm Figure 32(a-c) with a QYof 40–49% in hexane. Furthermore, we obtain a diameter growth from 2.48 nm to 2.67 nm upon the addition of the first ZnS shell. The next step was to add a second shell. The synthesis of InP/ZnS (2) was carried out by means of thermally controlled cooling exhibit significantly increased QY (Figure 32). This second shell growth results in an average increase in size from a diameter of 2.67 nm to 2.75 nm. The (InP/ZnS (2)) that have this addition layer, exhibit an improved QYcompared to InP/ZnS (1) with a QYranging from 75% to as high as 85.3% in hexane, compared with a previous max value of 49%. This is the highest QYobserved for InP/ZnS-based QDs to date [96]. This large increase of the emission performances is due to the ZnS passivation of the defect sites on the

InP core. This process inhibits some non-radiative decays paths, therefore increasing the PLQY. The main goal of this study was to develop ultra-bright quantum dots to be used for bio-imaging applications, therefor the behaviour in water needs to be assessed.

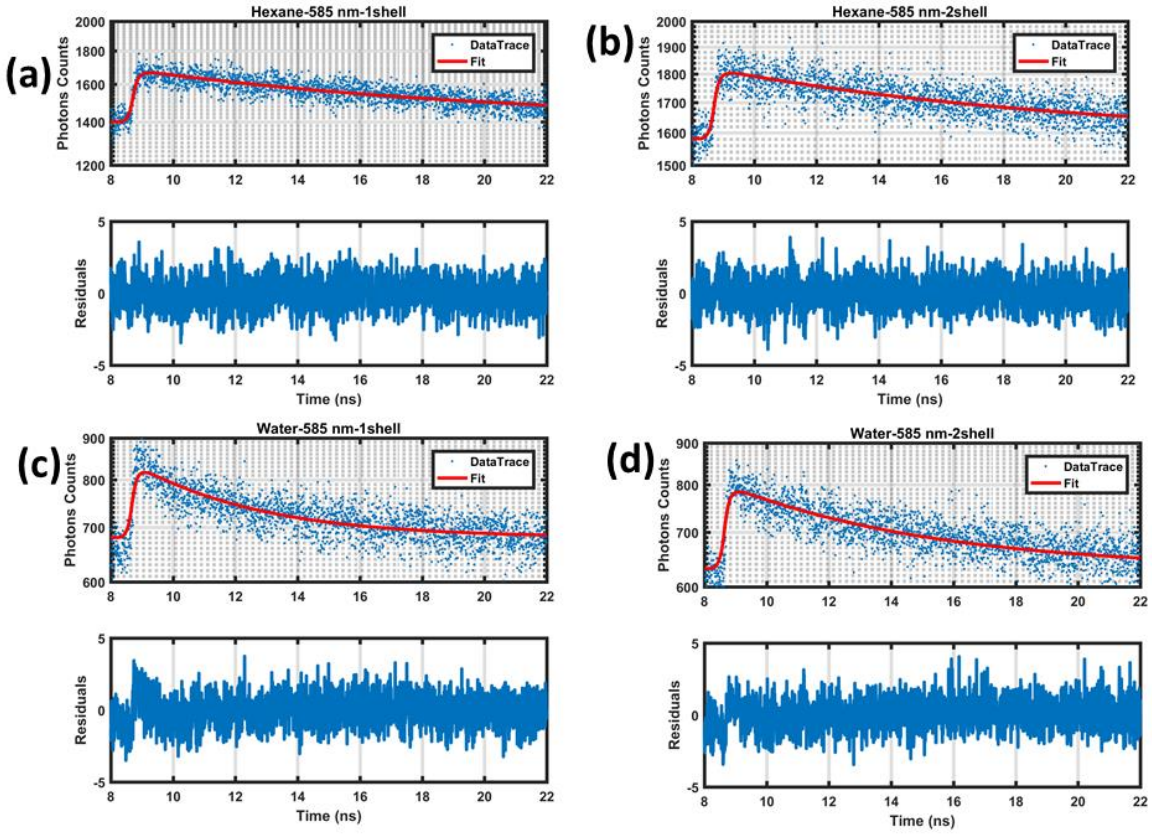


Figure 33 Lifetime curves measured for 585 nm peaked emission QDs:( a) single shell-Hexane, (b) double shell Hexane, (c) Single shell Water, (d) single shell Water showing both the time decay and the residuals.

The first step is to transfer the QDs in water using thioglycolic acid (TGA) as the transfer ligand. In water, the quantum yield was found to have of 57% which is higher than any other InP/ZnS quantum dots in water. Lifetime measurements in water show two decay pathways

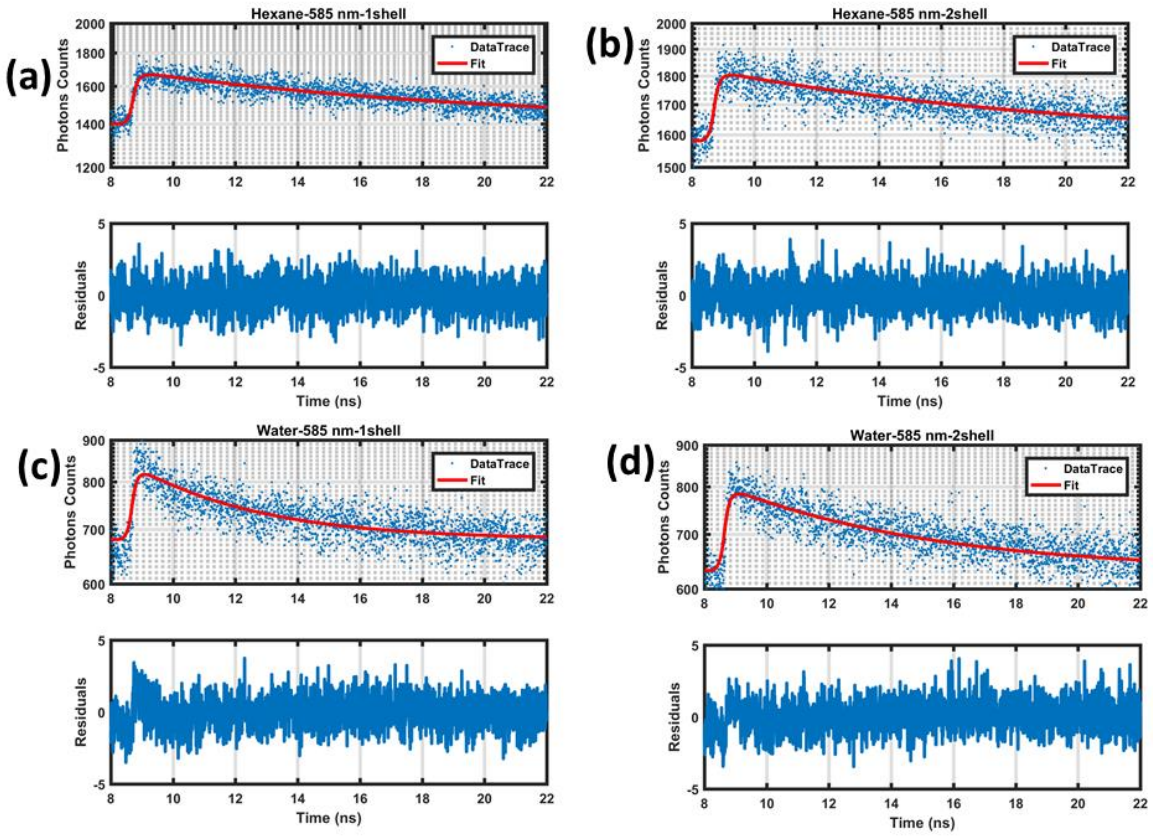


Figure 33 one slow and one fast. The slow component ranges around 15–17 ns, like the QDs in Hexane. However, the fast paths ranges from 0.7 ns and 1.4 ns for one and two shells, respectively. This shows a decay path via solvent oscillators Figure 34. The weight between the two components of the lifetime depending on the ZnS coverage. For InP/ZnS (1). In average the faster component is 1.413 ns with a weighting of 47.18%, instead for InP/ZnS (2), 0.708 ns at a 27.62%. This means that InP/ZnS (2) has a lower solvent quenching by $H_2O$. The increase of the weight for the slow component in the InP/ZnS (2) is directly corresponding to higher QY. Moreover, the lifetime decay allows us to determine the radiative and non-radiative decay rates for each compound. The values are shown in Figure 34. We can see how in InP/ZnS (2) the radiative decay rate doubled compared to InP/ZnS (1) whereas the non-radiative decay rate was reduced by a factor of 3.7. This is an evidence that the solvent quenching is reduced, and the shell is passivated in a more efficient way.

| QD | Zn:In ratio[a] | Diameter[b] (nm) | $\lambda_{em}$ (nm) | PLQY $\Phi$ | Lifetime (ns) | $\Gamma_{rad}$ ($ns^{-1}$) | $\Gamma_{non\text{-}rad}$ ($ns^{-1}$) |
|---|---|---|---|---|---|---|---|
| **InP** | 37:63 (±1.27) | 2.48 ± 0.45 | — | — | — | — | — |
| **InP/ZnS(1)** | 57:33 (±1.36) | 2.67 ± 0.48 | 613 | 49% | 19.7 | 0.025 | 0.026 |
| **InP/ZnS(2)** | 73:27 (±0.28) | 2.75 ± 0.45 | 623 | 85.30% | 20.5 | 0.042 | 0.007 |
| **InP/ZnS(3)** | 89:11 (±0.11) | 2.88 ± 0.49 | 611 | 47% | 22.1 | 0.021 | 0.024 |

Figure 34 Properties of the InP/ZnS in Hexane measured at different shells numbers [96]. InP is the QD core, InP/ZnS(1) the QD with single shell, InP/ZnS(2) double shell with cooling step and InP/ZnS(3) is the QD with thicker shell grown in one step.

This study developed a new to make super bright and non-toxic InP/ZnS in water for biomedical applications. This method simplifies the fabrication process by eliminating the glove box since relying on Schlenk line techniques only. The highest quantum yield recorded is 85% in Hexane. After a phase transfer to water, the quantum yield measured is 57%, is the highest quantum yield ever recorded for InP/ZnS QDs in water so far. In terms of lifetime, we discovered that the two shells Quantum dots have fewer solvent oscillations when in water.

## 4.2 DUAL MODE PLASMONIC PROBE FOR FLUORESCENCE AND SERS APPLICATIONS

This work was carried out in collaboration with my colleague Dr. Charlotte Eling. The contribution of this thesis was to perform the lifetime measurements for the novel plasmonic probes. The purpose of this work was to create a dual-mode probe for mitochondria imaging using functionalised gold nanoparticles with a rhodamine B based ligand.

The rhodamine-ligands have a higher emission at basic pH, instead lower at acidic pH. This switch process correlates to a pKa of pH 6.62, which is inside the pH range for biological applications (6.5-7.4). In acidic conditions, the rhodamine B stays in its stronger emission form. We control the coupling of the fluorophore to the plasmonic nanoparticle (and therefore the emission of the compound) with the molecular orientation with respect to the nanoparticle. The pH changes the RhB molecular conformation which in turn changes the orientation of the fluorescence dipole with respect to the nanoparticle, therefore changing the coupling.

This is reflected in the lifetime and quantum yield measurements. This reorientation results in a switched pH sensitivity (vertical dipole corresponds to low emitting molecular conformation but is enhanced by the nanoparticle, horizontal dipole corresponds to high emission molecular conformation but is strongly quenched by the particle). As soon as the pH increases, the molecule transits to a spirocyclic ring. This new state is non-emitting. This process of high and low fluorescence can be used as pH sensor. We present an AuNP-Rhodamine B conjugate having both Raman enhancement and a pH changing fluorescence. The plasmonic resonance of the gold particles is peaked around the wavelength of 521 nm the second component of dual probe is the rhodamine thiol derivative, which was synthesised in a two-step method [97].

The optical properties, such as emission and lifetime, were investigated at various pH. It was found that the emission intensity of 3 increased in more acidic conditions. As the pH goes down the Spirolactam ring opens, yielding to a greater fluorescence, as observed in other rhodamine

conjugates [105]. Making it more positive. Additionally, the emission maximum of AuNP.3 was shifted to a wavelength of 570 nm in comparison to 582 nm for 3. The lifetime of 3 shows two distinct components, representing two different decay rates. At low pH (3.82), and higher quantum yield, there is a slow component with a lifetime of 2.44 ns having a weighting of 63%, with the remaining 37% corresponding to the fast component of 0.58 ns.

As the pH is increased (6.26) and the quantum yield decreases, the lactam ring is formed, and the weighting of each channel is reversed as 31% now corresponds to a fluorescence lifetime of 2.37 ns and 69% to a lifetime of 0.34 ns. This change in lifetime along with the evolution of the quantum yield with pH clearly illustrates the increase of a non-radiative decay channel with protonation of the ligand. The lifetime of 3 was also measured in a series of solvents including ethanol where it was found that 93% of the fluorescence corresponds to a lifetime of 1.34 ns with the remaining corresponding to a lifetime of 2.13 ns, which agrees to reported values for rhodamine B.

The observed change of the fluorescence lifetimes with the solvent, indicates solvent quenching effects on 3, particularly in water Figure 35. Due to the emission shift of AuNP.3, and in order to quantify the coupling to the plasmonic resonance, the lifetime of AuNP.3 was measured at emission wavelengths 530 nm (corresponding to a full overlap with the LSPR of the AuNP) and 575 nm (corresponding to the tail of the LSPR). Both at low and high pH, the lifetime is reduced from ~600 ps away from the plasmonic resonance (575 nm) to below 100 ps (limited by the instrument response) on the plasmonic resonance (530 nm). Along with the decrease in emission intensity, the reduced lifetime of AuNP.3 around the plasmonic resonance Figure 35 shows that the fluorescence is being increasingly quenched by the AuNP as the spectral overlap with the plasmonic resonance increases. This is also consistent with the evolution of the emission spectrum of AuNP.3, as the intensity at a wavelength of 530 nm decreases faster with pH compared to a wavelength of 575 nm. Additionally, the weight of the fast component (sub-100 ps) is reduced as the pH is increased, in agreement with the reversed pH curve of AuNP.3

| | | 530 nm | | 575nmn | |
|---|---|---|---|---|---|
| pH 4.31 | Lifetime(ps) | <100 | 1700 | 611 | 2200 |
| | Weight | 92% | 8% | 31% | 69% |
| pH 8.16 | Lifetime(ps) | <100 | 1400 | 657 | 2800 |
| | Weight | 85% | 15% | 42% | 58% |

Figure 35 lifetime recorded at two different pH at two different wavelengths. Courtesy of [97].

Here we briefly described a dual-modal SERS/fluorescence imaging agent that is pH sensitive. The fluorescence changes with a large shift in the emission spectrum, from 582 nm to 570 nm upon surface functionalization to AuNPs of 12 nm in diameter. The second advantage that arises from functionalization to the AuNP is an inverse in pH dependent emission, with high emission observed at basic pH and low signal intensity at acidic pH with a pKa of 6.62. The complete work can be found [97].

## 4.3 FRET MODIFICATION USING SILVER NANO-GAPS

This work was carried out in collaboration with my colleague Dr. Abdullah O'Hamza. The main study of his work was to investigate the relation between Foster Resonant Energy Transfer FRET rate and the LDOS. The complete reference can be found here [87]. In terms of techniques used in this work, FLIM and hyperspectral imaging gave the contribution to gather the data for this work. The purpose of this work was to study the (FRET) process mediated by a silver nanocavity, In Figure 36(a) a representation of the studied system. The nanocavity is made by a 100nm thick silver film evaporated on glass with on top a 10nm dielectric spacing layer containing the donor. Two dielectric spacers separate the active layer from the silver film and the silver nanoparticle.

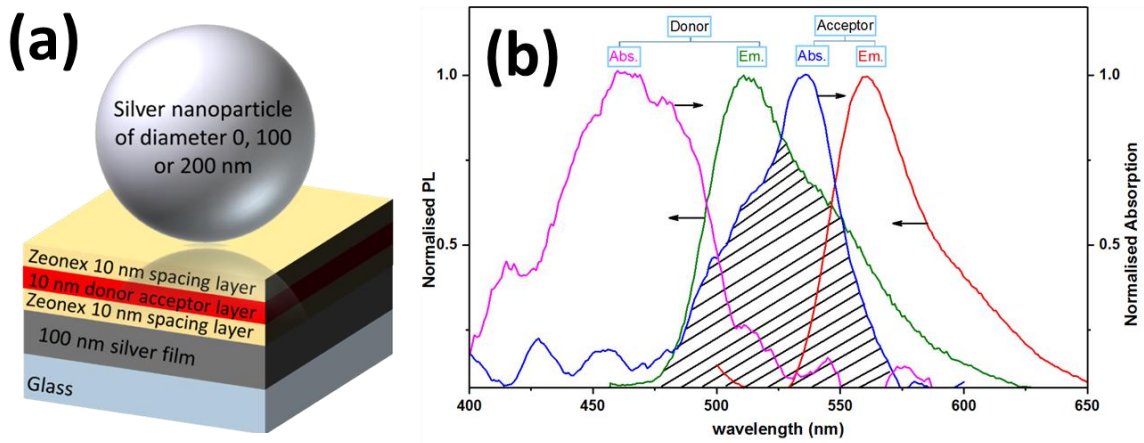


Figure 36(a) Schematic representation of the most performant plasmonic nanogap used to mediate the FRET. (b) Emission and absorption spectra of Uranin and Rhodamine6G. Donor and Acceptor respectively. Courtesy of [87].

The fluorophores couple used for this study is Uranin as donor and Rhodamine 6G as acceptor. The plasmonic nanocavity introduces a high local density of states not available to the dyes on their own, thereby introducing other channels for the FRET to take place. A steady-state fluorescence spectral mapping was carried out to study the modification of emission intensity at both the donor and acceptor wavelengths. Particles of 100 nm and 200nm diameter have been used to create the nano gaps. Each nanoparticle of interest was characterised by mean of a 10µm x 10µm (30 x 30 points square grid), these values are chosen in such a way that the pixels resolution are diffraction limited. Each point of the map is mapped over the spectral range 462 nm to 628 nm Figure 37. This map has been used to obtain all the spectroscopic parameters such as emission spectra and photoluminescence. The 405 nm laser power was kept around 3µW at objective. Measuring the power at the objective with a power and knowing the spot size it is possible to calculate the power density. This value is crucial to avoid photobleaching. The optimal power is chosen after a photobleaching study, namely several spectra are acquired at the same power without observing a change in the signal intensity.

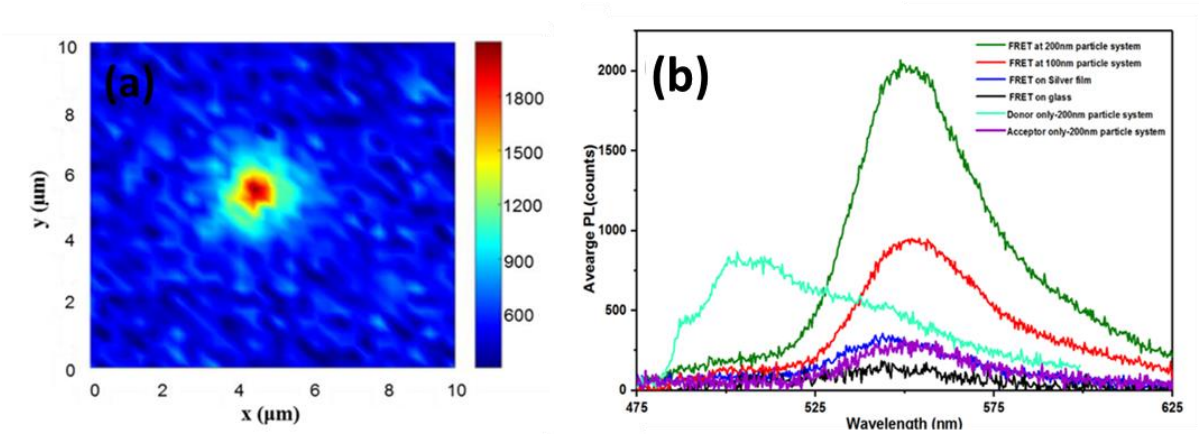


Figure 37 (a) 10 µm x10 µm area scan of fluorophores mix (Uranin donor and Rhodamine G acceptor) inside a 30 nm gap formed between a 200 nm silver particle and 100 nm thick silver substrate (Red spot), this maps composed by 900 pixels. (b) A fluorescence spectrum measured from a sample with the FRET pair, donor only and acceptor only in different conditions. (5% Uranin as a donor and 0.25% R6G as acceptor). Courtesy of 88.

We found an average emission increase of the acceptor equal to 15 times when the donor-acceptor couple is in the gap formed between the silver film and 200 nm silver. With the 100nm diameter silver particle, this enhancement is roughly 6 times in average. This is a good evidence of the FRET being improved by the nano gap. We proved that the observed enhancement is due to FRET rather than Purcell enhancement. This is done with the acceptor emission intensity $\frac{I_A}{I_{Ao}}$ calculated both in presence and absence of the donor.

### 4.3.1 DONOR LIFETIME MODIFICATION

To further prove the occurrence of FRET in the plasmonic nanocavity samples, it is very useful to study the donor fluorescence lifetime modification. The samples scanned to measure the photoluminescence enhancement have been re-scanned with the FLIM to obtain the lifetime change, such as Figure 37(b). We investigated the lifetime of the donor both on its own and in presence of the acceptor. This was to build a reference so we could be able to distinguish the modification performed by the nanostructure. Three different conditions have been investigated: donor alone, FRET pair on a substrate and the FRET pair into a plasmonic nano gaps. Two different silver nano particles have been used to complete the plasmonic nanocavity: 100 nm and 200nm diameter. Two components are found, the faster one was 2.9 ns and a slower one at 5.5nm. The fast component of the donor lifetime changed to 1.4 ns when measured from a silver film Figure 38. When probed into the nanogap, the fast components of the lifetime changed to 1.1ns and 0.82ns for the 100nm and 200nm particle, respectively. The FRET rate is calculated from the relation $\Gamma_{DA} = \Gamma_{total} - \Gamma_D$. With emission decay rate is the

inverse of the lifetime $\Gamma_D = 1/\tau_D$ as seen in chapter one. A decrease of the lifetime therefore means an increase of the decay rate, which is proportional to a modification of the local density of states. We observed a change in the donor decay rate once placed in the different photonic environment. We see a 2-fold increase when using a silver substrate, 2.5 and 3.5 when using a nanocavity with 100nm and 200nm nanoparticle respectively to form a nanogap.

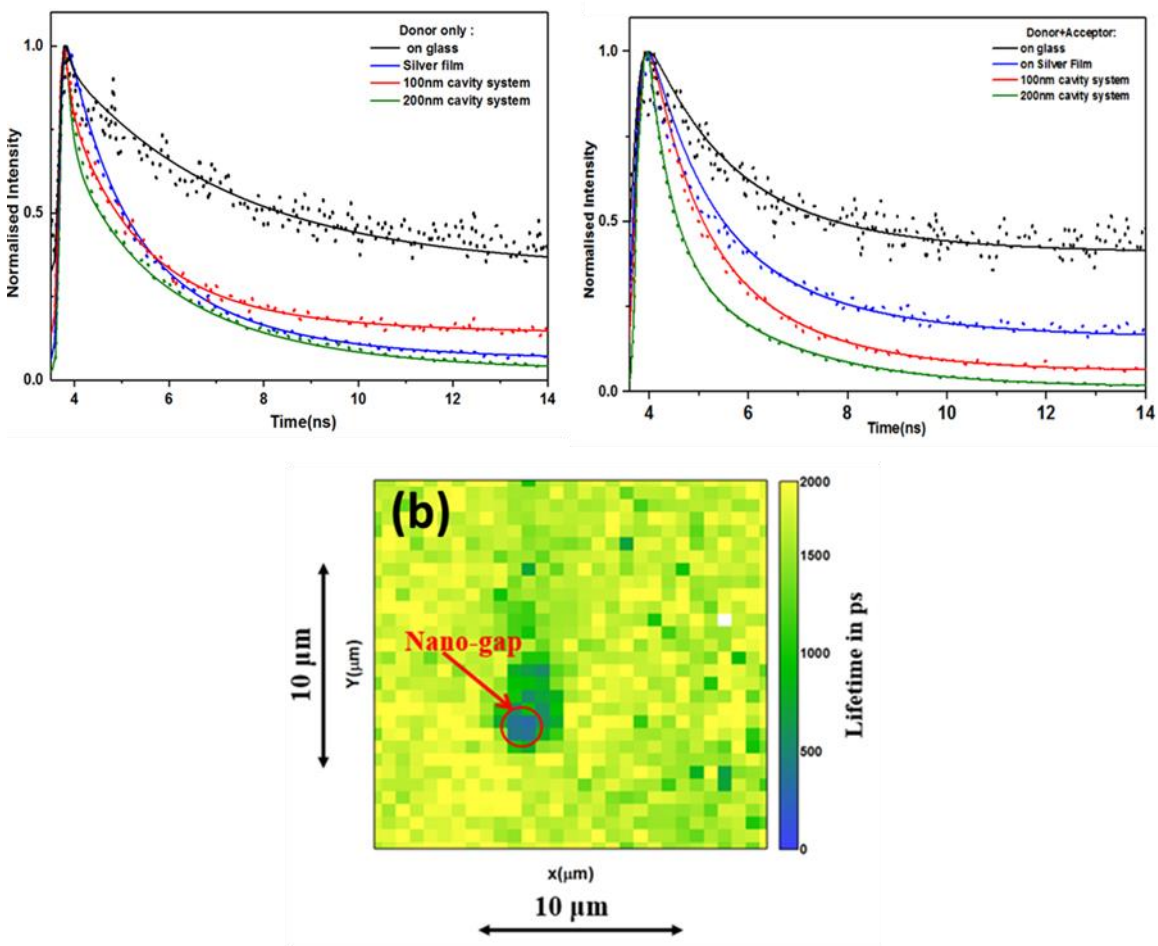


Figure 38 (a) Lifetime curves for the donor alone (Uranin) under different conditions, glass substrate, on silver film , in 100nm and 200nm nano gap .(b) Fluorescence lifetime image obtained on a similar nano gap. (c) Lifetime curves from the FRET pair (Uranin as a donor + R6G as acceptor) (b) Donor decay rate in the absent and presence of the acceptor. Courtesy of [87].

The FRET efficiency was calculated using the equation [106], [107]:

$$\eta_{FRET} = \frac{\Gamma_{DA}}{\Gamma_{DA} + \Gamma_D} = \frac{\frac{\Gamma_{DA}}{\Gamma_D}}{1 + \frac{\Gamma_{DA}}{\Gamma_D}} \tag{56}$$

We studied the FRET process in Uranin-Rhodamine 6G pair once the system was characterised on its own. We found that the enhancement in the energy transfer rate is highly sensitive to the

coupling between the two metals. The relationship between Förster energy transfer rate and LDOS was linear for gap widths larger than 10 nm and sublinear for gap widths less than 10 nm.

## 4.4 $SiN_x$ NANO STICKS

These samples were fabricated and provided by Dr. Chinna Devarapu from CAPPA (Centre for Advanced Photonics and Process Analysis) at the Cork Institute for technology in Ireland. The focus was to use silicon nitride micro gratings to generate micro laser, however, in a first instance we characterised their optical properties using the silicon nitride fluorescence. We can see what the sample looks like from Figure 39 (a). The first step was to use the K-space white light reflection to characterise the structure modes in reflection Figure 39 (b). We can see several modes localised across the range 450 nm 850nm, therefore offering a good platform for lasing applications.

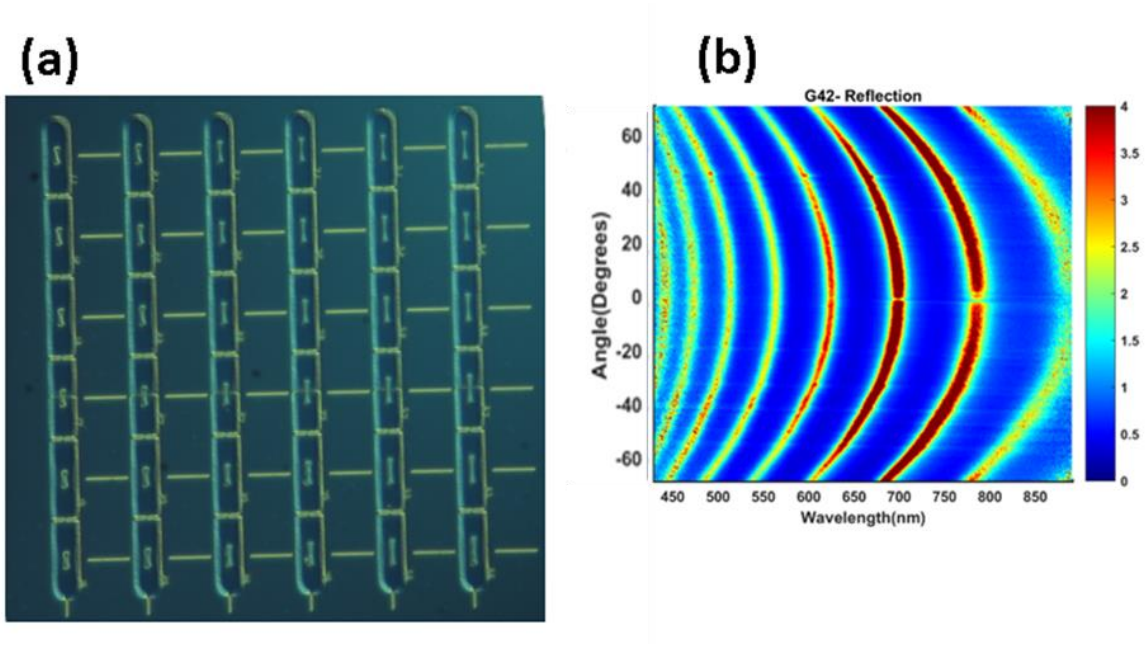


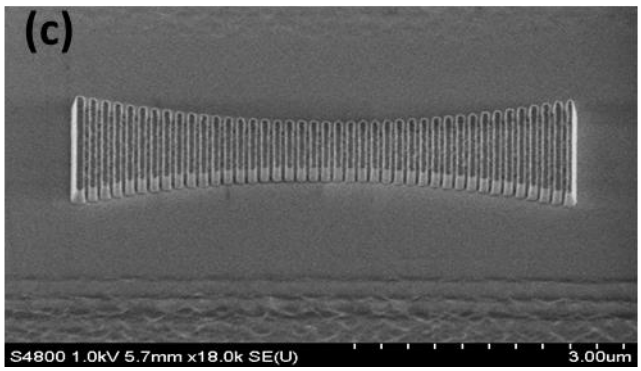


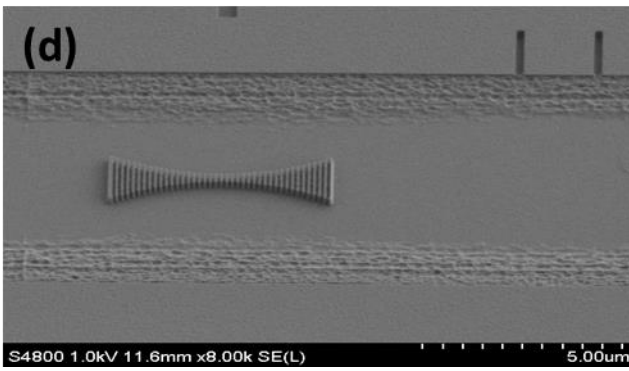

Figure 39 (a) Bright field images of an array of nanosticks. (b) k-space reflection map of a nano-grating. (c) SEM image of micrograting at high magnification and (d) low magnification.

The second step was to use the $SiN_x$ autofluorescence to obtain some modal images. Once the laser optimal power (2.9 µW 405 nm CW) was found, we used the hyperspectral imaging capability of the microscope described in chapter 3 to obtain the images in Figure 40 wavelength used for the display is 627nm. Figure 40 (a) shows a 10x10 $\mu m^2$ scan obtained with unpolarised light, namely the emitted light was not analysed.(c) and (d) represent the same image, but by selecting the emission polarisation with a polariser in front of the spectrometer: for a polarization parallel to the main axis of the grating and orthogonal respectively. The image corresponding to the polarization orthogonal to the grating main axis is quite well resolved, we can see the hotspot at the centre of the structure.

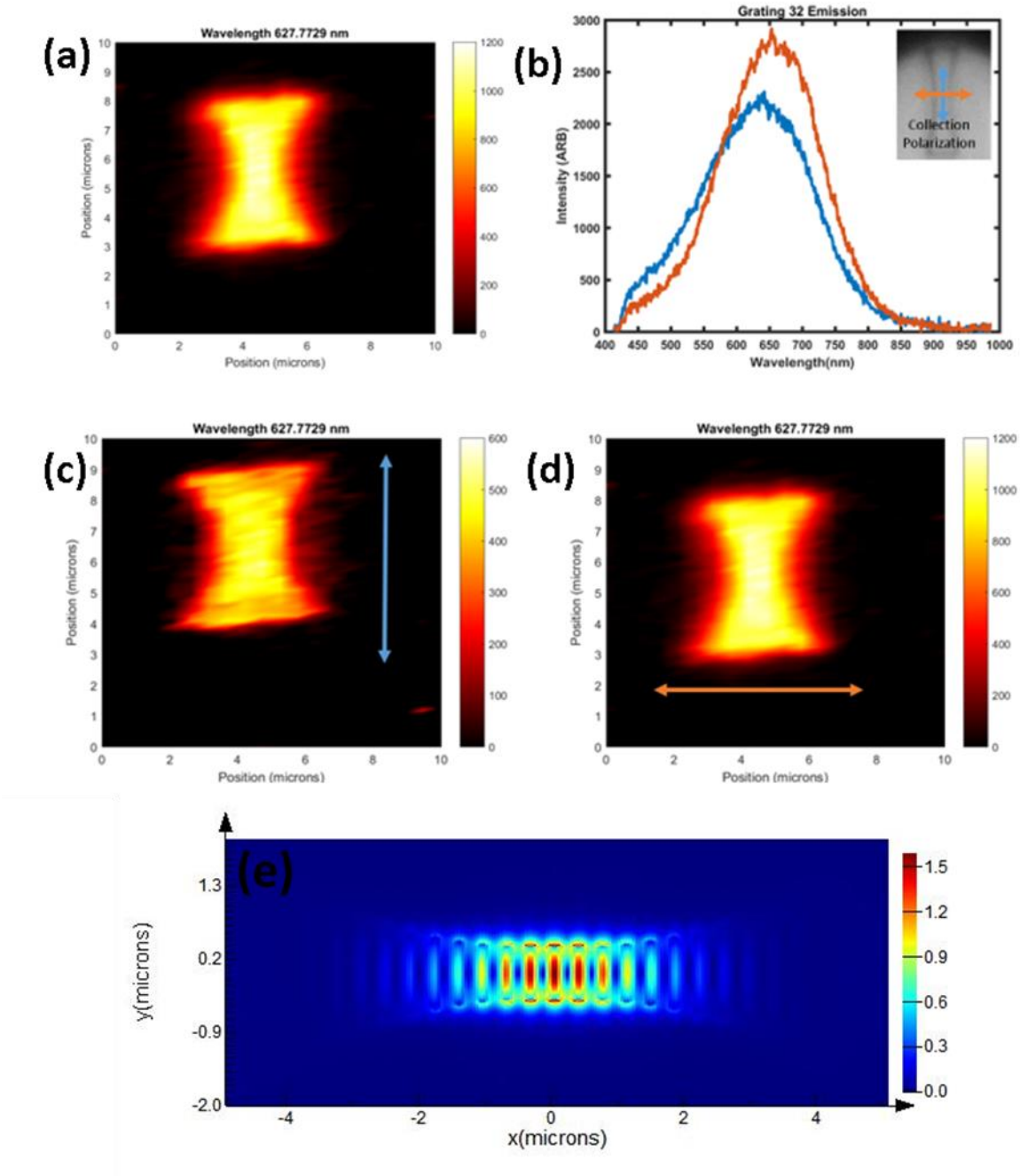


Figure 40 (a) hyperspectral image reconstructed by mapping the grating at the wavelength of 627nm. (b) intensity emission plot for two different polarization. (c) Auto fluorescence emitted from a $SiN_x$ with exciting polarization parallel to the main axis of the grating orange, (d)Polarization orthogonal to the main axis. (e) Simulated typical electric field ma inside a micro grating. Simulation courtesy of CAPPA.

These images were obtained without real plane filtering (confocal), namely the hotspot at the centre of the structure appears much bigger than the laser spot. By introducing a 100 µm diameter pinhole in the real plane at the exit of the microscope, we reduced the collection area of the signal by $1/10^{th}$. The image was re-acquired filtering the polarization orthogonal respect

to the grating main axis Figure 40 (d).This reconstructed hyper image resolved lots of details that were uncovered without spatial filtering. We can see several minima and maxima across the structure. This image allowed us to obtain some spectroscopic information as well. We plotted together several spectra obtained from different positions across the micro grating Figure 40 (b). The emission from the $SiN_x$ background is peaked around 650nm, instead the grating one is slightly red shifted. On the grating spectra a second peak appears around 700nm, At the edge of the grating the secondary peak appears in the spectrum as a shoulder, going toward the centre of the microstructure, the intensity of this second peak increases. At the exact centre of the micro grating the 700nm shoulder appears as a peak and its intensity it is comparable to the main peak at 650nm.

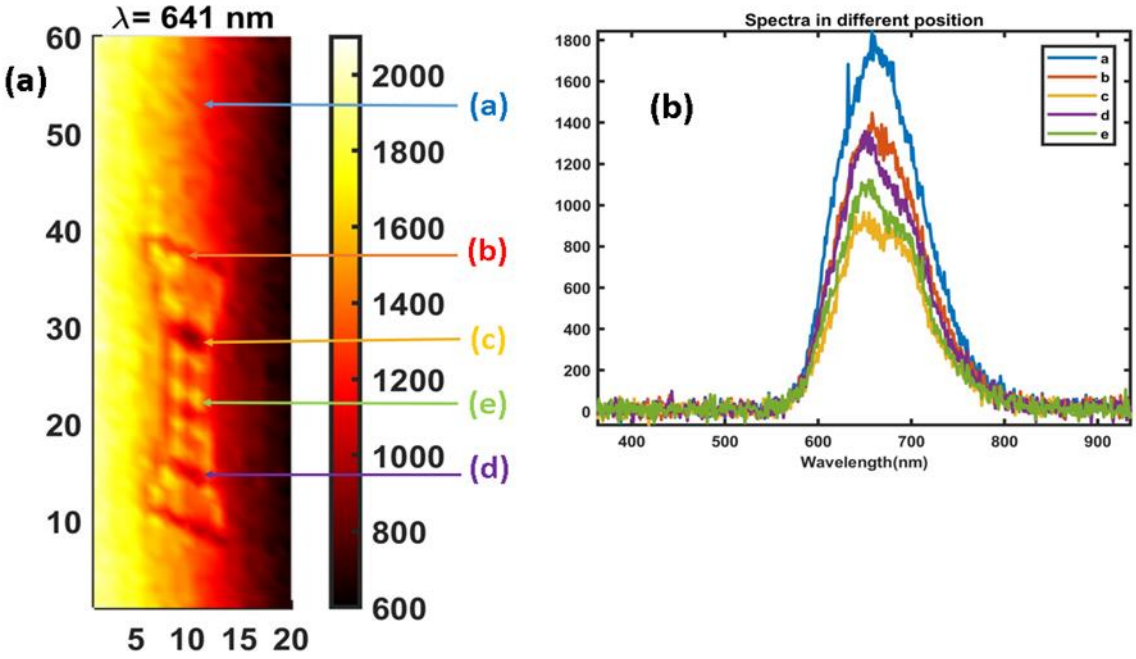


Figure 41 (a) High resolution hyperspectral image obtained with a 100µm pinhole. (b) emission spectra taken at different position across the grating.

In this paragraph we have briefly seen some basic properties of the $SiN_x$ micro gratings. We have seen how hyperspectral imaging can reveal some resonant modes inside the structure. A future study for this system is couple an emitting polymer or a gain medium to get localised lasing from the hotspot of the nanograting.

## 4.5 CONCLUSION

In this chapter, all the works in which this thesis gave a collaboration, or a partial contribution have been presented. In the first part of the chapter, the synthesis, and the optical properties of an innovative type of InP/ZnS quantum dots with ultra-high quantum yield have been described. . We continued with an innovative dual fluorescence and Raman nano probe. This system is a

12nm diameter nano particle with few thousand emitting molecules attached with it. We have seen how the emission is pH dependant and how the quantum yield is optimal in the biological range making this probe a realistic possibility for bio imaging. The third topic touched is the Foster Resonant Energy Transfer modification induced inside a silver nano particle on mirror cavity. We have seen how a 200nm in diameter silver nano particle onto the silver film was found to be the most optimal geometry to increase the FRET rate of the couple Uranin-Rhodamine 6G. The FRET rate was increased almost by a factor 3 instead the FRET efficiency was enhanced by the 42%. The last topic discussed in the chapter are the SiNx nano sticks, namely a focusing nano grating made by nanometric sticks. The purpose of this work was to get nano lasing, but this purpose was not achieved for time reasons. The nano sticks, however, gave few excellent hyper spectral images. Before concluding this chapter, I would like to express a big thank you to Dr. Clarke, Dr. Eling and Dr. O'Hamza respectively; it was a great pleasure and an honour to help at getting good measurements for your thesis and your publications.

# Chapter 5 HYBRID NANOCAVITIES

In the past few years, the nanoparticle on a mirror (NPOM) geometry has attracted a large amount of attention due to the ease and simplicity of fabrication. The coupling between the plasmonic modes of the nanoparticle with the plasmonic metal film provides strongly enhanced and highly localised electric fields other than a high density of photonic states. NPOM are easy to manufacture since in the most basic form they do not require any nano or micro patterning technique. They comprise of a homogenous metallic film with drop casted nanoparticles on it. A more sophisticated version can be manufactured via laser ablation [108] or thermal annealing [109]. The most popular materials are the standard plasmonic metals, gold, and silver. Purely metallic nanogaps generally suffer from drawbacks such as lower-quality factor than dielectric resonators [110]. On the positive side they exhibit a strong electric field localization and small modal volume. Another effect of the purely metallic nanocavity is the characteristic optical losses typical of metals. This is a problem for applications that require to enhance the spontaneous emission, but it is an advantage for applications such as Surface Enhanced Raman spectroscopy [111], [112], [113].

Our group has shown the use of such NPOM nanogaps for various applications such as single molecule Surface Enhanced Raman scattering [112], spontaneous fluorescence emission enhancement [57] and Forster Resonant energy Transfer control [87]. These systems are purely metallic nanogaps made by an extended metallic film and a nanoparticle separated by a 5-40 nm thin dielectric layer. Different approaches have been taken to reduce the intrinsic losses due to the metal film. A simple and effective system is to place a dielectric spacing layer between the gold film and the emitter doped film [87] to reduce the strong quenching due to the metals. This kind of nanogaps geometry allows to obtain enhancement in the order of hundreds of times by using an emitting layer just 10 nm thick [57].

The emission performances of a nanocavity are directly linked to the Purcell factor, which depends on the ratio of the quality factor to the mode volume as stated in Eq.41 There are therefore two ways to increasing the Purcell factor: one is to reduce the mode volume, the second is to increase the quality factor. There are several examples of high Purcell factor NPOM systems in the literature. Some groups used long silver nanowires on a silver mirror [114] and achieved 1000 times total spontaneous emission enhancement with a modified quantum efficiency of 0.25. Another strategy used is to embed the nanoparticle inside a dielectric nano fibre, in this way it is possible to achieve a coupling over a larger area rather than just one

hotspot [115]. Other groups [116] used another approach in which the mirror is made by a 1-micron diameter disk rather than an infinite film obtaining a small modal volume with a Quantum efficiency of 0.5. The reduction of the modal volume has been used by [117] as well: they realised a metal-insulator-metal resonator using an isolated disk both as mirror and as particle.

All the approaches mentioned above worked on reducing the volume mode by using the plasmonic nanoparticle. Dielectric resonators, on the other hand, offer very high-Quality factor, however this is observed over a small spectral bandwidth, typically 0.1 nm to 0.01nm [118],[119]. By contrast, the emission line width for a single quantum dots is typically 15 nm [120], at room temperature. Consequently, for a large band emitter the coupling tends to be weak in a purely dielectric resonator and it depends on the capability of the resonator to support the emission with the smallest mode volume possible. In theory the smallest mode volume possible is the diffraction limit:

$$V = \left(\frac{\lambda}{2n}\right)^3 \tag{57}$$

Where $\lambda$ is the wavelength and n the material refractive index. On the other hand, the plasmonic effects are happening at subwavelength scale, therefore the concept of diffraction limit is overcome. There is evidence of mode volumes as small as $0.03\left(\frac{\lambda}{2n}\right)^3$ [114]. Therefore, an advantage for using plasmonic entities instead of dielectric resonators is the bandwidth over which we can get enhancement.

In this work we aim to merge the two approaches with a hybrid configuration plasmonic-dielectric. We built new plasmonic nano gaps in which the metallic layer is replaced with a dielectric Distributed Bragg Reflector (DBR) Figure 40. In this way we will try to use both the small mode volume of the plasmonic and the high Q factor of the dielectric reflector. We are going to study two different physical regimes, in the first one we are going to couple the reflection band of the DBR with the plasmonics entity to make a hybrid nano particle on mirror cavity. Whereas in the next chapter we explore the interaction of the plasmonics nanoparticle with the first Bragg mode, namely in a confined situation. In this chapter we are going to investigate the coupling of the DBR reflection band with a gold nano sphere. We are going to study both the emission pattern and the modification of the LDOS.

## 5.1 PHOTONIC BAND COUPLING

In this work a metallic mirror is going to be replaced with a Distributed Bragg Reflector (DBR), a schematic structure in Figure 42. The system behaviour into the high reflectivity region of the photonic bandgap is going to be investigated. Both dipole orientations, vertical and in plane, are studied. This change for the mirror is motivated by multiple reasons, since a DBR is a dielectric stack, as we have seen in chapter one, the intrinsic losses are potentially greatly reduced. A DBR has an almost perfect reflection into a spectral region called stop band. In this area of the spectrum the light cannot propagate inside the stack making the DBR work like a reflector.

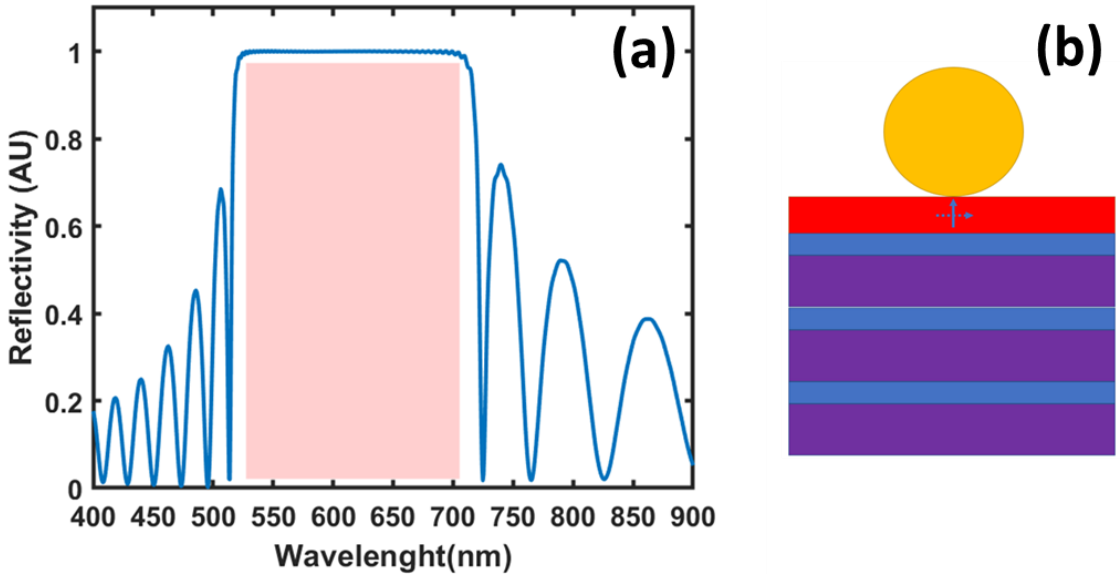


Figure 42 Representation of the hybrid nanocavity. The gold sphere placed above the active layer (red). The blue and the purple layer are the low and high index respectively of the DBR. The arrows represent the dipoles orientations. We studied one orientation at time. We studied the physical regime inside the DBR reflection band.

### 5.1.1 FDTD CALCULATIONS DECAY RATES

Due to the complexity of the system we started from the FDTD calculation to model the properties of a dipole emitter in such hybrid nano cavities. These simulations were carried out in the ideal conditions, namely one single isolated dipole placed at the centre of the nano cavity between the particle and the DBR surface. We obtained the emission diagrams via near to far field projections. The study has been carried out for two dipole orientations parallel and orthogonal to the substrate surface. The calculations have been repeated with four particle diameters (100, 250, 400 and 500) nm. The emitting layer has been modelled as a dielectric with a refractive index of 1.45 and a thickness of 10 nm. The emitting dipole is placed at the exact centre of the nano cavity in between the DBR surface and the particle bottom.

#### 5.1.1.1 METALLIC LAYER – DBR CAVITY COMPARISON

Before we start analysing the radiative properties of these nanocavities, it is worth seeing what the electric field looks like. In this way we can derive in which direction is the cavity moment and therefore optimise the dipole orientation. In Figure 43, we have the comparison of the electric field x and z components, recorded at the resonance for a 500 nm nano particle hybrid nano cavity. The nano cavity is only 10 nm thick and, although care was taken to remove the dipole source component from the field map, the recording of the electric field is partially affected by the injected dipole. However, removing the singularity at the centre, we can see how the strongest electric field component is the z one when the dipole is vertically oriented Figure 43(c). We can apply the Fermi's golden rule to postulate that decay rate is going to be the largest when the dipole is vertical (parallel to the cavity moment) and the smallest when it is horizontal (dipole oriented perpendicular to the cavity dipole moment).

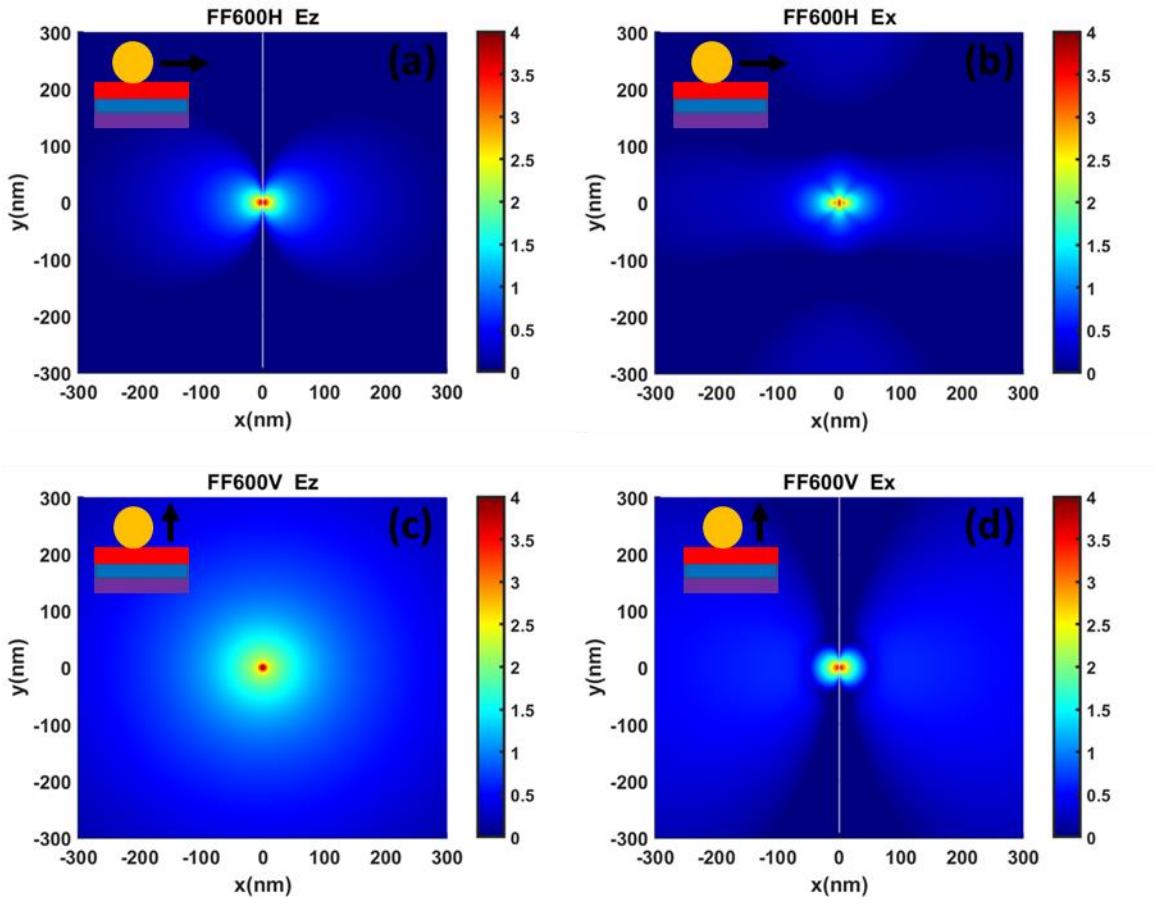


Figure 43 Electric field components maps measured for a 500 nm nano sphere-based hybrid nano cavity respectively horizontal dipole (a) z component, (b) x component. Vertical Dipole (c) z component, (d) x component. Intensity units in log scale. Image taken at 578 nm.

We carried on the study by comparing the decay rates of purely gold nano cavities and a DBR with a central reflection wavelength at 600 nm. The other parameters such as active layer, dipole orientation have been kept constant. Let us begin with purely metallic nanocavities. In Figure 44 (a-b) we have the normalised decay rate curves obtained for purely metallic

nanocavities with vertical and horizontal dipole respectively. The vertical orientation is the one that couples to the nano cavity because of Fermi's golden rule, with a factor of 10 between the two orientations.

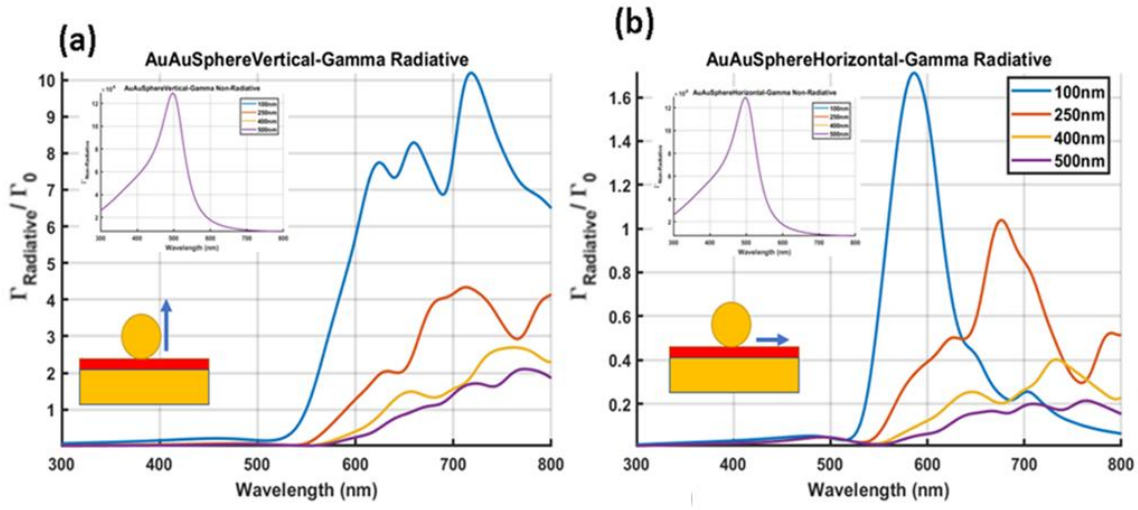


Figure 44 FDTD simulated Quantum efficiency for purely metallic nano cavities: (a) Simulated Radiative and (inset) Total decay across the visible spectrum. Maximum scale value for the inset 12000. Vertical Dipole (b) Normalized simulated Radiative and (inset) Total decay across the visible spectrum. Maximum scale value for the inset 12000. Horizontal Dipole.

In Figure 45(a) we have the calculated curves for the radiative decay rate over the vacuum decay rate for the vertical dipole inside the hybrid nanocavity for the vertical dipole. Enhancement is inversely proportional to the particle size, but as we can see the values are one order of magnitude higher than the gold case for the vertical orientation which is the one that realise the coupling. The horizontal dipole is weakly coupled the cavity, since the Fermi rule, for the hybrid nano cavity as well Figure 45(b). For this dipole orientation, the 100 nm particles give an enhancement as high as 2.5 instead the other particles are around 3. These values for the horizontal orientation are two orders of magnitude lower than the case with vertical dipole. Even for this nanocavity the electric field is mostly oriented toward z and the strongest field is experienced with the vertical orientation Figure 45 (c-d).

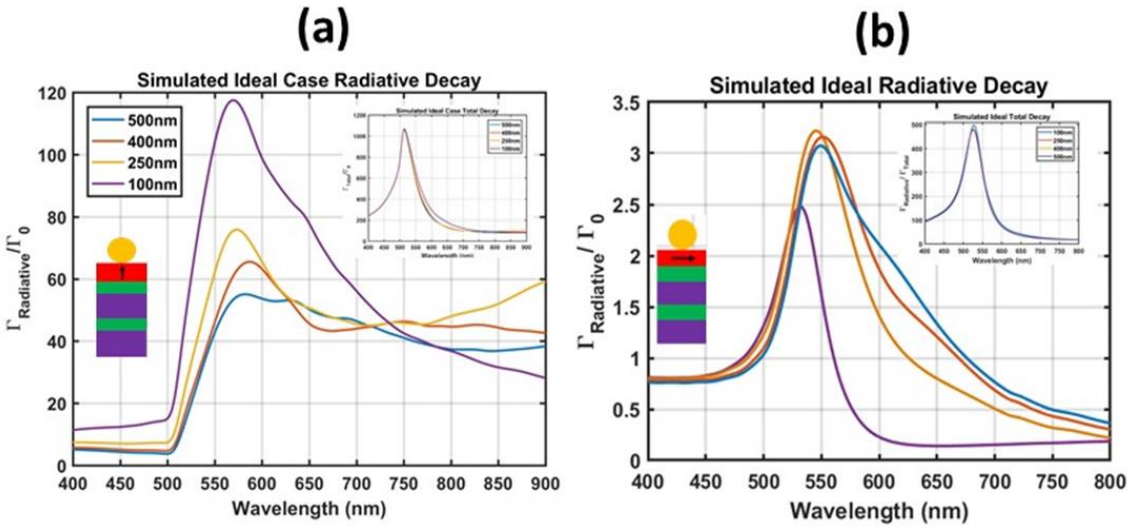


Figure 45 FDTD simulations: (a) Normalized simulated Radiative and (inset) Total decay across the visible spectrum. Maximum scale value for the inset 1200. Vertical Dipole (b) Normalized simulated Radiative and (inset

We summarised in Figure 46 all the radiative rates by integrating, over the visible range, all the curves for each particle size and dipole orientation other than for each substrate. The curves show clearly that the dielectric substrates have a much higher radiative decay rate enhancements compared to the gold one. The horizontal dipole orientation confirms the trend; however, the values are considerably smaller than the vertical one.

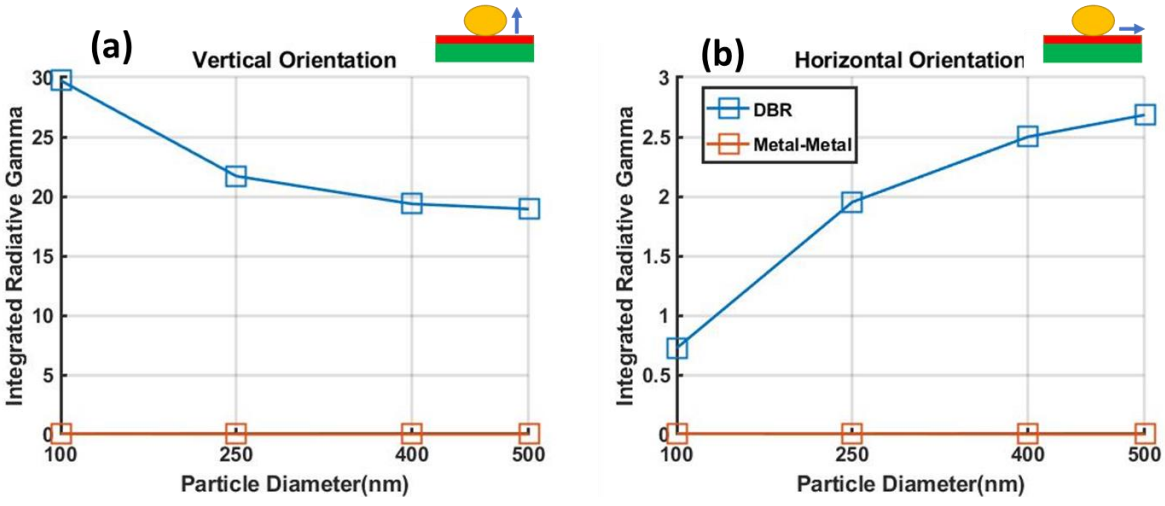


Figure 46 Summary for the FDTD measured radiative rates for all cavities. (a) Vertical Dipole, (b) horizontal orientation

#### 5.1.1.2 MODIFIED QUANTUM EFFICIENCY

It is also interesting to look at the modified quantum yield for the dipole emitter in the nanocavity. The quantum efficiency of a nano cavity can be expressed with the equation:

$$\phi_m = \frac{\Gamma_{rad}}{\Gamma_{total} + k_{nr}} \tag{58}$$

With $k_{nr}$ the intrinsic non radiative rate of the emitter in vacuum. We can connect the nano cavity quantum efficiency to the vacuum one with the equation [57]:

$$\phi_m = \frac{\frac{\Gamma_{rad}}{\Gamma_0}}{\frac{\Gamma_{total}}{\Gamma_0} + \left(\frac{1}{\varphi_0} - 1\right)} \tag{59}$$

Where $\varphi_0$ is the vacuum efficiency; We used the equation above to calculate the modified quantum efficiency for both hybrid nano cavities and purely metallic nano cavities as a function of $\varphi_0$ and the particle size. We used fixed values for $\varphi_0$ such as 1 (ideal case), 0.9, 0.6, 0.4, 0.2, 0.1 and 0.025. In Figure 47 we have the calculations performed for the hybrid nano cavities. We can see that all the curves follow a similar trend, they all start growing at the wavelength of 520 nm and reach a plateau around 600 nm. The maximum QE reached is 0.3 and always in the far-red part of the spectrum. Decreasing the quantum efficiency in free space $\phi_0$, we obtain a linear and according reduction of the quantum efficiency Figure 45.

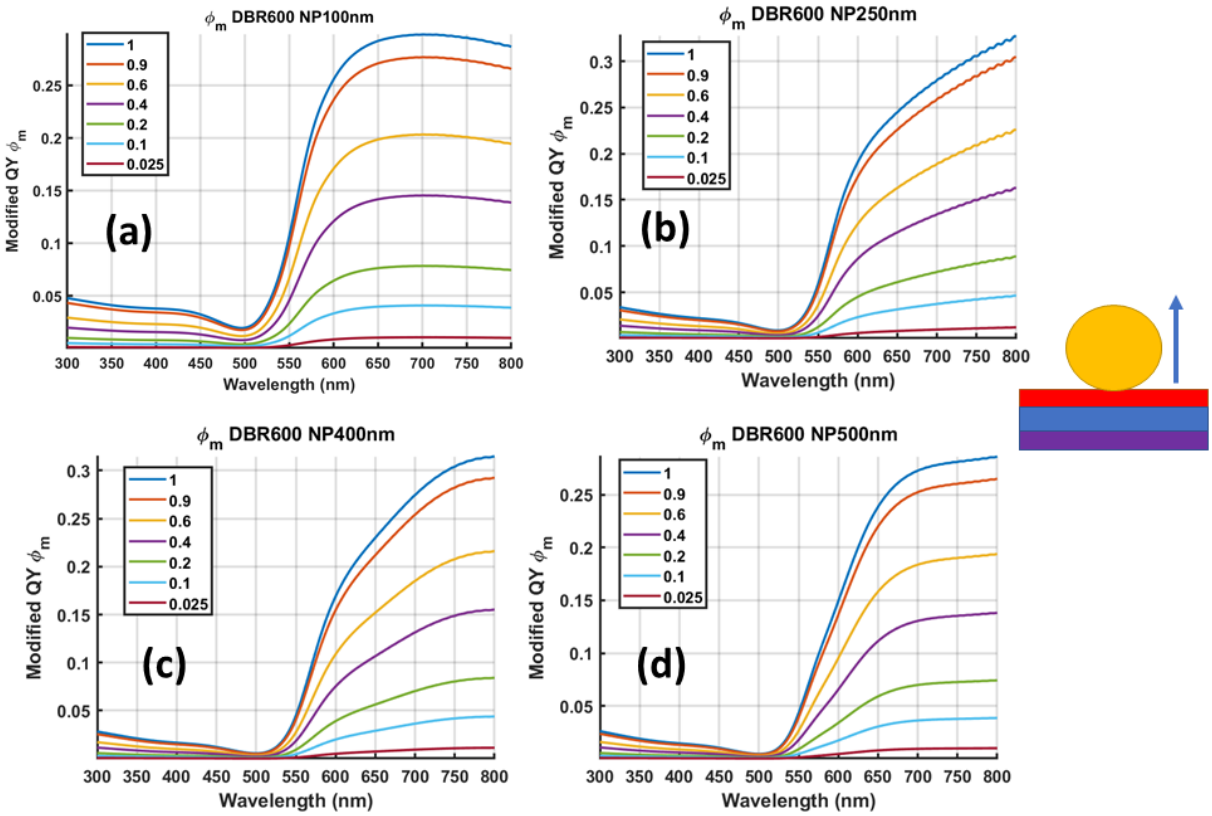


Figure 47 Modified quantum efficiency for a hybrid nano cavity with a vertical dipole calculated for a gold sphere with different diameters: (a) 100 nm, (b) 250 nm, (c) 400 nm, (d) 500 nm at different values of $\phi_0$.

We repeated the same calculations for the metallic nano cavities as well, Figure 48. The first difference with the hybrid case is the maximum value, the largest efficiency achieved here is in the order of $10^{-3}$. Almost 3 orders of magnitude less than the DBR case. Reducing $\phi_0$ we observe a reduction of $\phi_m$ accordingly, however the reduction is not linear for all the wavelengths. For instance, let us look at the Figure 48(b).

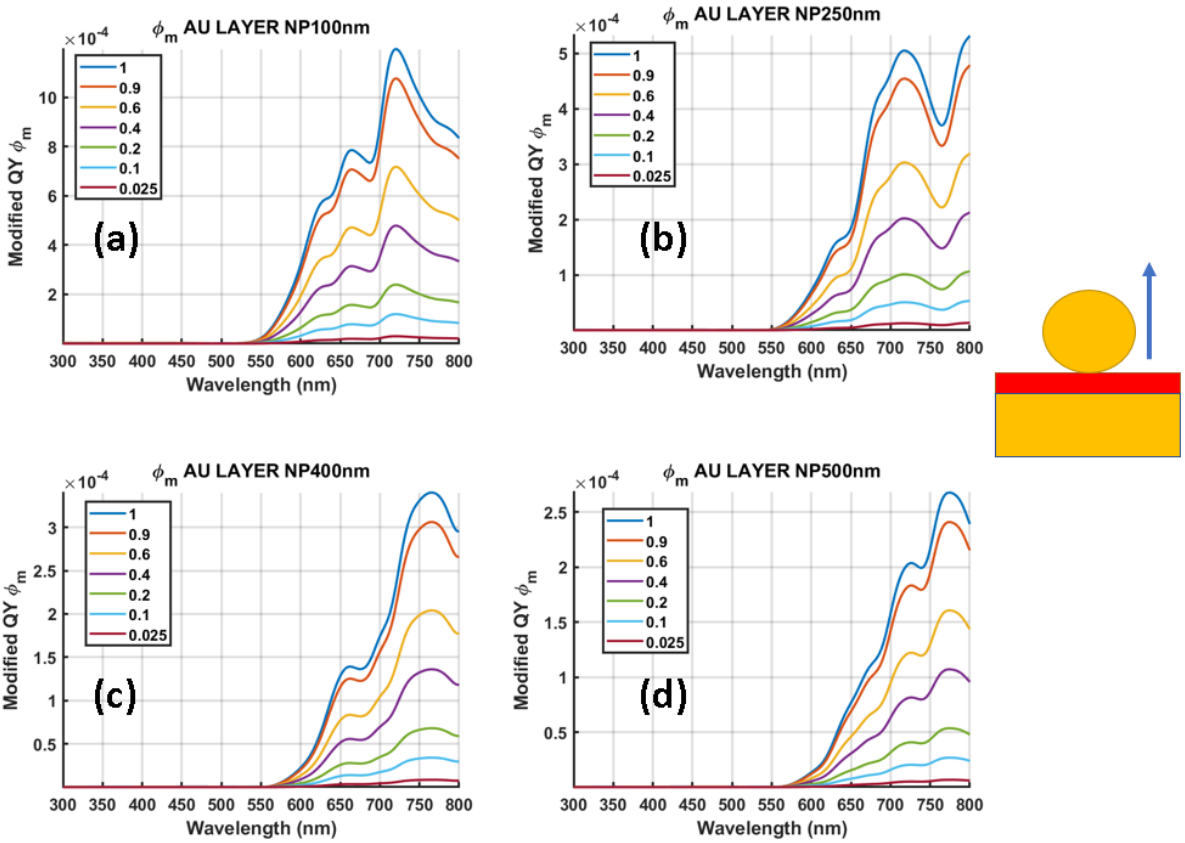


Figure 48 Modified quantum efficiency for a purely gold nano cavity with a vertical dipole calculated for a gold sphere with different diameters: (a) 100 nm, (b) 250 nm, (c) 400 nm, (d) 500 nm at different values of $\phi_0$.

The modified quantum efficiency curves cited afore are produced with a wide emission spectrum dipole. To represent the dyes used experimentally, we decided to correct the modified quantum efficiency with the emission spectrum of the two emitters used experimentally: Lumogen red and F8TBT.

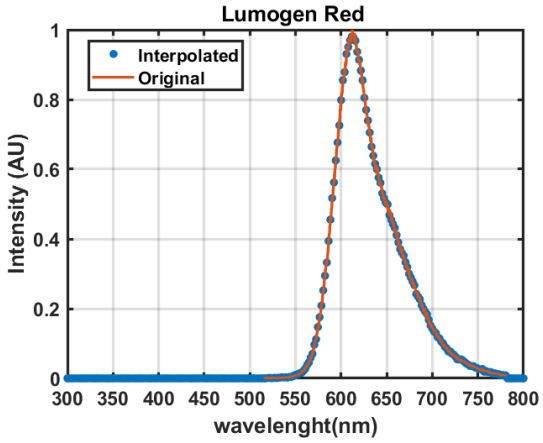


Figure 49 Lumogen emission spectrum. Orange original spectrum as collected from the spectrometer. Blue interpolated spectrum onto the FDTD calculations wavelength range.

This was done interpolating the experimental spectra over the calculation wavelength range and sampling, and normalising it to 1, Figure 49, see experimental section 5.2 . The final step is to perform a convolution of the modified QY curves with the interpolated spectrum. Figure 50 shows the results for the convolution performed on the DBR cavities curves. The new curves are reminiscent of the Lumogen red emission spectrum because, in the Lumogen red emission range (600 nm-670 nm), the original QY curves look like flat or slowly growing. Moreover, we observe a small change as a function of the particle size.

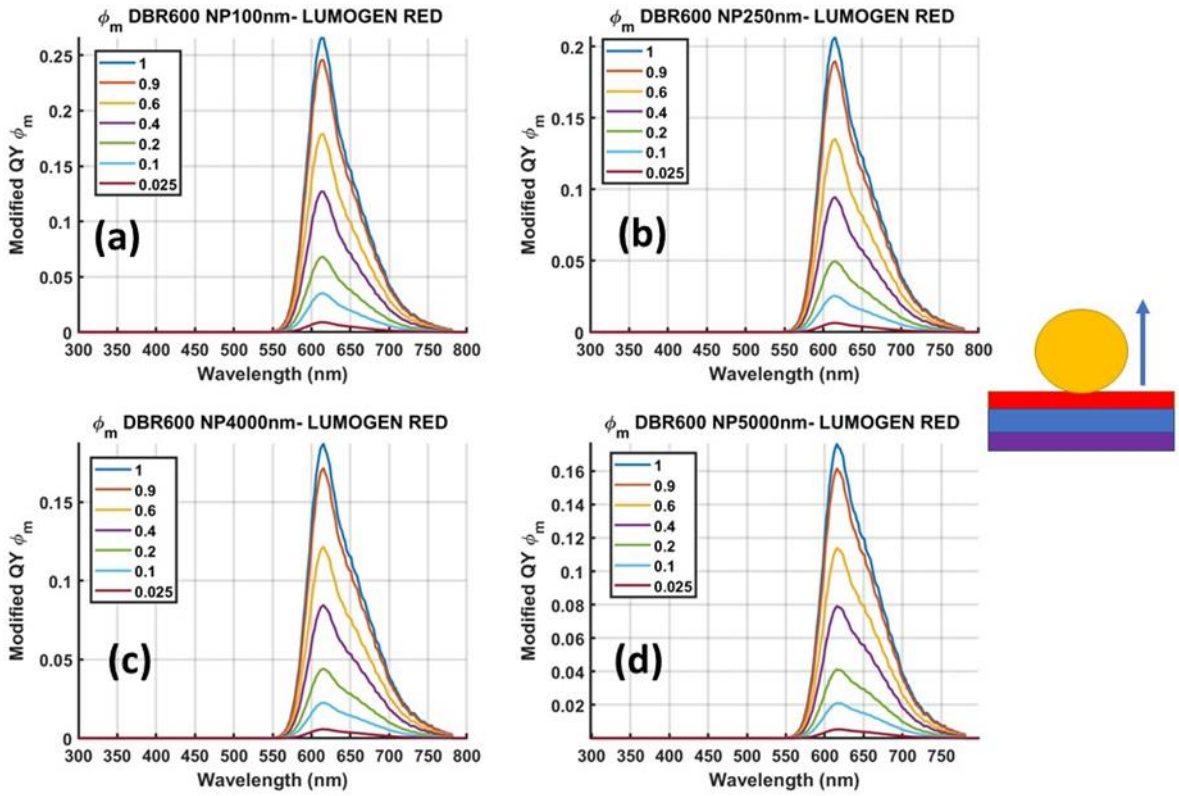


Figure 50 Modified quantum yield curves for the DBR hybrid nano cavities. Curves corrected for the Lumogen red emission spectrum

We repeated the same convolution process with the purely gold nano cavity curves Figure 51. We observe again a small quantum yield due to the gold quenching but decreasing in directly proportional to the particle size. The general shape observed in a flat source is retained over the dye emission spectrum

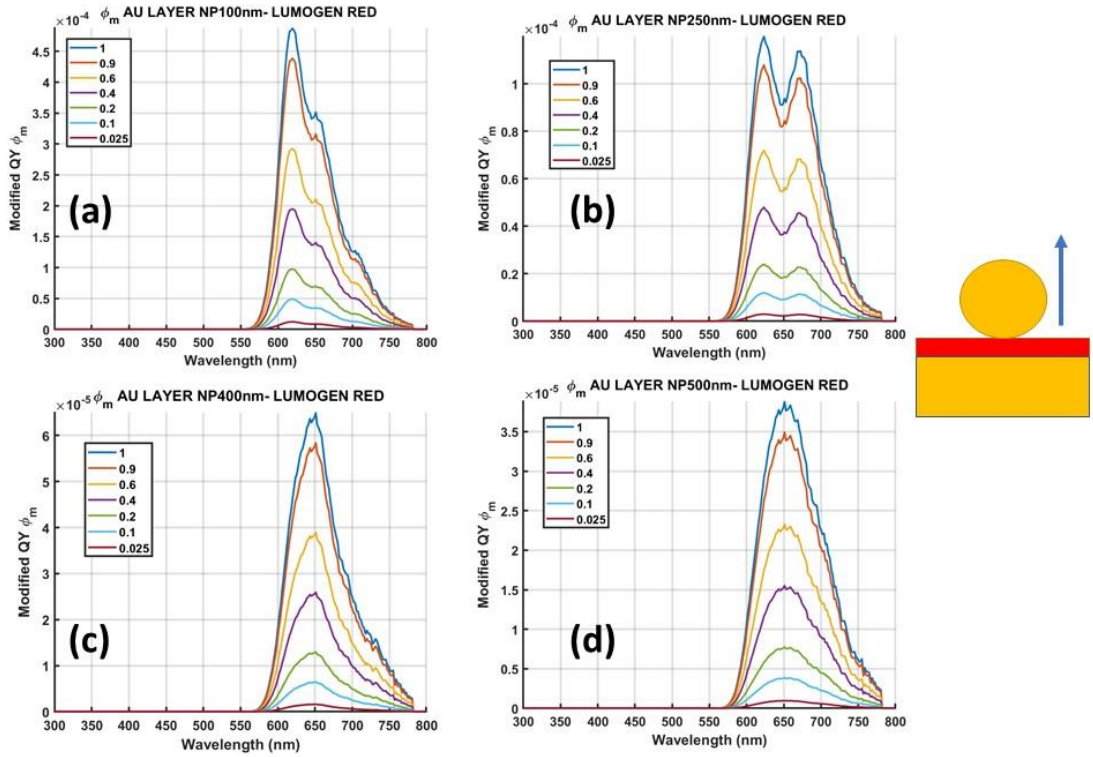


Figure 51 Modified quantum yield curves for the metallic nano cavities. Curves corrected for the Lumogen red emission spectrum.

We decided to apply this real emitter correction to the decay rates curves as well, to be able to directly correlate the experimental results with the simulations. We used the same procedure used for the modified QY curves, namely we interpolated the emission spectrum over the simulation spectral range, normalised it to one and then multiply it to all the curves. In Figure 52 we have the corrected decay rates, the vertical orientations Figure 52 (a) (c) DBR and metallic cavity respectively.

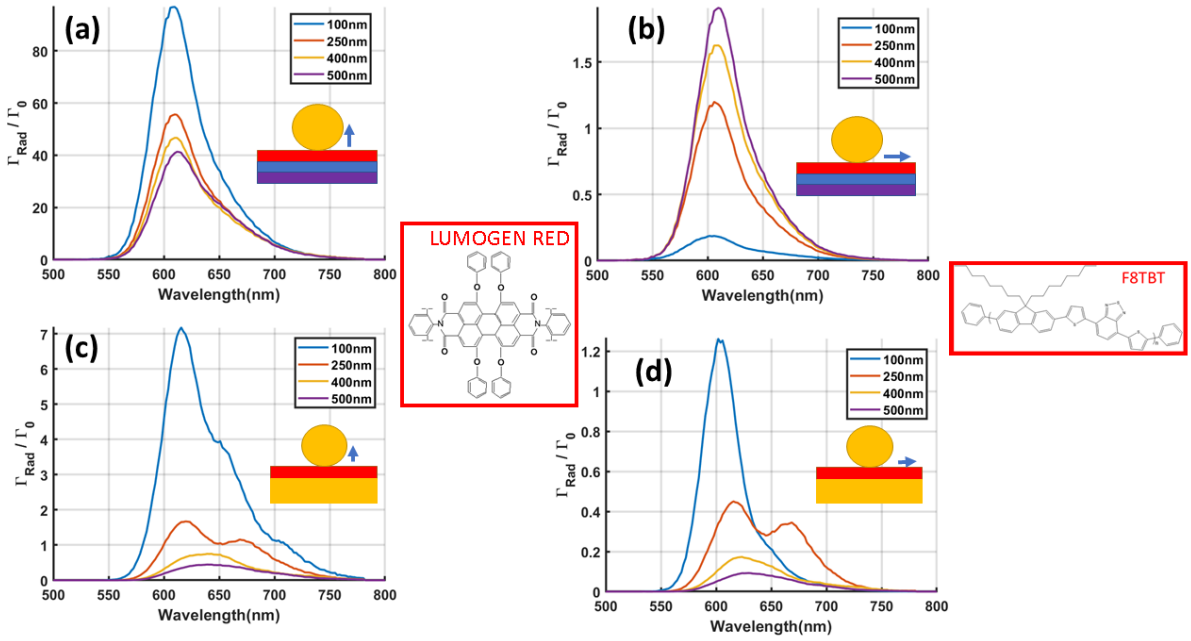


Figure 52 Corrected decay rates with the experimental emission spectra (a) DBR600, purely metallic nanocavity (c) Vertical dipole cavity corrected with Lumogen red. (b) l DBR600, purely metallic nanocavity (d) Vertical dipole cavity corrected with F8TB8.

We summarised the experimentally corrected FDTD decay rates for both metallic and hybrid nano cavities in Figure 53. These values have been obtained by integrating over all the spectrum the curves from Figure 52 We can see how with the vertical dipole decreasing the particle size, we have an increase of the decay rate. A similar behaviour is observed with the horizontal dipole, despite the values being several orders of magnitude smaller depending on the particle size.

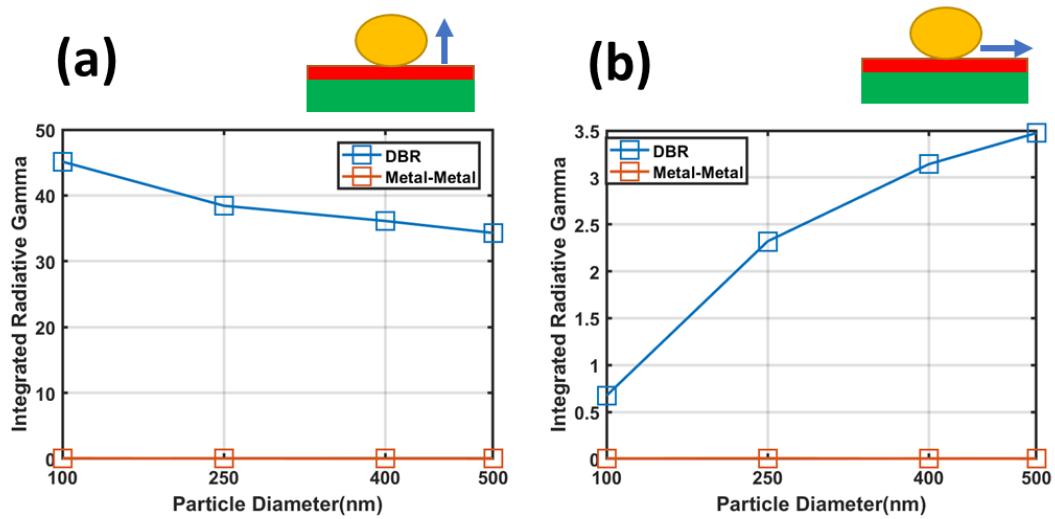


Figure 53 Summary for the FDTD decay rates corrected with the experimental emission spectrum for both gold and DBR nano cavity (a-b) vertical and horizontal dipole respectively.

In the next section we are going to see how we used Lumogen red and F8TB8T to realise the nano cavities experimentally.

## 5.2 EXPERIMENTAL RESULTS

After carrying out all these calculations, it is time to perform some experiments. We used a DBR with a central reflection wavelength at 600 nm Figure 54(c) to fabricate our samples.

### 5.2.1 HYBRID NANO-CAVITIES FABRICATION PROCESS

The FDTD calculations have been performed with two dipole orientations: vertical and horizontal with respect to the sample plane. We replicated these situations using two different emitting materials. A dye embedded into a polymer matrix to attempt to realise the vertical orientation and an emitting polymer for the horizontal one. The vertical orientation is achieved using a hosting polymeric matrix made of Zeonex ( refractive index equal to 1.42) doped with emitters from the Lumogen family (Lumogen Red). The hybrid cavities with vertical dipole orientation have been fabricated by spin coating onto a clean and freshly plasma treated DBR a 10 nm thick layer of Zeonex dissolved in Toluene doped with Lumogen red (5% in mass). A more detailed recipe can be found here [121]. The Lumogen red has been chosen as a quantum emitter due to the good spectral overlap between its emission spectrum, Figure 54 (b), and the experimental DBR reflection band Figure 54(c), and the minimum of the reflectivity of the second one. The high Quantum Yield (0.9) and its photochemical properties, such as, the high resistance to photobleaching [122], represent additional reason for this choice. The horizontal orientation instead is achieved using the red emitting polymer F8TB8T dissolved in toluene. The emission spectra of the polymer in Figure 54 is very similar to the Lumogen red one, therefore can reproduce the previous situation, but with a different orientation. Since the desired thickness of the emitting layer is 10 nm, the spinning parameters changed from time to time. The last step of the fabrication was the spin casting of the gold nano-spheres, in aqueous solution, onto the surface with a concentration of (0.005 mg/ml) to avoid the formation of clusters and have the possibility to execute single particle measurements. We carried out a systematic study by changing the gold nano-particles diameters (100, 250, 400, and 500) nm.

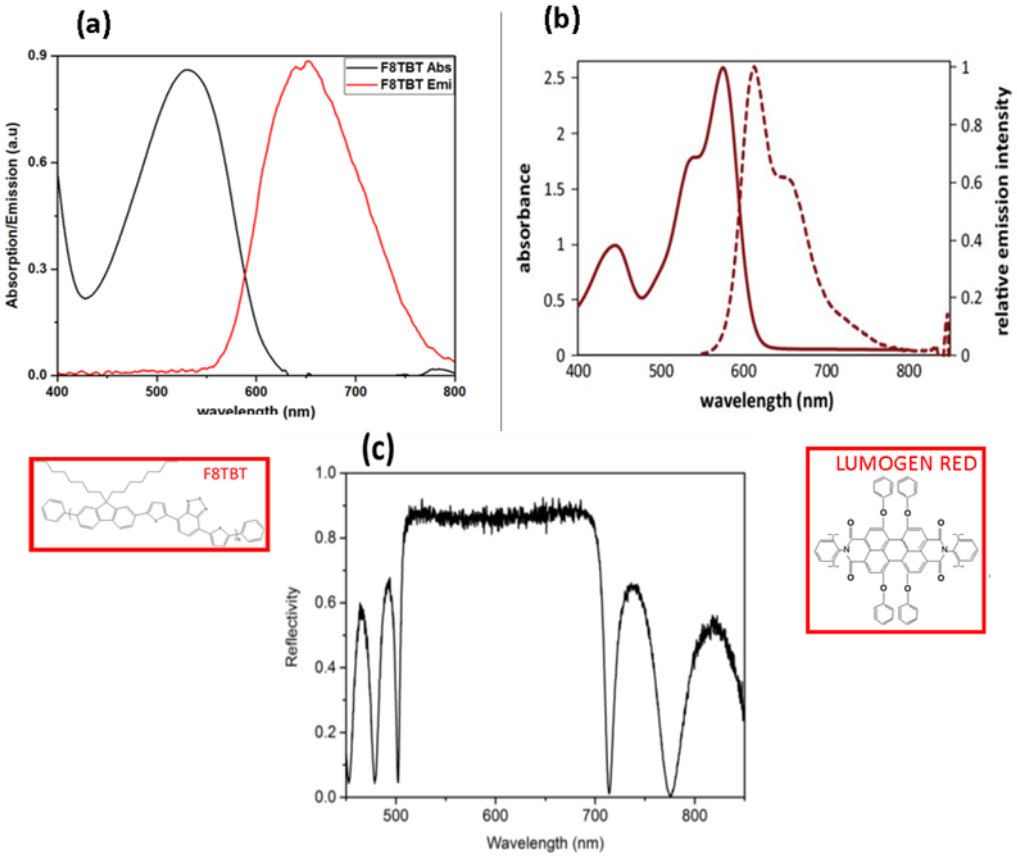


Figure 54 Absorption and emission spectra of (a) emitting polymer F8TBT, (b) Lumogen Red F. from [87] (c) reflection spectrum of the DBR used to fabricate the samples.

### 5.2.1.1 FLUORESCENCE CW ENHANCEMENT AND LIFETIME SPECTROSCOPY

The Lumogen red emission spectrum has a characteristic peak at 590 nm and a shoulder around 660 nm. Placing the emitter molecules into the nanocavity we observe an increase of the emission intensity with its maximum at 590 nm. This fluorescence increase is due to the cavity-emitter coupling [12]. The intensity enhancement, excited in CW, depends upon the particle size Figure 55(c,d). The largest intensity enhancement, about 50 times, takes place with the 500 nm diameter particle, instead the lowest, about 30 times, with the 250 nm one, Figure 55 (c,d). Another way to quantify the fluorescence enhancement is with the lifetime spectroscopy. The nano-cavity introduces new hybrid modes not available in the nano particle or DBR on their own. These hybrid modes modify the local density of states (LDOS) and consequently the radiative emission rate of the emitter changes [123] according with the Fermi's golden rule [124]. The Lumogen red in a Zeonex film has a lifetime of about 1.48 ns Figure 55(Red curve). In the decay curves relative to the nanocavity, two lifetimes are observed (352ps and 4.32ns) Figure 55 (b) (blue curve). One of these lifetimes is much faster than the other one. The fastest one is the lifetime relative emitting molecules coupled to the nanocavity, instead the slower one is relative to the molecules on the background. The lifetime has been measured in for the

two Lumogen red characteristic emission peaks. The radiative decay enhancement Figure 53 (a) is about 3-5 times, this value is modest comparable to other plasmonic systems [12] because our hybrid nano cavity has a thickness of barely 10 nm and many emitting molecules are quenched by such a vicinity to the gold particle. At the same time, however, we went really close to the instrument resolution of 200 picosecond, from Figure 55 we can see that the fast lifetime is 352ps. The author of [125] had to use dielectric layers to be able to reduce the quenching. We did not do it since we wanted to probe the properties of the smallest cavity possible.

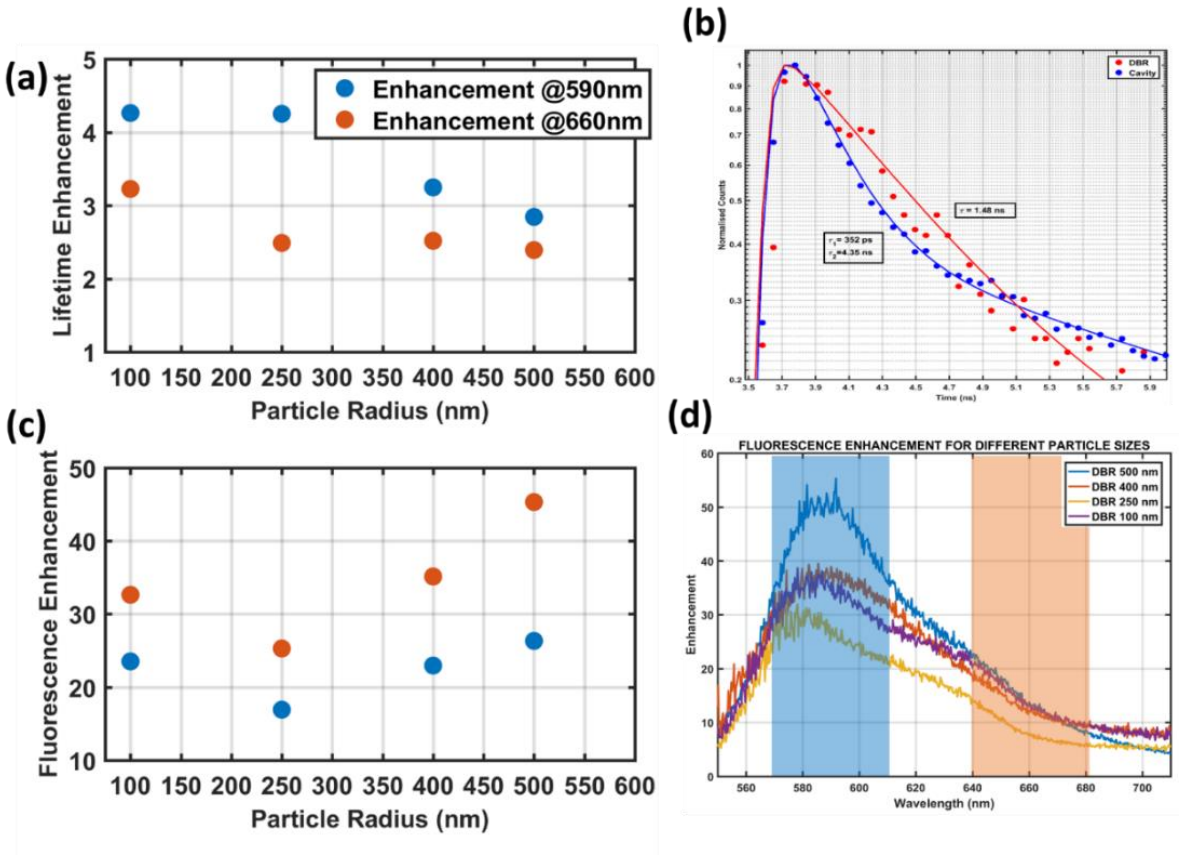


Figure 55 (a) experimentally measured lifetime enhancement for different particles size. (b) Example of lifetime decay for Lumogen red on DBR (red curve) and in a hybrid nanocavity (blue curve). (c) Measured fluorescence enhancement for different nanocavities. (d) Hybrid nano cavities emission enhancement for different nano particle size.

We have seen how the intensity enhancement determined from the emission spectra ranges between 30 and 50 depending upon the particle size Figure 55 (d), whereas the lifetime appears to shorten by only a factor 3-6. This discrepancy takes place because our Flim system reached the resolution limit. Lumogen red has a shorter lifetime already 1.5ns, therefore the cavity coupling shortens this time below the instrument resolution. Other red emitters with similar spectral properties and longer lifetimes were available, however they did not have the same preferential dipole orientation of the Lumogen red. In the next sections, we study the

modification of the emission diagram by the cavity to investigate the discrepancy between the CW fluorescence enhancements and the lifetime measurements.

### 5.2.2 EXPERIMENTAL EMISSION DIAGRAMS

We excited the fluorescence using the laser diode at 405 nm, a wavelength that does not match with the resonance of the isolated gold nanoparticle [126], the DBR reflectivity stop band, the hybrid nanocavity modes and with the maximum of the absorption of the quantum emitter. Therefore, it is possible to measure just the fluorescence enhancement due to the LDOS modification rather than the change of the excitation rate due to the emitter absorption at the excitation wavelength.

We studied the directionality of the emitted light using the k-space imaging technique. We used a high numerical aperture objective (NA = 0.9) to collect the emitted light, allowing us to probe the angular region spanning +/- 64° from the normal to the sample surface. The emission from our emitter on the DBR only is mostly concentrated into two lobes at the boundaries of the collection region, Figure 56 (a). The nano cavity, instead, emits all over the measurable angular span Figure 56(b). The emission intensity enhancement is more pronounced in the region perpendicular to the surface Figure 56(a), especially in the ± 20 degrees region perpendicular to the surface.

We can obtain a degree of tunability by changing the particle size, as shown by the different angular emission diagrams on Figure 56(b). The 500 nm cavity gives us the sharpest emission diagram and the 250 nm the broadest one. The angular emission broadening in the enhanced emission follows the same trend of the fluorescence intensity enhancement observed in Figure 55(c).

Since the fluorescence lifetime is a property of the quantum emitter and its surrounding environment, its measurement does not depend on the intensity of the detected signal as it is an intrinsic physical property extracted via a fit from a time dependent signal. Therefore, the fluorescence lifetime is independent of the directionality of the light as the undetected photons emitted outside the collection area of the objective do not influence the arrival time of the photons and therefore the global lifetime. We must point out though, that the size probed region is as large as the spot size and the dipole orientation is averaged over all directions.

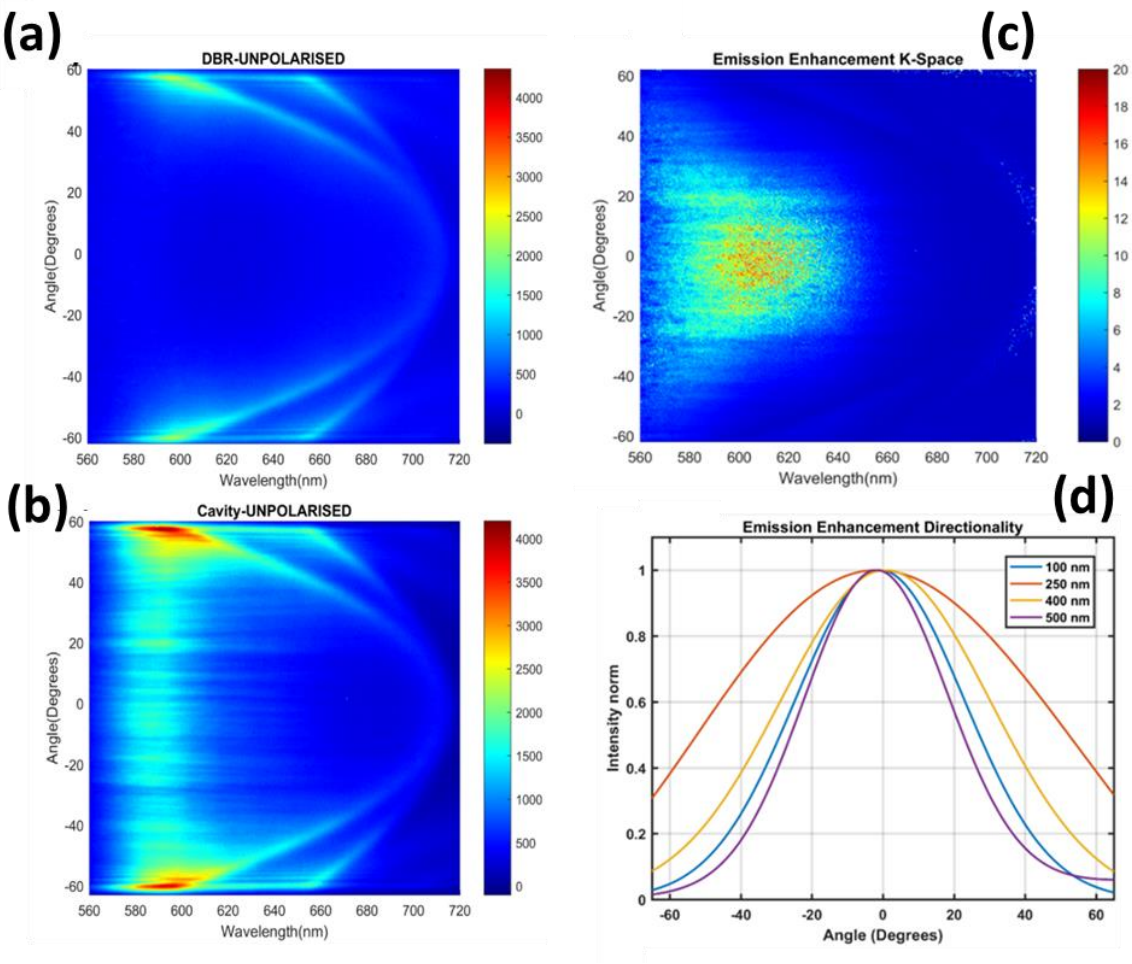


Figure 56 (a) K- space image of the emission recorded on DBR, (b) on cavity Lumogen Red, mean dipole vertical. (c) Emission enhancement in k-space for a 500 nm nano particle, (d) k –space emission diagrams for a wavelength of 590 nm for different particle sizes.

On the other hand, the technique based on the integrated spectra is sensitive to the directionality of the emission: the measured spectrum is the sum of all the signals over all the collected angles. The photons going out of the collection do not provide a contribution to the normalization spectrum and hence the signal intensity increases, not only because there is a stronger signal emitted from the nano cavity, but also because the cavity redistributes the angular emission into the collection cone. To compare directly the performances of the hybrid nano-cavities with the ones of a purely metallic nano gap a similar device was prepared using a 100 nm thick silver film instead of the DBR but keeping the emitting layer thickness and the nanoparticle diameter constant.

We replicated the k-space measurements on the same red DBR but changing the emitter orientation. We used F8TBT because it has a horizontal dipole moment once spun in a thin film

and it exhibits an emission spectrum similar to the Lumogen Red  Figure 54 (b-d) but ensures that the fluorescence dipole moment is majoritarily in the plane of the sample. In Figure 57, we have the k-space emission recorded with horizontal dipole, (a) on 250 nm particle cavity, (b) reference emission on DBR, Figure 56 (c) ratio between the two. We can see how the enhancement factor is at least one order of magnitude lower than the vertical case. This reduction of the emission was expected because of Fermi's golden rule. We can see how the horizontal reference has light the first Bragg mode at low angle, plus two red shifted lobes at high angles compared to the two isolated lobes of Figure 56 (a). The difference in the emission diagram is not as remarked as in the vertical orientation. This is due to the low coupling consequence of the Fermi golden rule. In addition, we can find the two emission lobes at the edges of the collection region.

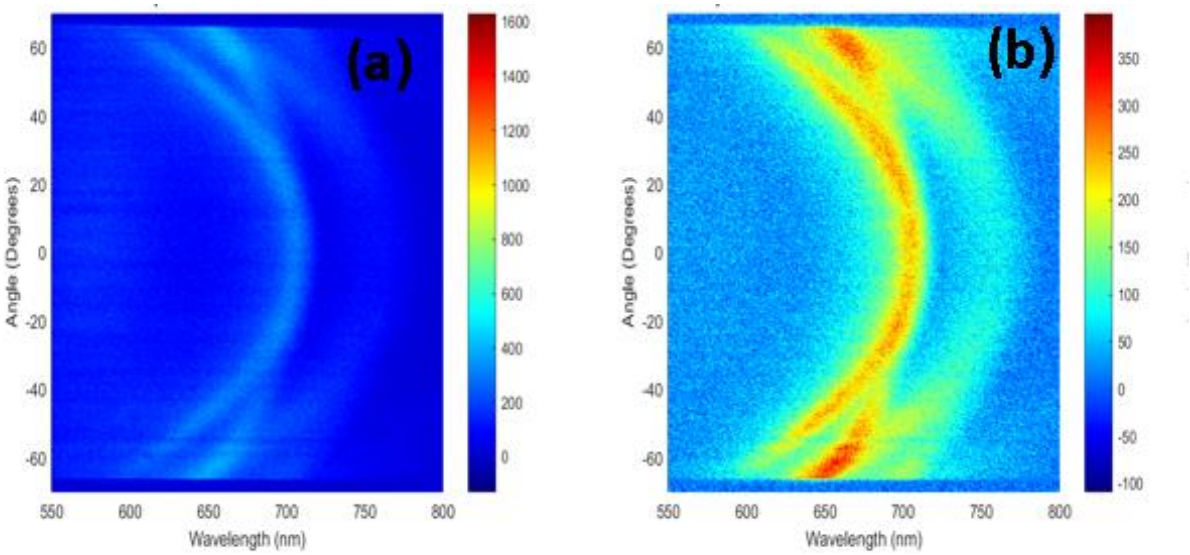


Figure 57 K-space image of (a) 250 nm hybrid nanocavities using emitting polymer F8TBT of the emission. (b) F8TBD Emission recorded from the DBR surface.

## 5.3 FDTD FAR FIELD PROJECTIONS

The emission diagrams can be simulated using FDTD simulation and the technique of the near to far field projections. The dipole orientation is perpendicular to the DBR surface (vertical). [120]

### 5.3.1 FAR FIELD HYBRID NANO- CAVITIES

The simulation in Figure 58 show us these results for a vertical dipole positioned in the middle of the nanocavity. Panel (e) is used as the reference and corresponds to the emission of the dipole in the spacing layer above the DBR only, where the light can be seen to be emitted at angles as high as 75 degrees. Panels a, b, c, d represent the calculations performed in presence

of a nanoparticle of diameter 100 nm, 250 nm, 400 nm, and 500 nm respectively. By introducing the nano particle to form the nano cavities, we can see that the emission diagrams are changed compared with the DBR reference. Just as we did for the experimental results, we can observe a trend as a function of the nanoparticle size: the 500 nm cavity emits the in a smaller angle cone, instead the 250 nm in the broadest one. The 250 nm particle (b) has broader emission lobes ranging from 25 to 50 degrees. The 400 nm (c) results to be weaker coupled than the other ones and the emission lobes are even further spectrally broaden. Last (d) 500 nm has still two emission lobes, but more localised and shifted in the range 20-40 degrees. This last case is confirmed to be the most directional system since most of the light is emitted more perpendicular to the surface than all the previous cases.

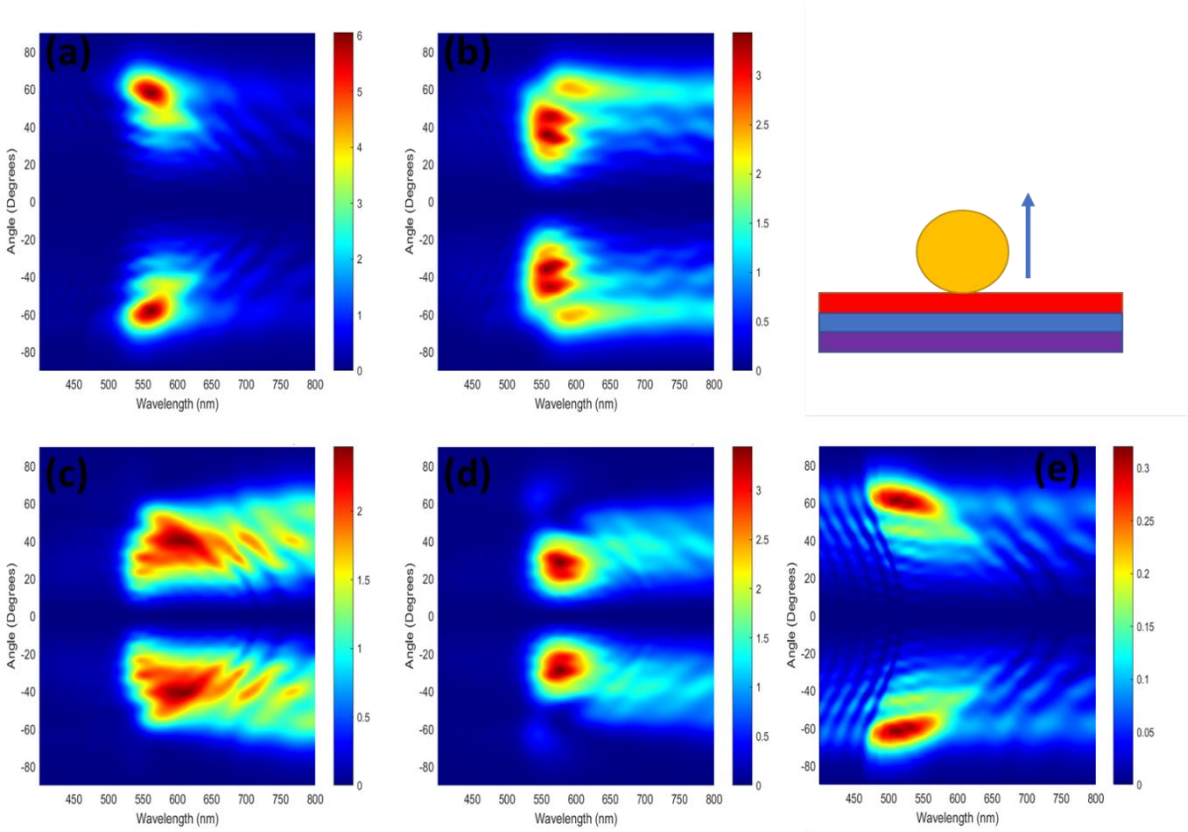


Figure 58 Far field simulation for a hybrid nanocavity made by the red DBR and gold nanosphere with a diameter (a) 100 nm, (b) 250 nm, (c) 400 nm, (d) 500 nm and (e) reference simulation with a dipole on a DBR. Dipole orientation Vertical, perpendicular to the surface

On the other hand, when the dipole orientation is parallel to the DBR surface (horizontal), Figure 59, we can immediately notice some substantial differences with Figure 58, namely, with the dipole perpendicular with the surface. First, the reference case panel (e) with intensity of the E-field is higher when the dipole is vertical, rather than when it is in the horizontal position. This happens because the dipole lying flat on the surface is in the optimal position to have its light reflected in the direction of observation. The radiation pattern is quite different with this

dipole orientation. Particularly for the larger particle sizes, panels (b, c, d), we can see how the emission diagrams have three lobes one highly localised at zero degrees and two smaller ones around 60°. Secondly, when we introduce the cavity (adding the nano particle), the E-field is 10 to 20 times more intense than when the dipole on DBR reference. This is a clear evidence that the dipole is coupled with the cavity, indeed the enhancement is the highest when the dipole orientation is perfectly parallel to the cavity moment. With the dipole horizontally aligned, it is therefore normal to expect a lower signal output since the dipole cavity coupling is weak.

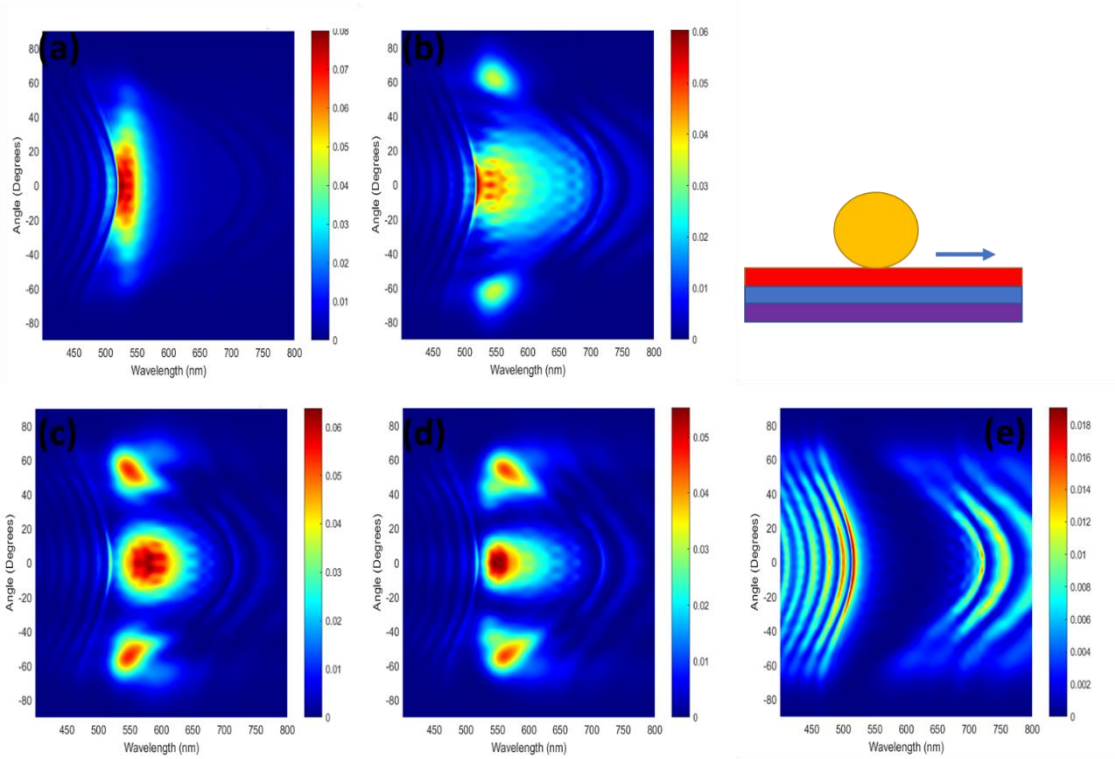


Figure 59 Far field simulation for a hybrid nanocavity made by the red DBR and gold nanosphere with a diameter (a) 100 nm, (b) 250 nm, (c) 400 nm, (d) 500 nm and (e) reference simulation with a dipole on a DBR. Dipole orientation Horizontal, parallel to the surface.

The main discrepancy between calculations and experiment is the absence of signal emitted at 0 degrees in the simulations. This is explainable because the emitting dipole is placed in the centre of symmetry of the whole nano cavity. The dipole orientation is perfectly orthogonal to the surface. In the next section we are going to see how the emission diagrams are influenced locally by the change of the refractive index.

### 5.3.2 FDTD REFERENCE CALCULATIONS

To further understand the optical properties of these hybrid nano-cavities we performed some control simulations to figure out how some external parameters can change the emission diagrams.

We repeated the calculations for a purely metallic nanocavity. We kept the active layer thickness fixed to 10 nm. Johnson and Christy [127] is the dataset used for the gold optical constants.

It can be seen on Figure 60 and Figure 61 that, independently of the dipole orientation, little change in emission diagrams is observed due to the change of the particle size. For a vertical dipole, we see the presence of two lobes peaked around 60 degrees. The lobes positions seem moving slightly toward the centre by increasing the particle size. With the horizontal orientation, we have only one lobe spreading across most of the angular span for the 100 nm particle case. Increasing the particle size, the emission lobe squeeze further reaching the 20 degrees span for the 500 nm particle

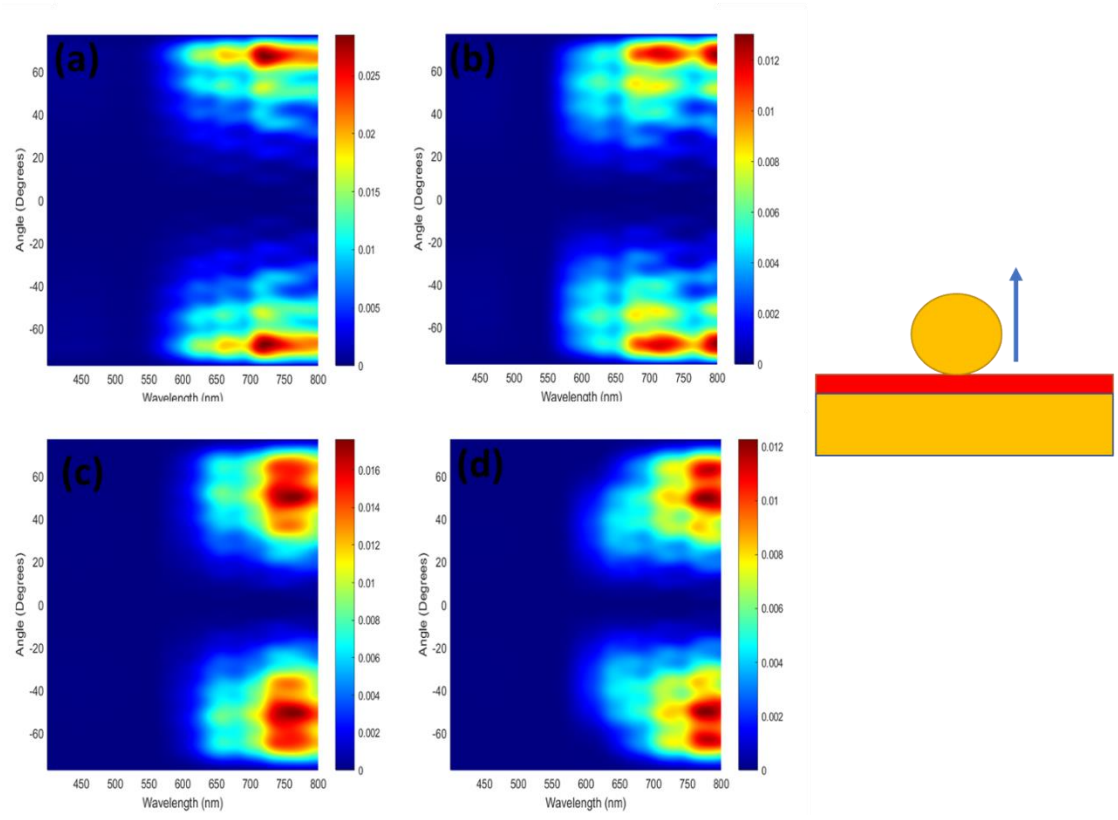


Figure 60 Far field projection for a purely metallic nano cavity. Different nano particle diameters: (a)100 nm, (b) 250 nm. (c) 400 nm and (d) 500 nm. Dipole orientation Vertical.

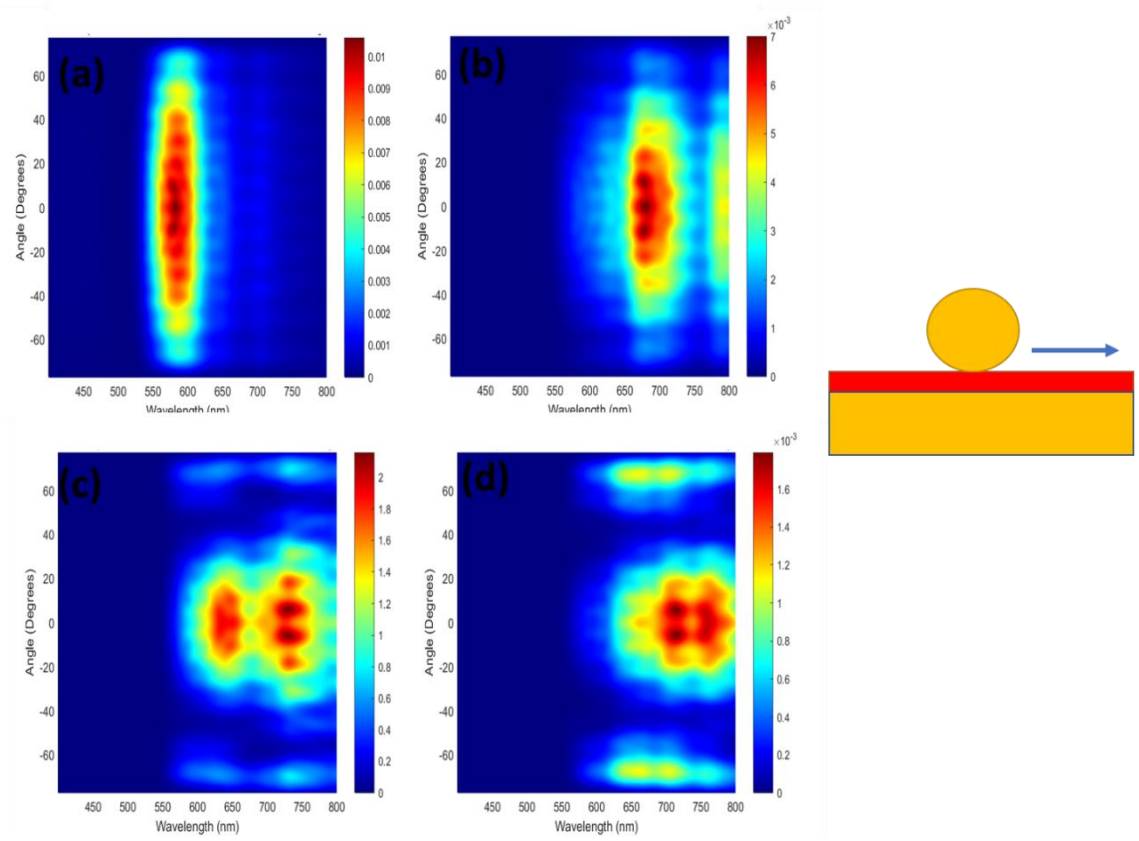


Figure 61 Far field projection for a purely metallic nano cavity. Different nano particle diameters: (a)100 nm, (b) 250 nm. (c) 400 nm and (d) 500 nm. Dipole orientation Horizontal.

In the next paragraph we are going to see how even a small change in the relative position of the dipole versus the centre of symmetry of the cavity will dramatically change the emission diagrams shape.

#### 5.3.2.1 IMPORTANCE OF DIPOLE POSITION IN THE CAVITY

We adapted the modelling to explore the origin of the emission observed experimentally at lower angles (close to normal incidence) where it appears to be dark in the single dipole calculations. We perform this control simulation by fixing the particle size to 500 nm and the dipole orientation to vertical. We moved the dipole position along the x axis as a proof of concept and to avoid losing an additional degree of symmetry. We moved the dipole from the x=0 position in steps of 10 nm along the x axis until 40 nm, and then for x=60, 80, 100, 150 and 300 nm. We recorded the near to far field projection at each step. Figure 62 We can see that the symmetry of the emission diagram, with two emission lobes observed for a dipole in the middle of the cavity, start to be broken as the dipole is displaced. Once the dipole is displaced by 60 nm from the centre of the cavity, light is emitted in the central angular region. The effect is even more visible in Figure 62 **Error! Reference source not found.**(c), where we performed an angle section at the wavelength of 550 nm and plot them together. We can see that when the dipole position increases, the signal intensity in the region perpendicular to the substrate

increases accordingly, dropping abruptly in intensity once the dipole is positioned 100 nm away from the cavity centre, namely when it is outside of the cavity hot spot. Finally, for a dipole positioned 300 nm from cavity centre, the far-field emission diagram converges to the one observed for a dipole on DBR alone, illustrating a greatly reduced coupling with the nanocavity mode.

With those calculations we show how the relative position between dipole and nanocavity centre changes the far field projection making the light emitted into the central region as well, in agreement with the experimental results (Figure 65(b)). By adding more dipoles, it is possible to fill the gap between the two emission lobes, and therefore obtain an even more realistic representation of the experiment.

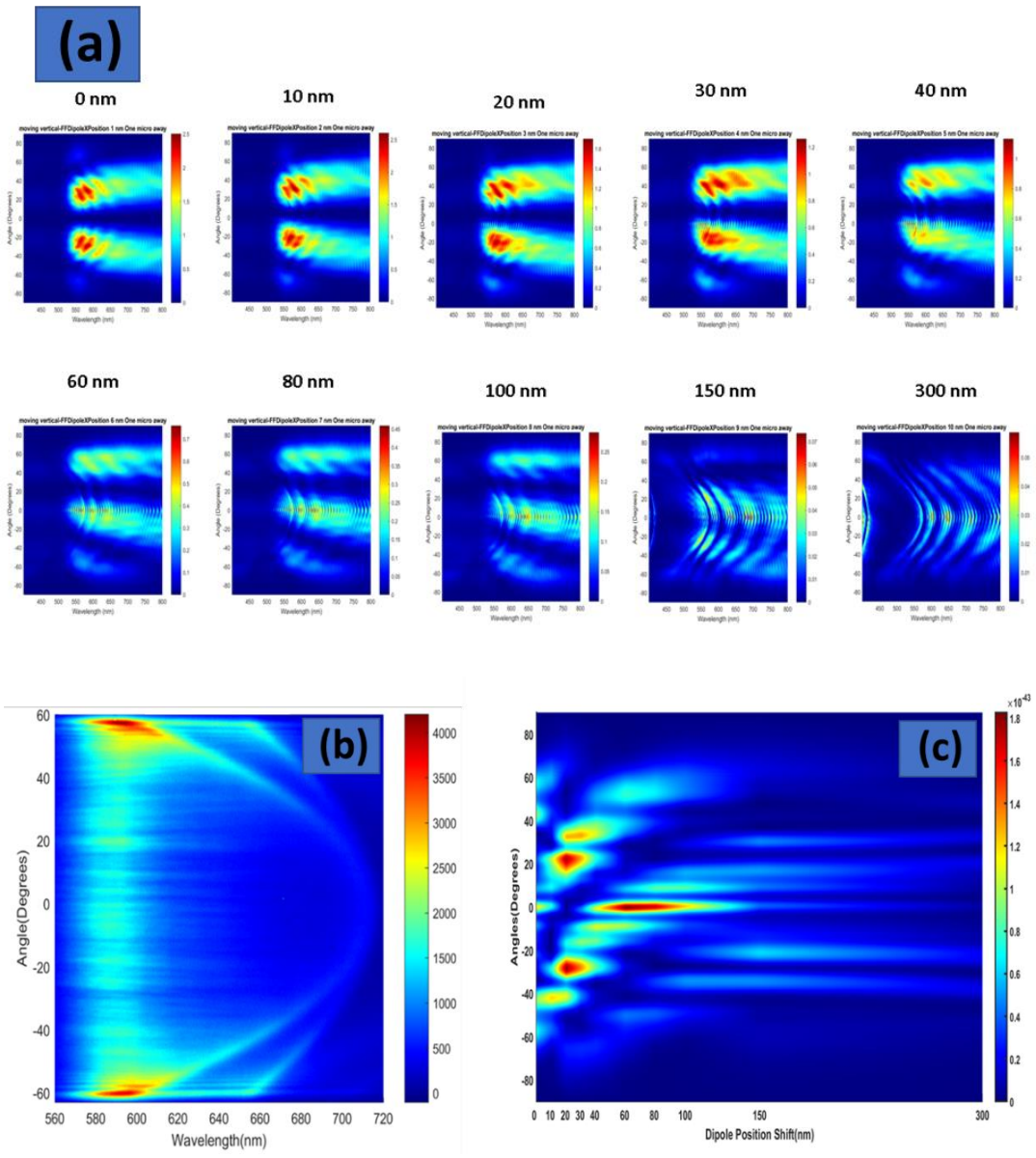


Figure 62(a) Change of the emission diagrams recorded at different dipole position a hybrid nanocavity. Dipole orientation Vertical. Moving dipole far field section at the resonance plotted vs the dipole position.

Dipole orientation Vertical. Particle size 500 nm. (b) Experimental recorded case, (c) Experimental cross section of (a) measured for each dipole position at the wavelength of 550 nm, raw data.

## 5.4 EXPERIEMENTS vs SIMULATIONS COMPARISON

FDTD simulations are excellent modelling tools, but by their nature they can describe only quasi-ideal systems. This can lead to a certain mismatch between model and experiment. The role of the simulation is to expand the experiment and to help understand the results. In this section a comparison between experimental and modelling results is presented. The two most critical factors are related with the dipole properties, in the specific, the orientation, the number of dipoles, the position in the nano gap respect the gold sphere.

The dipole in the simulation is single, in the real experiment the probed area using a 405 nm laser is roughly 250 nm, namely hundreds of Lumogen red emitting dipoles are contained. Placing several emitting dipoles will make the calculation unstable. The instability is due mostly to interference between all the radiated waves. Multiple emitting dipoles in such a small space will make the autoshut off constantly oscillating, this will lead a very long simulation time (several weeks). An alternative would be to set an even longer simulation time to allow a proper decay, this will make the simulation even longer. The nano gap studied here, however, allows to consider the whole volume as single dipole. It is possible to do this approximation since the main aim here is to observe the change of emission diagram from the cavity into the far field. The orientation of the dipole is a critical parameter, the Fermi's Golden rule described in chapter one states that the intensity of the dipole-cavity coupling is a maximum when the dipole and the cavity moment are perfectly parallel. The average orientation of the Lumogen red molecules embedded in the emitting film can be considered vertical as explained in section 5.2.1.

The last critical parameter is the dipole position compared to the nano gap centre of symmetry, the influence of such a physical distance has been simulated in Fig.63. Experimentally, as said before, it is possible to probe an area that is roughly the size of the laser wavelength. In fig. 63(c) it is possible to see how when the dipole is moved 80 nm away from the centre, the largest amount of light is redirected in the angular range perpendicular to the surface. Moving the dipole relatively to the gaps centre of symmetry has the same effect of moving the feed of an antenna. The main discrepancy between calculations and experiment is the low light emission in the angular rag 0-30 degrees. This happens because the excited region in the experimental case is so wide, roughly 200 nm, and involves even the molecules placed out of the cavity hotspot. This difference can be explained by considering both the large number of molecules (hundreds) and the relative position between cavity and molecules.

## 5.5 CONCLUSIONS

In this chapter we have seen the optical properties for a hybrid nano cavity made of a distributed Bragg reflector and a gold nano sphere. In this work, we coupled the DBR reflective band to greatly reduce the losses of the traditional metallic nano particle on mirror system. We used FDTD calculations to model the properties of such a system. We simulated the non-radiative and radiative decay rate enhancements and we saw that the latter can get as high as 120. For comparison, we simulated the purely gold nano cavities with the same cavity parameters, and we saw that the radiative decay rate is a factor 10 higher in the hybrid nano cavities. We saw better performances with the vertically oriented dipoles as expected from the Fermi golden rule and the known cavity field orientation. E field images of the DBR hybrid nano cavity section showed that the coupling happens mostly in the first few layers.

The emission diagrams have been calculated as well. The field was more intense with the vertical dipole rather than with the horizontal one because of the Fermi golden rule. In terms of emission pattern, we saw that the vertical dipole placed on a DBR tends to have an emission at high angles, more than 60 degrees. Introducing the nano particle to form the cavity, the emission changes and shifts more at angles more orthogonal to the surface with a great tunability upon the particle size. With the horizontal dipole we saw one lobe orthogonal and two smaller lobes at high angles. The shape of the mode's changes again upon the particle size.

The nano cavities have been realised experimentally choosing a DBR which reflective band was centred around 600 nm, we used the dye Lumogen red to replicate the situation of the vertical dipole and the emitting polymer F8TBT for the horizontal one. With the Lumogen red we saw an emission enhancement intensity reaching up to factor 50. The emission pattern was recorded using the k-space imaging technique. We observed the two emission lobes at high angle previously recorded on the DBR reference far field calculation. We saw, via the k-space imaging, that the emission enhancement was focused into a cone 20 degrees wide orthogonal to the surface. The calculation predicted that the emission lobes were going toward the centre once introduced the nano cavity, but not into this region. We explained the discrepancy via FDTD refinement calculation. We show that the emission pattern is sensitive to the relative position between dipole and the nano cavity centre. We showed that a change of the dipole position as small as 50 nm makes the light being emitted orthogonally to the surface. We investigated the horizontal orientation using the emitting polymer. We saw not a specific enhancement pattern like in the previous case.

However, the horizontal is perfect to couple the emission with the Bragg modes of the DBR rather than with the hybrid nano cavity. In the next chapter, we study another physical regime in which the DBR is not used as mirror, but rather like a photonic crystal, by considering the coupling with the DBR 1$^{st}$ Bragg mode instead of the stopband.

# Chapter 6 ISOLATED SUPER-TAMM MODES

The coupling between a plasmonic element and a photonic mode is going to be described in this chapter. It is well-known that the coupling of the 1st Bragg mode of 1D photonic crystals (DBR) with an extended metallic film leads to the creation of Tamm states. To probe the coupling between the 1st Bragg mode and the plasmonic particle, we will consider 3 different DBR arrangements, each with a slightly different stopband, and therefore a different 1st Bragg mode spectral position. we scan the 1st Bragg mode spectral position across the plasmonic nanoparticle localised resonance Figure 63 (a) and explore the modification of a dipole emitter emission positioned in each hybridised system. Tamm plasmons are surface state that can be excited at the interface between a DBR and a metallic layer. These states found several applications in micro-lasers [68][69], spontaneous emission control [128]. Another quality of Tamm mode is the super- Tamm mode [70]. A super Tamm plasmon is a surface mode with intermediate behaviour between Bragg modes and conventional Tamm plasmon. Super Tamm states were firstly theorised by M. Kaliteevski et al. in 2007 [65] and then experimentally reported by C. Symonds et al in 2017 [70]. Bragg modes have high penetration into the DBR stack, instead Tamm plasmons lay close to the interface between a DBR and a metallic surface [70]. Super Tamm modes are still partially confined within the metal; however, they extend further into the DBR, see Figure 9. Super Tamm are excitable only in planar film geometries. In this work we show that it is possible to excite highly localised Tamm states with simpler nano sphere cavities.

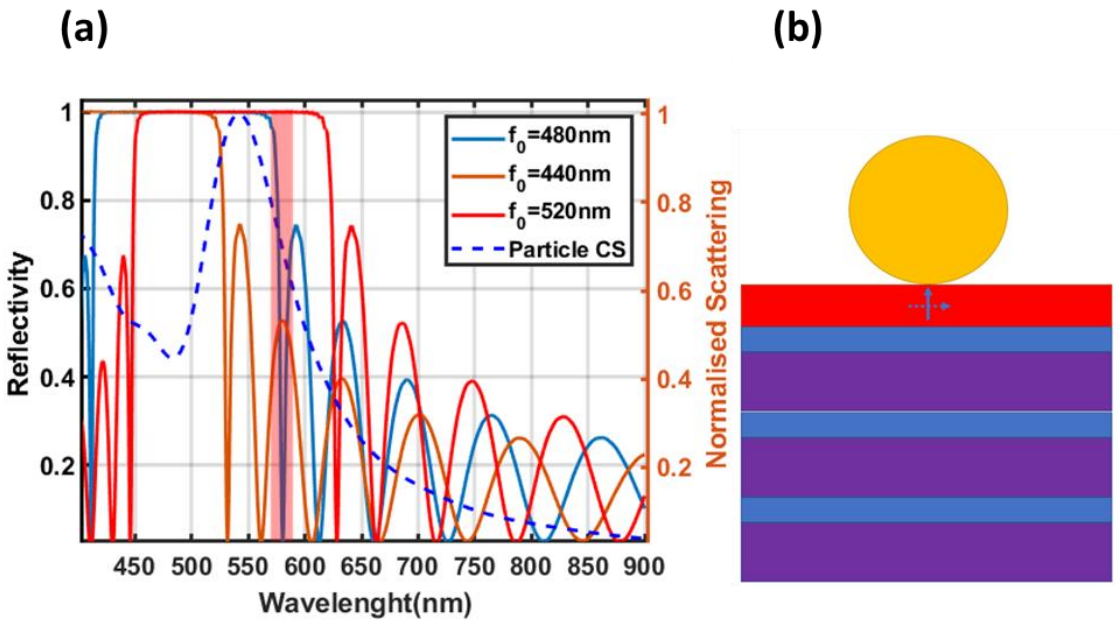


Figure 63 (a) Overlap between a f0=440 nm , f0=480 nm, f0=520 nm DBR reflectivity spectrum and 100 nm diameter Au nano sphere scattering scross section CS. (b) Schematic representation of the hybid nano cavity system. We studied the physical regime inside the DBR first Bragg mode.

## 6.1 FDTD CALCULATION

The structure studied in this chapter is analogous to the one of the previous one, indeed we kept the DBR refractive indices the same as in the previous chapter, the same was done for the particle sizes. We performed different calculations to determine the optimal DBR stop band to have a perfect overlapping of DBR first Bragg mode and nano particle extinction and dye emission for the experimental case. For this study we used six different DBRs, with central wavelength f0 ranging from 400 nm to 600 nm in steps of 40 nm. In a first instance, we studied the traditional super-Tamm plasmon arrangement: a 20 nm thick infinitely extended gold film is used in the formation of the hybrid nano cavity, deposited on top of a 10 nm thick active layer, on top of a DBR. This study was performed to better understand the dynamics of the Bragg first mode and to determine the position of the Super Tamm Mode for each DBR.

### 6.1.1 FDTD GOLD LAYER CAVITY

In Figure 64, we have the results of such calculations. We can see that around the 1$^{St}$ Bragg mode we have coupling, which intensity increases when the mode position reached the green part of the spectrum, as the losses due to the gold are reduced. In Figure 64 (h), we have the position of the super Tamm mode obtained from the calculations in Figure 64. Those points are obtained by plotting the Far field section at 0 degrees and identifying the position of the blue shifted peak respect to the 1$^{st}$ Bragg mode. The super Tamm spectral position is always blue shifted to the 1$^{st}$ Bragg mode and increases linearly with the DBR central wavelength.

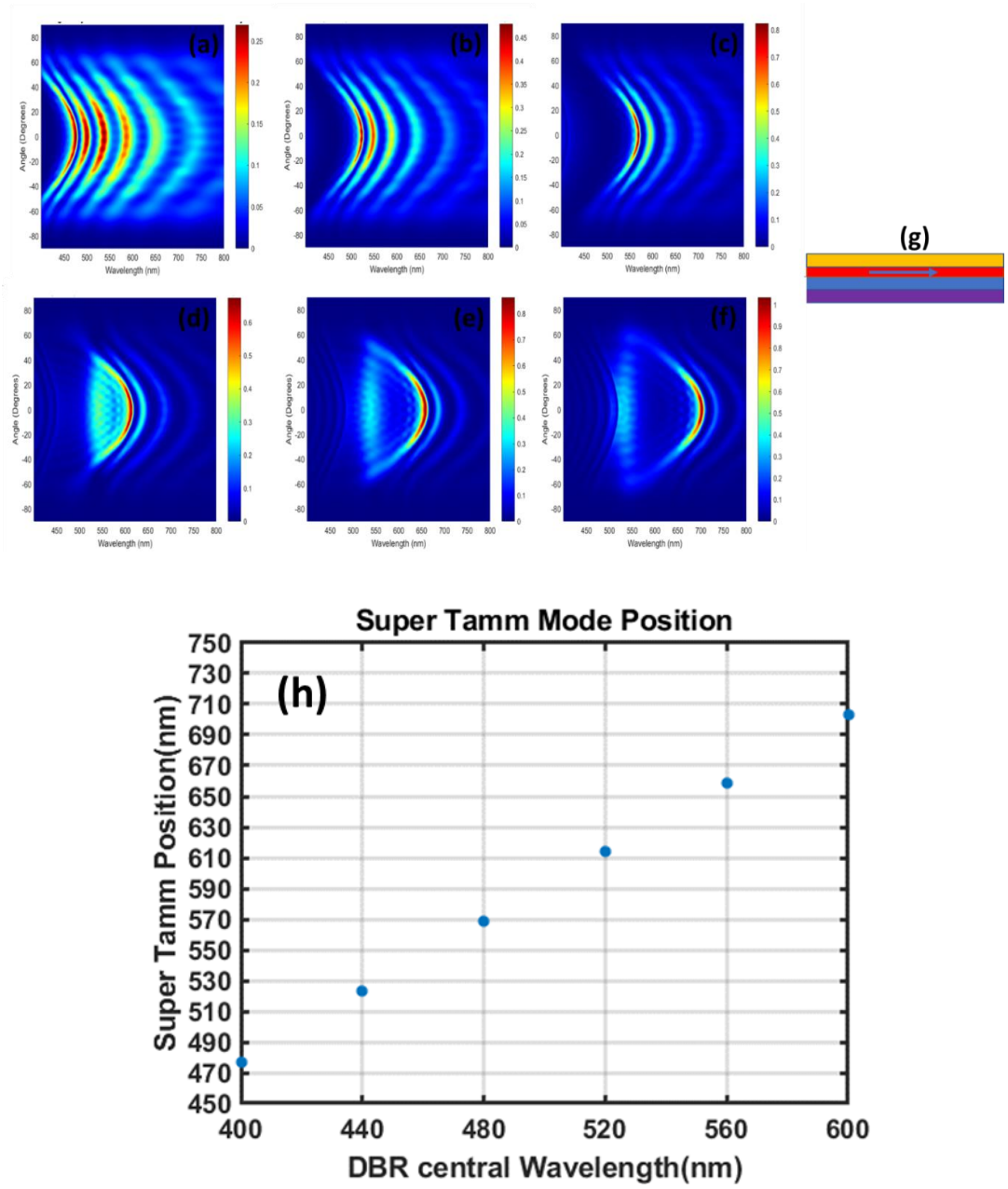


Figure 64 Far Field projections of a hybrid cavity made by a Gold film spaced onto different DBRs. The changing parameter is the central stopband wavelength: (a)400 nm, (b)440 nm, (c)480 nm, (d)520 nm, (e)560 nm, (f) 600 nm. (g) Representation of the simulated system. The arrow is the dipole orientation. (h) Theoretical Super Tamm mode position for each system a-f.

### 6.1.2 FDTD GOLD NANO SPHERES CAVITIES

As preliminary test we decide to give a look at the electric field intensity inside a nanocavity at the 1st Bragg mode. In Figure 65, we can see the differences in the E-field distribution between horizontal and vertical dipole in such a system.

With the Vertical dipole (a) we have a large portion of the electric field radiated toward the outside and large cone in the DBR where the field did not penetrate. The horizontal dipole instead, has a stronger portion of the electric field penetrating inside the dielectric stack. To better model the emission diagrams we used the far-field projection technique.

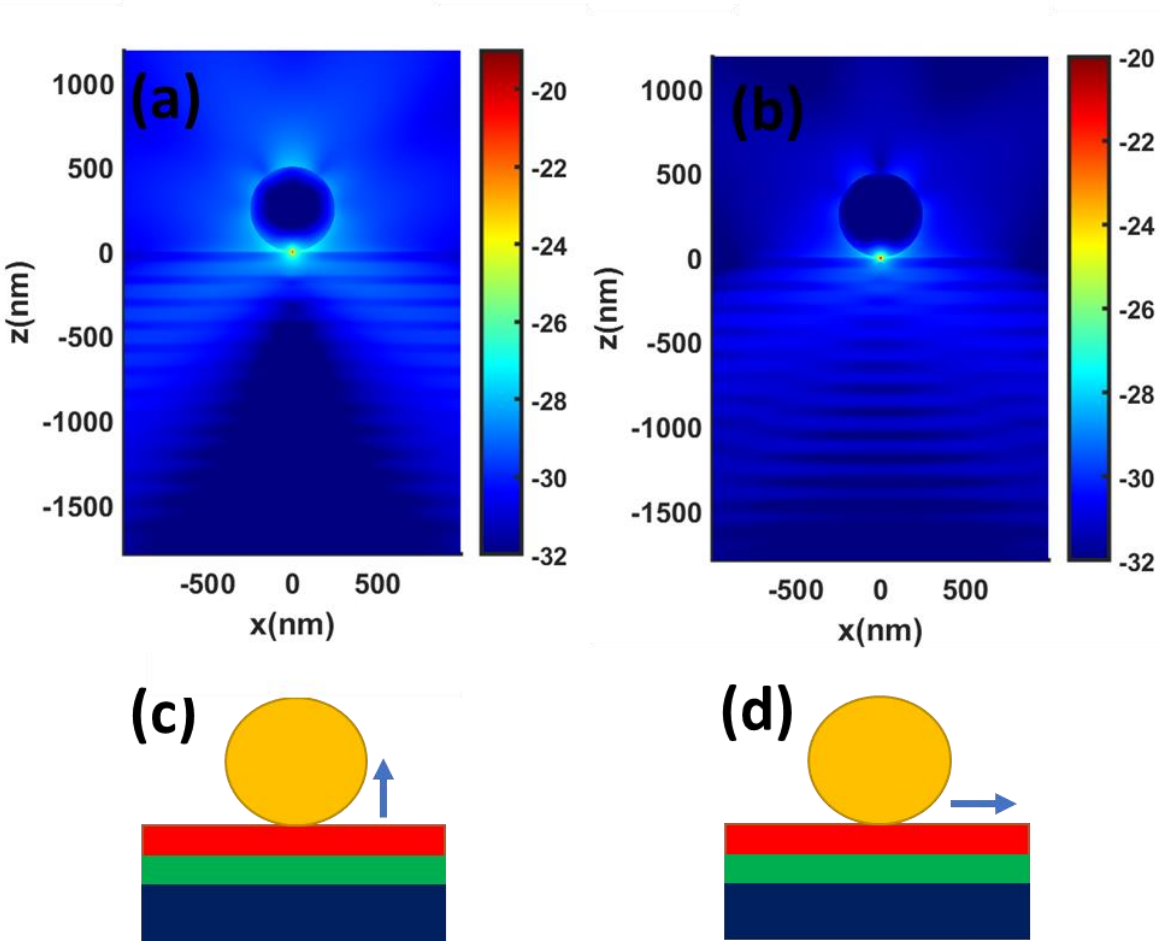


Figure 65 Electric field intensity in log scale measured at the first Bragg mode (581nm). Particle size 500 nm. (a)Vertical dipole (b) horizontal dipole, (c-d) cavity representation for (a) and (b) respectively. Intensity scale in log units.

In Figure 66 we have the simulations for the far field projections performed with the dipole in vertical position. The Vertical dipole follows a similar trend observed with the previous chapter as well. The electric field maps in Figure 66 show that the DBR is not acting as a resonator with this dipole orientation, making the vertical dipole not suitable for our study at the Bragg mode.

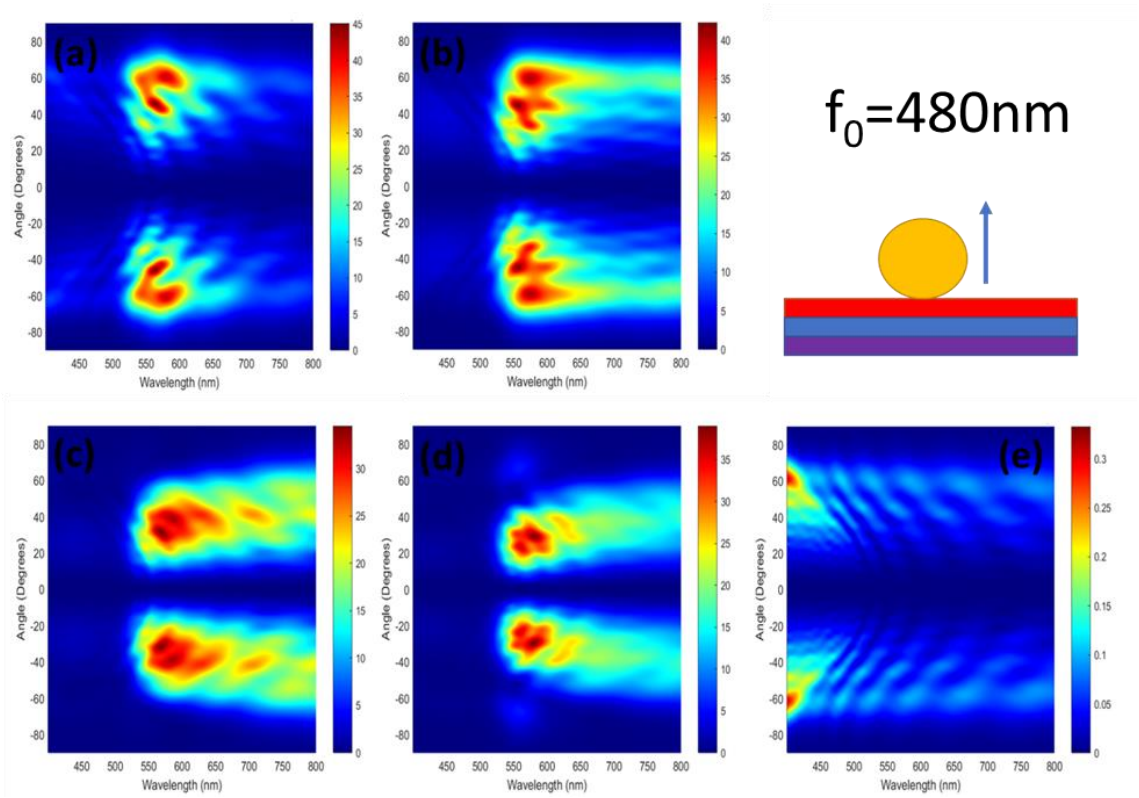


Figure 66 Far field simulation for a hybrid nanocavity made by the f0=480 nm DBR and gold nanosphere with a diameter (a) 100 nm, (b) 250 nm, (c) 400 nm, (d) 500 nm and (e) reference simulation with a dipole on a DBR. Dipole orientation Vertical, perpendicular to the surface.

### 6.1.3 STOP BAND TUNING

For the standard Tamm-state, coupling with a smooth metal film, the spectral overlap is less critical since the smooth metal film supports SPPs at all frequencies below the surface plasmon frequency. The localised modes of the nanoparticle, on the other hand, have well defined spectral resonances. For this reason, if we want to couple the 1st Bragg mode with the nano sphere resonance, a careful tuning of the DBR band gap has to be carried out. A more interesting behaviour arises with the horizontal dipole orientation. We can see from Figure 67 the emission is tightly localised around the 1$^{st}$ and 2$^{nd}$ Bragg mode. For larger particles (c-d) the angular dispersion is even narrower. We stress out that these calculations have been performed with a single dipole placed in the centre of symmetry of the cavity. Decreasing the particle to 400 nm we obtain a further localisation of the central lobe. The highest angle emission confinement is obtained with the 250 nm particle figure (b), as we can see all the emission is tighly localised arounf the 1$^{st}$ and 2$^{nd}$ Bragg mode. The coupling with the 100 nm particle, looks the weakest among the 4 cases. These calculations show a better confinement than the regime studied in chapter 5.

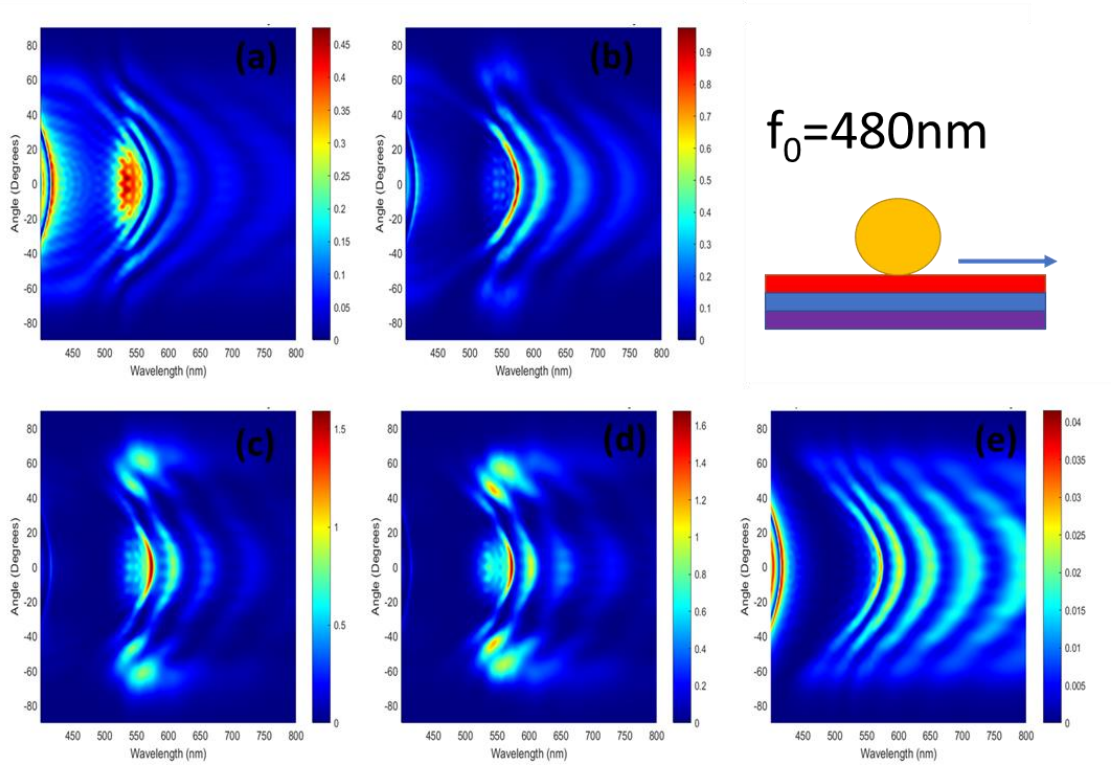


Figure 67 Far field simulation for a hybrid nanocavity made with different f0=440 nm DBR and gold nanosphere with a diameter with a diameter (a) 100 nm, (b) 250 nm, (c) 400 nm, (d) 500 nm and (e) reference simulation with a dipole on a DBR. Dipole orientation Horizontal, parallel to the surface.

Looking at this data, we notice a certain reminiscence with a super Tamm mode. The effect of a super Tamm state is a blue shifted peak with respect to the 1st Bragg mode. We measured this from the far field calculation in Figure 64 by measuring the spectral profile at 0 degrees and observe the position of the blue shifted peak near the 1st Bragg mode. We repeated the same procedure for the far field projections performed on hybrid nano cavities. Figure 68 (a) shows an example far-field cross-section. In Figure 68(b-c-d) we show the spectral position of the peaks measured for different reflection bands, plotted with the spectral position of the DBR 1st Bragg mode and the super-Tamm identified in Figure 67. For all particle sizes, the observed peak is blue shifted compared to the 1st Bragg mode and this wavelength is always longer than the theoretical super-Tamm one. Moreover, for a given DBR substrate, increasing the particle size always results in a blue shift of the super-Tamm mode: the 100 nm particle has a peak closer to the 1st Bragg mode instead the 500 nm closer to the super-Tamm. The blue shifting is almost linear with increasing the particle size.

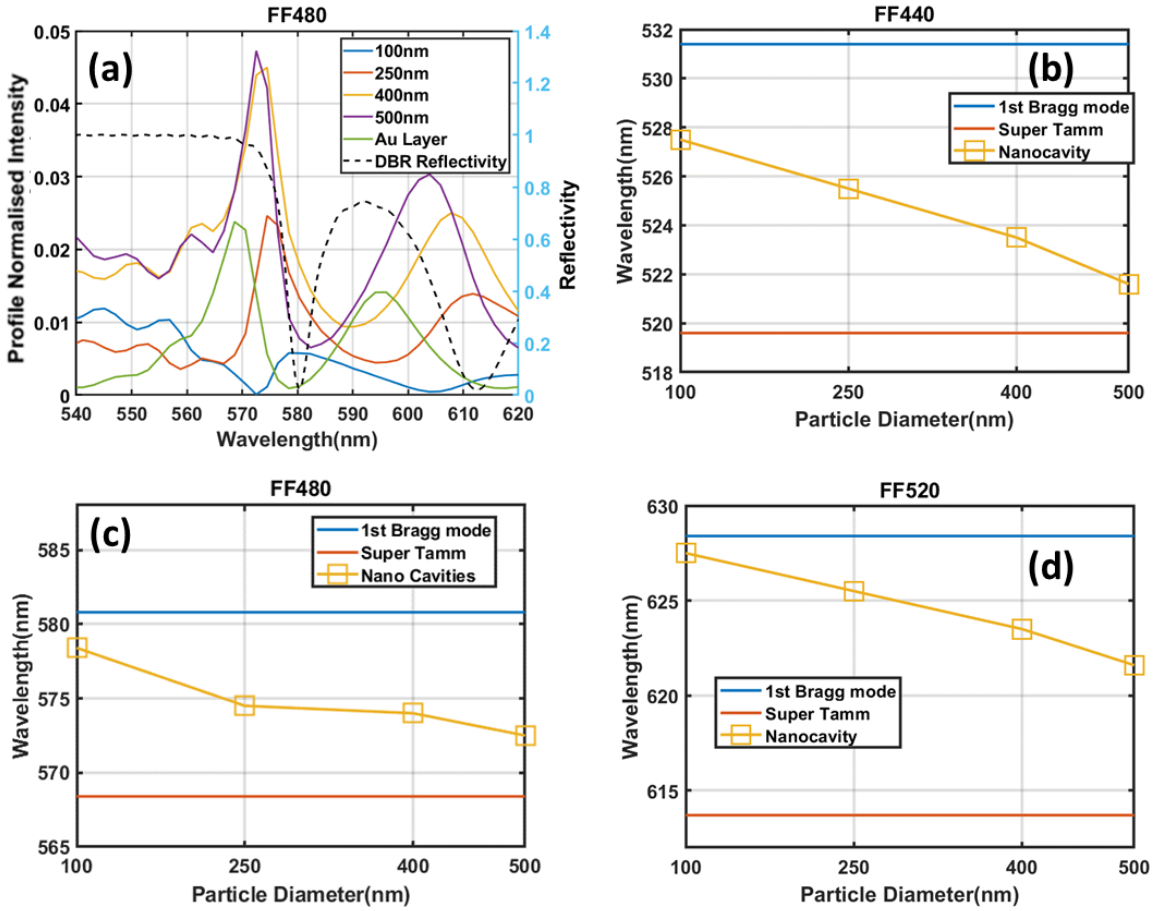


Figure 68 Example of Far field profile recorded for different nano cavities compared with calculated the DBR reflection spectrum. Zoomed around the 1st Bragg mode wavelength (581.4nm). Reflectivity rescaled on the right unit scale. Localised shifted peak position plot vs 1st Bragg mode and super Tamm mode for sphere-based hybrid nano cavities made with different DBRs (b) 440 nm, (c) 480 nm and (d) 520 nm.

In the next section we are going to see how the experiments matched this theoretical prediction.

## 6.2 EXPERIMENTAL RESULTS

### 6.2.1 FABRICATION PROCESS

To study this second physical regime we used both vertical and horizontal dipoles as well. We used another Lumogen family dye, this time we used the Lumogen Yellow F, which displays its emission peak in the first Bragg mode, making this a region of interest for this study, Figure 69 (a). Similarly, to the work presented in the previous chapter, we used the Zeonex polymer as the hosting agent for the dye. For the horizontal orientation we chose the emitting polymer F8TBT Figure 69 (b). The experimental procedure is the same of the previous chapter. In Figure 69 (c) we have the experimental reflection spectrum for the DBR used in this second study, which

shows the clear spectral overlap between the 1st Bragg mode and the emission of both Lumogen Yellow F and F8BT.

The emitting layer has been deposited onto the DBR surface via spin coating after a solvent and plasma cleaning. We kept the active layer thickness to 10 nm. We carried out a systematic study by changing the gold nano-particles diameters (100, 250, 400, and 500 nm) and looking at the optical properties of each quantum emitter in those systems.

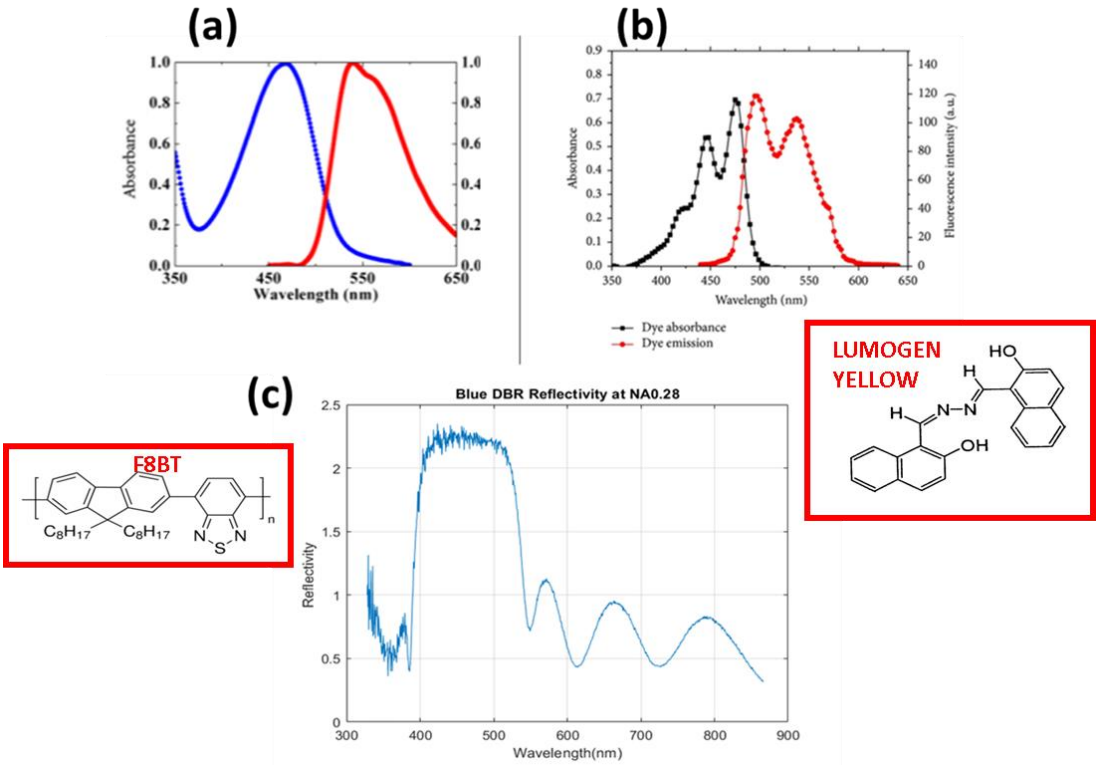


Figure 69 Absorption and emission spectra of (a) F8BT and (c) Lumogen Yellow F. (c) Reflection spectrum for the DBR used in the experimental section.

### 6.2.2 EMISSION DIAGRAMS

In Figure 70, we have the emission diagram recorded from the cavity made with a 100 nm diameter particle using the Lumogen Yellow F as emitter, therefore the dipole orientation is vertical. In Figure 70 (a) we have the emission diagram recorded from the cavity, from the reference (b) we can observe how the nanocavity (a) enables the emission at angles where otherwise is not allowed. The emission coupling is directional, indeed most of the emitted light is into the cone ±30°, Figure 70 (f). Another important feature it is tight spectral localization around 510 nm. The 1st Bragg mode is increasing the field confinement and therefore the intensity of the excitation.

On the DBR reference instead we have emission only at angles close or higher than 60 degrees. This result in line with what you showed in the previous chapter for DBR alone, albeit spectrally shifted to correspond to the new DBR optical response. As consequence of this, the enhancement factor is highly localised spectrally around 500 nm and spread over a span of 40 degrees. Comparing the emission profile at 0 degrees Figure 70 (e), we see how the cavity introduces a blue-shift of 30 nm in the emission spectrum. The results obtained are compared with the calculation in Figure 70 (c-d) cavity and reference. To make the theoretical figures directly comparable with the experiments one, we corrected the far field images by interpolating the horizontal lines with the experimental emission spectrum of the Lumogen Yellow F normalised to 1. Simulation and experiments are in good agreement when we compare the reference (b-d): both figures have an emission peak around 510 nm and the emission is directed at angles higher than 40 degrees. However, theory and experiments are in partial agreement when we compare the response of the cavity (a-c): in the simulations there is little signal at small angles. This discrepancy can be explained with a more random orientation distributions of the dipoles into the cavity and with the relative position of the dipole with the cavity. This was explained in section 5.3.2.1.

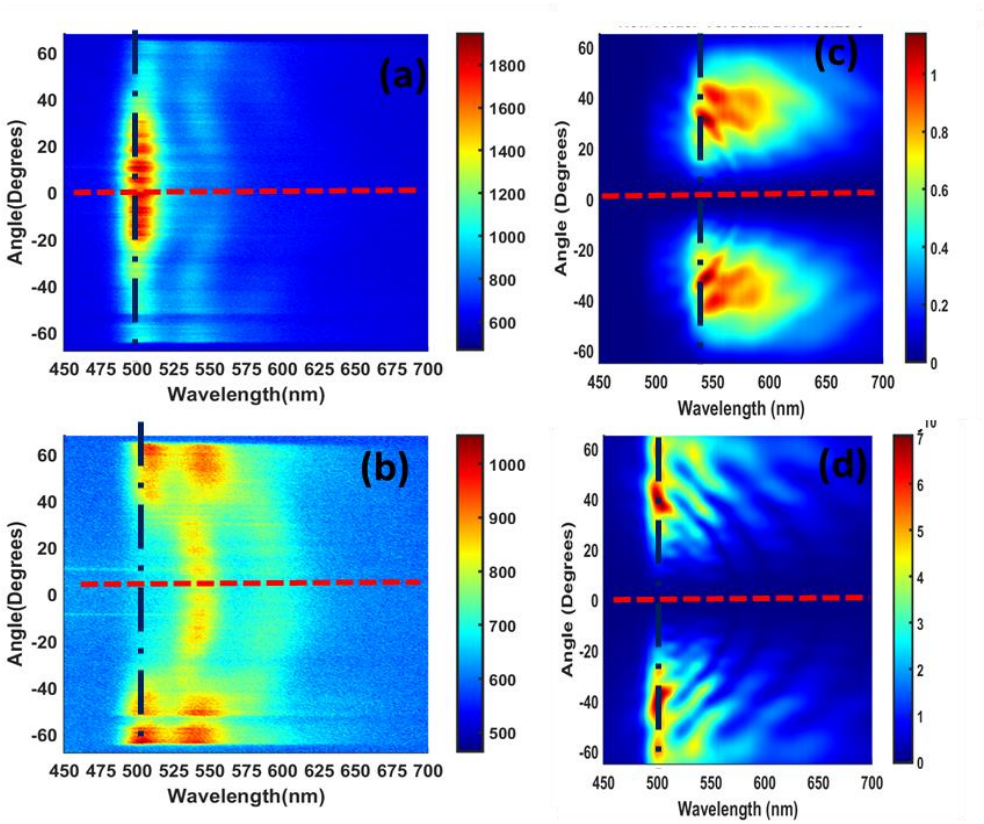

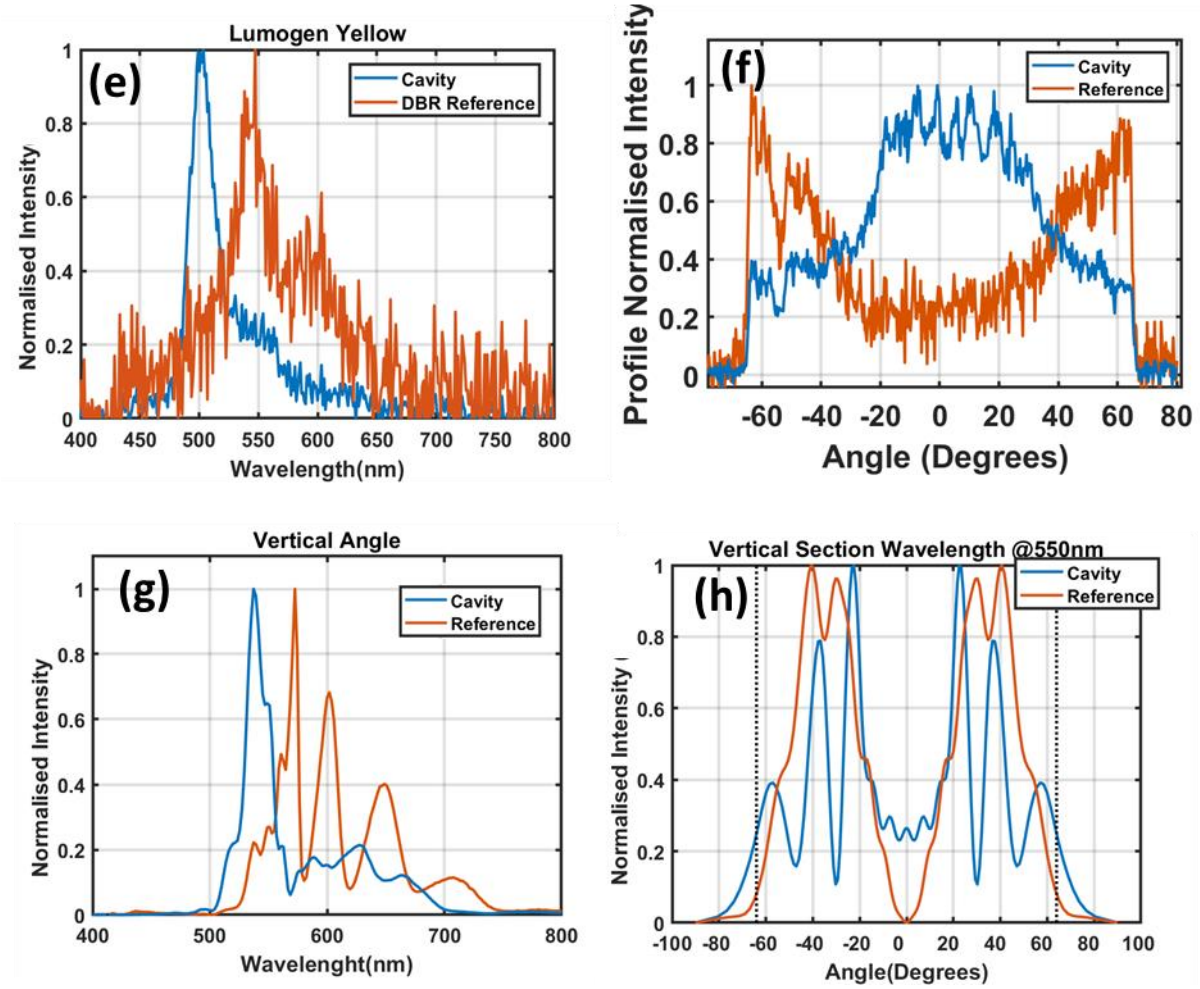


Figure 70 (a) Cavity experimental emission diagram (particle size 250nm), (b) reference on DBR k-space emission, (c) simulated cavity far-field, (d) simulated reference far-field, spectral profile corrected with Lumogen Yellow emission spectrum. (e) Experimental 0 angle section (figure a -b red line). (f) Experimental peak wavelength section (figure a – b black line). (g) Simulated 0 angle section (figure c-d red line). (h) Experimental peak wavelength section (figure c-d black line).

We repeated the experiment with the horizontal dipole. We used the emitting polymer F8BT to replicate the experiments. In Figure 71 we have the k-space emission from the nanocavity (particle diameter 250nm)(a), DBR reference (b). The reference on DBR (b) shows the light being emitted on the local maximum out of the 1st Bragg mode. In terms of angles we observe two main lobes at high angles (above 50°) and parabola at small angles. The nano-cavity (a-f) enable the polymer emission mostly around the 1$^{st}$ Bragg mode with a high angle localization in the region ±20 degrees. This is the strongest directionality observed in this work. The emission diagram at 0 degrees shows a 20 nm blue shift. The reference image (d) is particularly close to the experimental one (b). The agreement between theory and experiments is particularly evident when we compare the experimental angle section (f) with the predicted one (h).

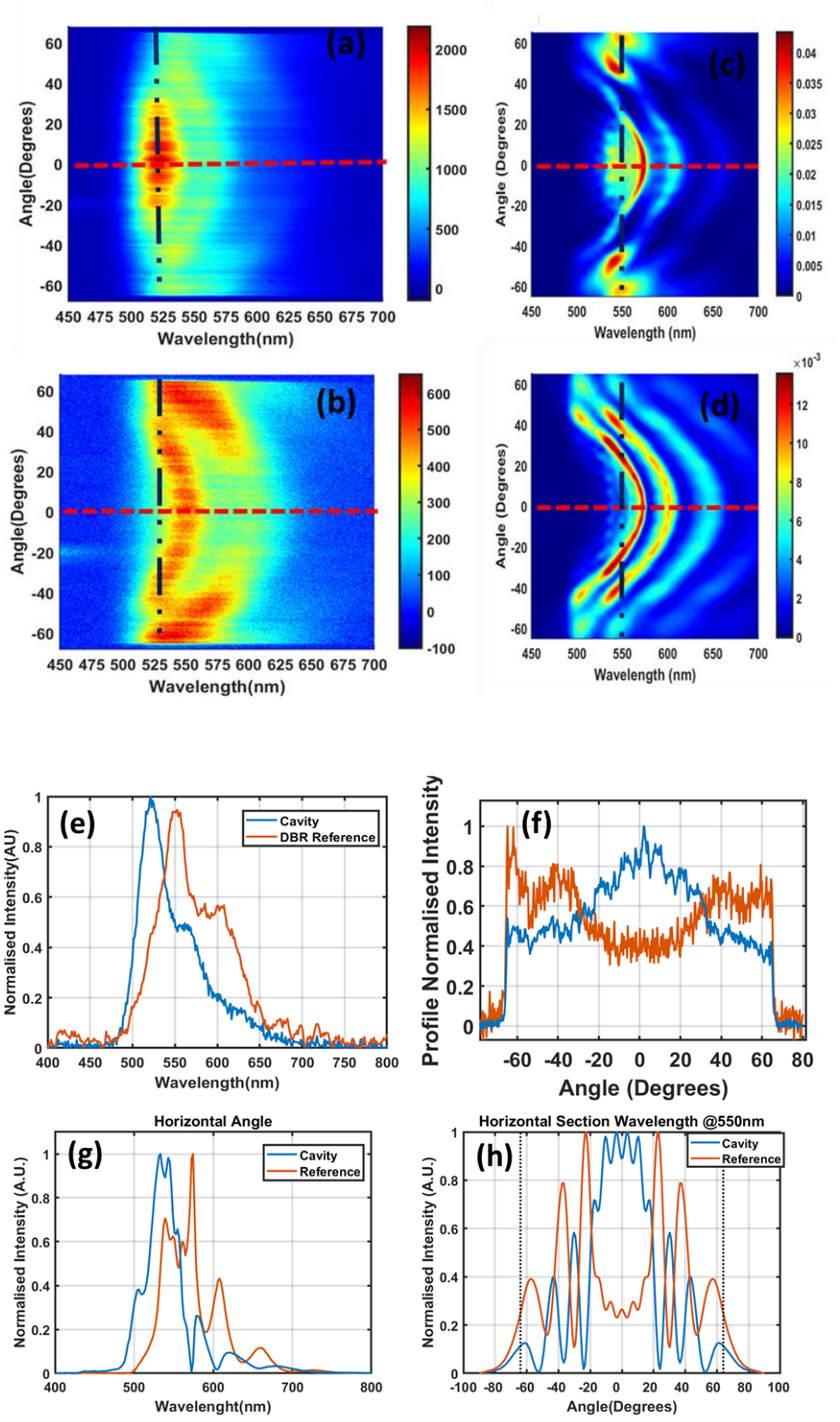


Figure 71 (a) Cavity experimental emission diagram, (b) reference on DBR k-space emission, (c) simulated Cavity Far field, (d) simulated reference Far field ,spectral profile corrected with F8BT emission spectrum. (e) Experimental 0 angle section (figure a -b red line). (f) Experimental peak wavelength section (figure a – b black line). (g) Simulated 0 angle section (figure c-d red line). (h) Experimental peak wavelength section (figure c-d black line).

Repeating the procedure presented in Figure 68 (a) with the experimental data for different particle sizes, we can again plot the position of the peak emission wavelength for each nano-cavity, compared with the experimentally determined 1st Bragg mode spectral position, Figure 75. For the Lumogen Yellow in those nano-cavities, the emission peak is shifted to a wavelength of about 505 nm, however, no spectral shift is observed as the nano particle size increases. For F8BT on the other hand, Figure 72, we can clearly observe peak shifting towards the blue as the nano particle size increases, in agreement with the simulations in Figure 68.

This is the proof that is possible to excite an intermediate Tamm state in between the 1st Bragg mode and the super Tamm.

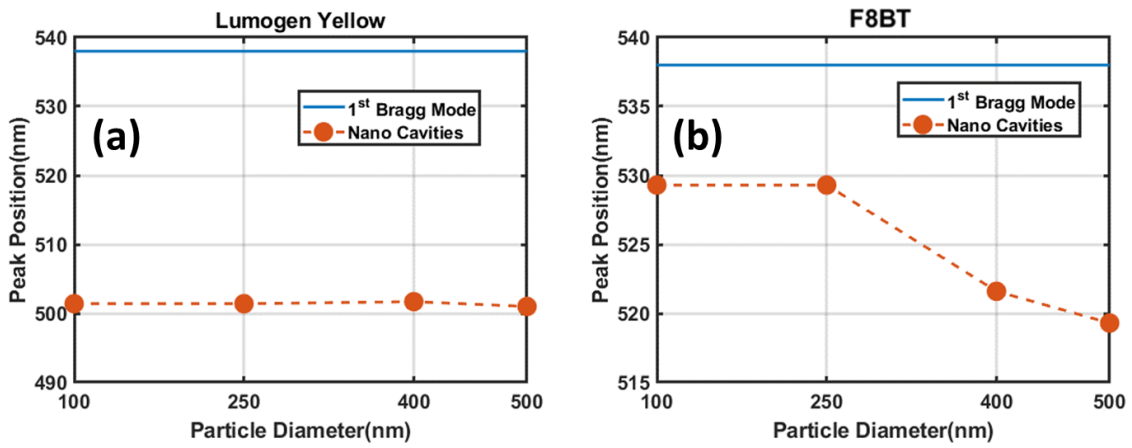


Figure 72 Experimentally observed peak position of the localised mode compared to the 1st Bragg mode. (a) Lumogen Yellow, (b) F8BT.

We performed another cycle of simulations in which the nano-spheres are replaced with 10 nm thick nano-disks with diameter equivalent to the nano spheres. The sphere offers small contact point and a curvature compared to an infinite film. With this study we wanted to explore the transition dynamics from a traditional super -Tamm mode (infinite film) to a localised one (sphere). We added two extra disks with the diameter of 1000 nm and 3000 nm. We summarised the results in Figure 73. As we can see, at parity of size, the nano-disk do not exhibit any noticeable shift from the Bragg mode. The two larger disk sizes have a larger shift. The convergence to the super Tamm mode is much slower with the nano disks.

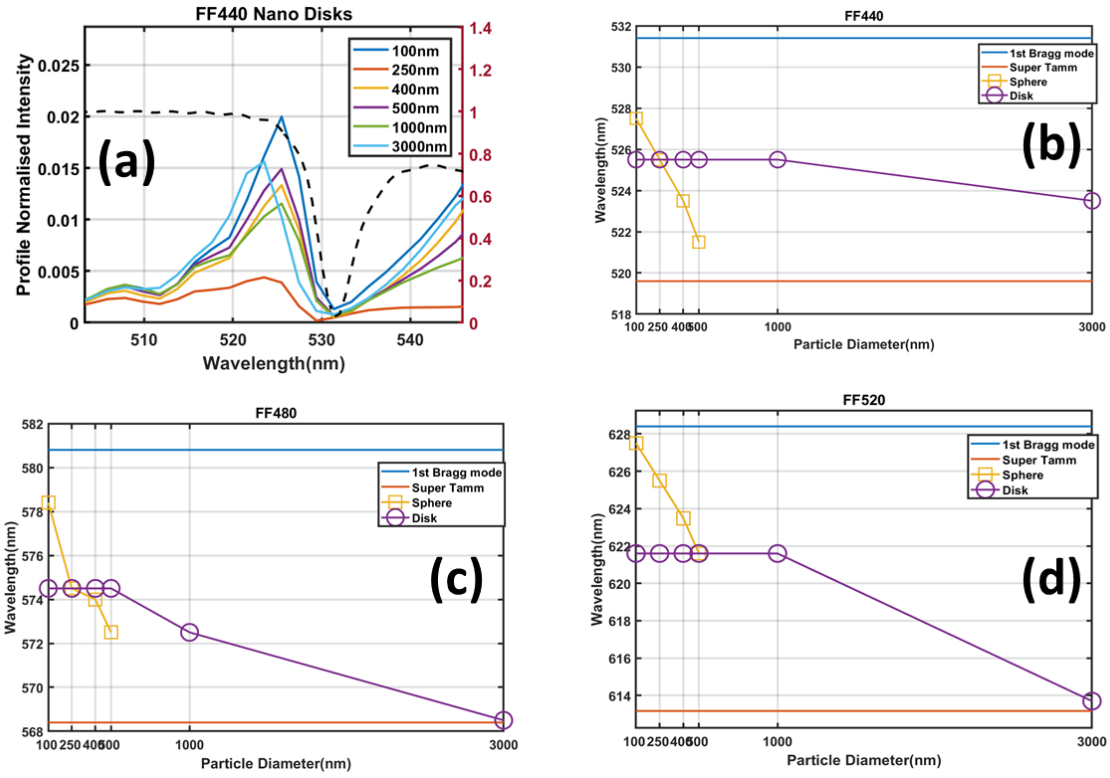


Figure 73 Example of Far field profile recorded for different nano cavities compared with calculated the DBR reflection spectrum. Zoomed around the 1st Bragg mode wavelength (531.4nm). Reflectivity rescaled on the right unit scale. Localised shifted peak position plot vs 1st Bragg mode and super Tamm mode for sphere-based hybrid nano cavities made with different DBRs (b) 440 nm, (c) 480 nm and (d) 520 nm. The Purple line represents nano cavities made using gold nano- disks instead of nano spheres.

## 6.3 CONCLUSIONS

In this chapter we studied both experimentally and via FDTD calculations the optical properties of a hybrid dielectric metal nano cavity in a first Bragg mode confinement.

This choice was justified by merging the high-quality factor Q given by the DBR supported by the relatively small modal volume into the Bragg mode with the even smaller Volume mode V given by the plasmonic nano particles to get a high Purcell factor. The extinction of a gold nano sphere lays into the visible and the position of the first Bragg mode can be accurately tuned to match it. The FDTD calculation show a strong far field localisation both spectral around the 1st Bragg mode and in terms of angle, particularly interesting are the far field maps recorded with the horizontal orientation since the localisation is high. The novelty of this work is to have used emitting polymers instead of epitaxially grown quantum dots to achieve the horizontal dipole [70]. The emitters experimentally used are, Lumogen Yellow F for the averaged vertical orientation and F8BT for the horizontal one. Both emitters have the emission peak roughly around 550 nm, the DBR 1st Bragg mode lays around that wavelength. Both orientations

achieve and high spectral localisation around the first Bragg mode, but in terms of angles we see a much larger difference. The Lumogen Yellow (Vertical) has an emission cone as wide as 30 degrees, instead the F8BT (horizontal) has an emission cone roughly 20 degrees. This is the smallest angle cone achieved with all the systems. With FDTD near to far field projections we predicted, for Au nano spheres based nano cavities, the existence of localised modes in between the 1$^{st}$ Bragg mode wavelength and the Super Tamm wavelength. Smaller spheres exhibit this mode closer to the 1$^{st}$ Bragg mode, increasing the particle diameter the wavelength of this mode quickly converges to the super Tamm wavelength. We remember that Tamm plasmon are usually observed with highly horizontal emitters such as epitaxial quantum dots grown inside the reflector and with more planar nano particle geometries such as micro-disks[70]. We repeated the calculations with nano disks having 10 nm thickness and the same diameter of the nano spheres. The results were totally different since no shift was observed increasing the disk size, unless using larger micro disks with a diameter of one and three microns. We need to specify that despite increasing the size this much a much more modest shift was observed compared with the nano spheres.

# Chapter 7 Conclusions and Future Work

Throughout this thesis, the unique optical properties of hybrid plasmonic/photonics nano gaps have been studied. Plasmonic and photonics have been combined to create hybrid nanogaps made by distributed Bragg reflector DBR and gold nano spheres. Organic dyes embedded in thin films and emitting polymers have been used as fluorescent probes. The first were used when the dipole orientation was required to be vertical, instead emitting polymers were used when it was required to be horizontal. These hybrid nano cavities have been used both as emitting antennas, as well as super Tamm modes generator.

The nano gaps were fabricated by spin coating 10 nm of emitting material, either a dye doped film or an emitting polymer film, onto a DBR grown on Silicon. The last step was to deposit the gold nano spheres onto the emitting surface. In both applications 100, 250, 400 and 500 nm diameter gold nanosphere have been used. The gold nanoparticles were used due to their ability to support localised surface plasmons resonances (LSPR). The enhanced local fields surrounding the particle can modify the local density of states (LDOS) of an emitter when placed in proximity (1-10 nm) to the particle. DBR were chosen instead of metallic mirrors since of their almost perfect reflectivity and negligible optical loss within the stopband.

The first application examined was the directivity of the emission. Because of the Fermi golden rule, the dipole needs to be parallel to the cavity dipole moment to get the largest coupling possible. The directivity was studied with the technique of k-space imaging using an air objective with a very lager numerical aperture of 0.9. This numbers equivale to the ability to reach a light cone of +/- 64 degrees to the normal of the surface. The light emission is re-directed by using gold nano particles toward directions where the reflector on its own cannot reach. These hybrid nanocavities showed some capabilities in the emission control. Indeed, both the emission intensity and directivity depend upon the particle size. The 500nm particle showed the tightest emission cone enhancement of 20 degrees. The time dynamic of the emission process was studied as well confirming the coupling between emitters and nano cavity. Showing an effective lifetime reduction of a factor six when the emitter is probed inside the cavity. This proves that the cavity was effectively boosting the excitation rate of the fluorophore since the excitation rate is the reciprocal of the lifetime. FDTD calculations have been made to help modelling the systems. The calculations were performed in an ideal situation in which the emitting dipole is unique, and it is placed at the exact centre of symmetry pf the nano cavity halfway exactly between the DBR surface and the nano antenna. These calculations

modelled the k-space imaging by projecting the near field recorded above the nano antenna into the far field. The calculations agree with the experiment to such an extent. Indeed, some of the light is re directed toward the direction orthogonal to the surface like in the experimental case. FDTD has been used to model the influence of the nano particle size, DBR spectral band position and dipole orientation.

The next step to study the system would be to use more complicate geometries to control the emission pattern. In this work, only nano spheres have been used, due to the limited nano fabrication capabilities. Other geometries of interest would be nano rods and pointy objects such as nano pyramids. Nano rods have two LSPRs modes, one parallel and one orthogonal to the main axis. It is possible to excite one of the two modes by properly tuning the polarization of the excitation. This property of the rods can be used to manipulate the optical response of the nano antenna by changing with the polarization of the impinging light. A simple modification like this, it could improve the hybrid nano gaps by making them active devices. Nano rods will add an extra degree of control to the hybrid nano antennas, the emission can be tuned by changing the excitation polarization. The idea behind such a device is to control the intensity of the emission as well as the direction by controlling the polarization of the exciting light.

The second use of hybrid nano cavities done in this thesis is using them as model study for localised super Tamm states. For this second experiment, the DBR has been used as a 1-d photonic crystal rather than a reflector. Indeed, the minima in the DBR reflection spectra represent modes in which the light can travel through the stack without being reflected. The first minimum on the red shifted side of the DBR reflection band is called $1^{st}$ Bragg mode.

In this work the first Bragg mode is coupled with the LSPR of the nano sphere. The emitting dipole needs to be oriented orthogonal to the cavity dipole moment, namely parallel to the interface between DBR and nano particle. FDTD calculation helped modelling the influence of the $1^{st}$ Bragg mode position and the particle size into the system as well as they have been used to determine the Super Tamm position mode position as well. From these calculations as well, it has been observed a new mode spectrally placed in between the $1^{st}$ Bragg mode and the super Tamm one. This new mode has been named as isolated Super Tamm mode, since it is excited thank to an isolated nanosphere. The new mode blue shifts by increasing the particle size asymptotically converging toward the suer Tamm wavelength.

The same calculation was performed with nano disks, same geometry used in [70], however the presence of this mode was barely noticeable until increasing the disk diameter to 2

micrometres. Some control calculations were performed with nano spheres but using the other dipole orientation and as expect no mode was observed.

The novelty of this work is to find an electromagnetic mode with intermediate nature between Super Tamm plasmon and the 1st Bragg mode. This new type of Super Tamm mode is much closer spectrally to the Bragg mode compared with the Tamm mode. To excite this mode, an emitting polymer was used, and this represents another element of novelty since other previous works on Super Tamm modes have used epitaxially grown quantum dots.

Epitaxial quantum dots allow a better control of the dipole orientation since of their bottom-up fabrication process. The experiments need to be repeated with such an emitter to increase the efficiency of the mode excitation. The last parameter to change is the geometry of the nano antenna. This work was performed using nano spheres only, therefore a new set of experiments using different geometries is needed to figure out the real nature of this electromagnetic mode. Another important point to explore is the time dynamics of this new mode excitation process.

# REFERENCES


[1] Kittel, C. (2004). Introduction to solid state physics (8th ed.). John Wiley & Sons, NYC.

[2] S. Roy, C. K. Dixit, R. Woolley, R. O. Kennedy, and C. Mcdonagh, “Synthesis and Characterization of a Noble Metal Enhanced Optical Nanohybrid ( NEON ): A High Brightness Detection Platform Based on a Dye-Doped Silica Nanoparticle,” vol. 664, 2012.

[3] X. Zhou et al., “Two-Color Single Hybrid Plasmonic Nanoemitters with Real Time Switchable Dominant Emission Wavelength,” Nano Lett. 2015, 15, 11, 7458–7466, October 5, 2015

[4] X. Zhou et al., “Polarization-dependent fluorescence from an anisotropic gold/polymer hybrid nano-emitter,” Appl. Phys. Lett., vol. 104, no. 2, pp. 1–5, 2014.

[5] K. Leong, M. T. Zin, H. Ma, M. Sarikaya, F. Huang, and A. K. Jen, “Surface Plasmon Enhanced Fluorescence of Cationic Conjugated Polymer on Periodic,” vol. 2, no. 11, pp. 26–28, 2010.

[6] A. Furube, L. Du, K. Hara, R. Katoh, and M. Tachiya, “Ultrafast Plasmon-Induced Electron Transfer from Gold Nanodots into TiO 2 Nanoparticles,” pp. 14852–14853, 2007.

[7] H. Cong, R. Toftegaard, J. Arnbjerg, and P. R. Ogilby, “Silica-Coated Gold Nanorods with a Gold Overcoat : Controlling Optical Properties by Controlling the Dimensions of a Gold - Silica - Gold Layered Nanoparticle,” vol. 26, no. 20, pp. 4188–4195, 2010.

[8] R. Quidant and N. F. Van Hulst, “Dot Coupled to a Nanoantenna,” vol. 329, no. August, pp. 930–934, 2010.

[9] O. Kulakovich et al., “Enhanced Luminescence of CdSe Quantum Dots on Gold Colloids,” 2002.

[10] J. Kim and B. Mathieu, “Plasmon-Induced Modification of Fluorescent Thin Film Emission Nearby Gold Nanoparticle Monolayers,” vol. 26, no. 20, pp. 8842–8849, 2010.

[11] T. Sen and A. Patra, “Recent Advances in Energy Transfer Processes in Gold Nanoparticle Based Assemblies ,2012.

[12] A. Kinkhabwala, Z. Yu, S. Fan, Y. Avlasevich, K. Müllen, and W. E. Moerner, “Large single-

molecule fluorescence enhancements produced by a bowtie nanoantenna," Nat. Photonics, vol. 3, no. 11, pp. 654–657, 2009.

[13] W. P. Hall, S. N. Ngatia, and R. P. Van Duyne, "LSPR Biosensor Signal Enhancement Using Nanoparticle - Antibody Conjugates," pp. 1410–1414, 2011.

[14] J. B. Schneider, "Near-to-Far-Field Transformation," Underst. Finite-Difference Time-Domain Method, pp. 351–376, 2010.

[15] H. Dong et al., "A nanostructure-based counter electrode for dye-sensitized solar cells by assembly of silver nanoparticles," Org. Electron., vol. 15, no. 7, pp. 1641–1649, 2014.

[16] G. Rana et al., "Quadrupole-Quadrupole Interactions to Control Plasmon-Induced Transparency," Phys. Rev. Appl., vol. 9, no. 6, p. 64015, 2018.

[17] Y. Zhang, T. Q. Jia, S. A. Zhang, D. H. Feng, and Z. Z. Xu, "Dipole, quadrupole and octupole plasmon resonance modes in non-concentric nanocrescent/nanodisk structure: local field enhancement in the visible and near infrared regions," Opt. Express, vol. 20, no. 3, p. 2924, 2012.

[18] D. Gerard and S. K. Gray, "Aluminium plasmonics," J. Phys. D. Appl. Phys., vol. 48, no. 18, p. 184001, 2015.

[19] A. S. Baburin, A. M. Merzlikin, A. V. Baryshev, I. A. Ryzhikov, Y. V. Panfilov, and I. A. Rodionov, "Silver-based plasmonics: golden material platform and application challenges [Invited]," Opt. Mater. Express, vol. 9, no. 2, p. 611, 2019.

[20] V. Amendola, R. Pilot, M. Frasconi, O. M. Maragò, and M. A. Iatì, "Surface plasmon resonance in gold nanoparticles: A review," J. Phys. Condens. Matter, vol. 29, no. 20, 2017.

[21] F. Ehrenhaft and L. Lorenz, "Der physik. 1.," 1908.

[22] R. Spurr, J. Wang, J. Zeng, and M. I. Mishchenko, "Linearized T-matrix and Mie scattering computations," J. Quant. Spectrosc. Radiat. Transf., vol. 113, no. 6, pp. 425–439, 2012.

[23] M. Le Bellac and J. Lévy-Leblond, "Galilean Electromagnetism," Nuovo Cim. B, vol. 14, no. 2, pp. 217–234, 1973.

[24] P. Review and I. The, "Electronic polarizability," vol. 31, no. 6, pp. 3486–3495, 1985.

[25] K. L. Kelly, E. Coronado, L. L. Zhao, and G. C. Schatz, “Feature article,” pp. 668–677, 2003.

[26] X. Fan, W. Zheng, and D. J. Singh, “Light scattering and surface plasmons on small spherical particles,” Light Sci. Appl., vol. 3, no. November 2013, pp. 1–14, 2014.

[27] T. Information, November, 1997. http://www2.basf.us/additives/pdfs/p3201e

[28] T. V Teperik and V. V Popov, “Radiative decay of plasmons in a metallic nanoshell,” pp. 1–7, 2004.

[29] C. Dahmen, B. Schmidt, and G. Von Plessen, “Radiation Damping in Metal Nanoparticle Pairs,” 2007.

[30] Hao, E., Schatz, G.C. & Hupp, J.T. Synthesis and Optical Properties of Anisotropic Metal Nanoparticles. Journal of Fluorescence 14, 331–341 (2004).

[31] J. Lerm et al., “Size Dependence of the Surface Plasmon Resonance,” pp. 2922–2928, 2010.

[32] Aleksandar D. Rakić, Aleksandra B. Djurišić, Jovan M. Elazar, and Marian L. Majewski, “Optical properties of metallic film for vertical cavities optoelectronics device”, Applied optics, vol 37 , issue 22, 5271-5283, (1998)

[33] M. M. Alvarez, J. T. Khoury, T. G. Schaaff, M. N. Shafigullin, I. Vezmar, and R. L. Whetten, “Optical Absorption Spectra of Nanocrystal Gold Molecules,” vol. 5647, no. 96, pp. 3706–3712, 1997.

[34] C. Sönnichsen, T. Franzl, T. Wilk, G. Von Plessen, and J. Feldmann, “Drastic Reduction of Plasmon Damping in Gold Nanorods,” Phys. Rev. Lett. 88, 077402 – Published 31 January 2002.

[35] M. Meier and A. Wokaun, “Enhanced fields on large metal particles: dynamic,” vol. 8, no. 11, pp. 581–583, 1983.

[36] C. F. Bohren and D. R. Huffman, Absorption and scattering of light by small particles. Wiley-Interscience Publication .JOHN WILEY & SONS., 2007.

[37] Y. S. Kim, P. T. Leung, and T. F. George, “Classical decay rates for molecules in the presence of a spherical surface: A complete treatment,” Surf. Sci., vol. 195, no. 1–2, pp. 1–14, 1988.

[38] G. Colas des Francs et al., “Fluorescence relaxation in the near-field of a mesoscopic

metallic particle: distance dependence and role of plasmon modes.," Opt. Express, vol. 16, no. 22, pp. 17654–17666, 2008.

[39] A. V Zayats and I. I. Smolyaninov, "Near-field photonics: surface plasmon polaritons and localised surface plasmons," J. Opt. A Pure Appl. Opt., vol. 5, pp. S16–S50, 2003.

[40] A. V. Zayats, I. I. Smolyaninov, and A. a. Maradudin, "Nano-optics of surface plasmon polaritons," Phys. Rep., vol. 408, pp. 131–314, 2005.

[41] O. Benson, "Assembly of hybrid photonic architectures from nanophotonic constituents," Nature, vol. 480, no. 7376, pp. 193–199, 2011.

[42] Plalla Perez Gonzalez, "Optical properties and high-frequency electron transport in plasmonic cavities," . https://cfm.ehu.es/nanophotonics/THESIS/Thesis_Olalla_Perez_Nov_2011.pdf

[43] "E. Fermi. Nuclear Physics: course notes complied by J. Orear, A. H. Rosenfeld, and R. A. Schluter. The University of Chicago Press: London. 1974. ISBN 0226243656.," p. 1974, 1974.

[44] R. I. Ghauharali, J. W. Hofstraat, and G. J. Brakenhoff, "Fluorescence photobleaching-based shading correction for fluorescence microscopy," J. Microsc., vol. 192, no. 2, pp. 99–113, 1998.

[45] E. Günther, A. Klauß, M. Toro-Nahuelpan, D. Schüler, C. Hille, and D. Faivre, "The in vivo mechanics of the magnetotactic backbone as revealed by correlative FLIM-FRET and STED microscopy," Sci. Rep., vol. 9, no. 1, pp. 1–9, 2019.

[46] L. Song, E. J. Hennink, I. T. Young, and H. J. Tanke, "Photobleaching kinetics of fluorescein in quantitative fluorescence microscopy," Biophys. J., vol. 68, no. 6, pp. 2588–2600, 1995.

[47] R. I. Ghauharali and G. J. Brakenhoff, "Fluorescence photobleaching-based image standardization for fluorescence microscopy," J. Microsc., vol. 198, no. 2, pp. 88–100, 2000.

[48] "E. C. Le Ru and P. G. Etchegoin. Principles of surface-enhanced Raman spectroscopy and related plasmonic effects. Elsevier: Oxford. 2009. ISBN 9780444527790.," p. 2009, 2009.

[49] P. Anger, P. Bharadwaj, and L. Novotny, "Enhancement and quenching of single-

molecule fluorescence," Phys. Rev. Lett., vol. 96, no. 11, pp. 3–6, 2006.

[50] T. Härtling, P. Reichenbach, and L. M. Eng, "Near-field coupling of a single fluorescent molecule and a spherical gold nanoparticle," Opt. Express, vol. 15, no. 20, pp. 12806–12817, 2007.

[51] "L. Novotny and B. Hecht. Principles of nano-optics. Cambridge: New York. 2012. ISBN 9781107005464.," p. 2012, 2012.

[52] "J. R. Lakowicz. Topics in fluorescence spectroscopy: volum 4 probe design and chemical sensing. Plenum: New York. 1994. ISBN 0306447843.," p. 1994, 1994.

[53] G. Colas Des Francs, S. Derom, R. Vincent, A. Bouhelier, and A. Dereux, "Mie plasmons: Modes volumes, quality factors, and coupling strengths (Purcell factor) to a dipolar emitter," Int. J. Opt., vol. 2012, 2012.

[54] J. J. Greffet, M. Laroche, and F. Marquier, "Impedance of a nanoantenna and a single quantum emitter," Phys. Rev. Lett., vol. 105, no. 11, pp. 1–4, 2010.

[55] R. Chikkaraddy et al., "Single-molecule strong coupling at room temperature in plasmonic nanocavities," Nature, pp. 1–4, 2016.

[56] S. Mubeen et al., "Plasmonic properties of gold nanoparticles separated from a gold mirror by an ultrathin oxide," Nano Lett., vol. 12, no. 4, pp. 2088–2094, 2012.

[57] A. P. Edwards and A. M. Adawi, "Plasmonic nanogaps for broadband and large spontaneous emission rate enhancement," J. Appl. Phys., vol. 115, no. 5, 2014.

[58] C. J. R. Sheppard, "Approximate calculation of the reflection coefficient from a stratified medium," Pure Appl. Opt. J. Eur. Opt. Soc. Part A, vol. 4, no. 5, pp. 665–669, 1995.

[59] G. Lee, D. A. Scripka, B. Wagner, N. N. Thadhani, Z. Kang, and C. J. Summers, "Design and fabrication of distributed Bragg reflector multilayers for dynamic pressure sensing," Opt. Express, vol. 25, no. 22, p. 27067, 2017.

[60] I. H. Malitson, "Interspecimen Comparison of the Refractive Index of Fused Silica, J. Opt. Soc. Am., vol. 55, no. 10, p. 1205, 1965. https://www.osapublishing.org/josa/abstract.cfm?uri=josa-55-10-1205

[61] J. R. Devore, "Refractive Indices of Rutile and Sphalerite," J. Opt. Soc. Am., vol. 41, no. 6, p. 416, 1951.

[62] L. Gao, F. Lemarchand, and M. Lequime, “Exploitation of multiple incidences spectrometric measurements for thin film reverse engineering,” Opt. Express, vol. 20, no. 14, pp. 15734–51, 2012.

[63] P. Lova et al., “Polymer distributed bragg reflectors for vapor sensing,” ACS Photonics, vol. 2, no. 4, pp. 537–543, 2015.

[64] B. Osting, “Bragg structure and the first spectral gap,” Appl. Math. Lett., vol. 25, no. 11, pp. 1926–1930, 2012.

[65] M. Kaliteevski et al., “Tamm plasmon-polaritons: Possible electromagnetic states at the interface of a metal and a dielectric Bragg mirror,” Phys. Rev. B - Condens. Matter Mater. Phys., vol. 76, no. 16, pp. 1–5, 2007.

[66] A. V. Kavokin, I. A. Shelykh, and G. Malpuech, “Lossless interface modes at the boundary between two periodic dielectric structures,” Phys. Rev. B - Condens. Matter Mater. Phys., vol. 72, no. 23, pp. 1–4, 2005.

[67] R. Badugu and J. R. Lakowicz, “Tamm state-coupled emission: Effect of probe location and emission wavelength,” J. Phys. Chem. C, vol. 118, no. 37, pp. 21558–21571, 2014.

[68] C. Symonds et al., “Con fi ned Tamm Plasmon Lasers,” 2013.

[69] K. Leo, V. Lyssenko, and S. Hofmann, “Lasing of Tamm states in highly efficient organic devices based on small-molecule organic semiconductors,” Faraday Discuss., vol. 174, no. i, pp. 183–201, 2014.

[70] C. Symonds et al., “High quality factor confined Tamm modes,” Sci. Rep., vol. 7, no. 1, p. 3859, 2017.

[71] Kane Yee, “Numerical solution of initial boundary value problems involving maxwell’s equations in isotropic media,” IEEE Trans. Antennas Propag., vol. 14, no. 3, pp. 302–307, 1966.

[72] M. Salmasi, M. E. Potter, and M. Okoniewski, “Implementation of General Dispersive Anisotropic Materials in Lebedev FDTD,” IEEE Trans. Antennas Propag., vol. 66, no. 12, pp. 7171–7179, 2018.

[73] M. H. Chowdhury, K. Ray, and J. R. Lakowicz, “Use of aluminum films as substrates for enhanced fluorescence in the ultraviolet-blue spectral region.,” Proc. SPIE--the Int. Soc.

Opt. Eng., vol. 6869, no. 68690E, p. nihpa120419, 2008.

[74] P. Das, A. Kedia, P. S. Kumar, N. Large, and T. K. Chini, “Local Electron Beam Excitation and Substrate Effect on the Plasmonic Response of Single Gold Nanostars,” J. Phys. C0hem. C 2015, 119, 32, 18537–18545

[75] S. Xiao and R. Vahldieck, “An Efficient 2-D FDTD Algorithm Using Real Variables,” IEEE Microw. Guid. Wave Lett., vol. 3, no. 5, pp. 127–129, 1993.

[76] K. H. Dridi, J. S. Hesthaven, and A. Ditkowski, “Staircase-free finite-difference time-domain formulation for general materials in complex geometries,” IEEE Trans. Antennas Propag., vol. 49, no. 5, pp. 749–756, 2001.

[77] “Radar Cross section of three dimensional scatterers - Allen Taflove.pdf.” .

[78] “Numerical solution of steady-state electromagnetic scattering problems using the time-dependent Maxwell’s equations," IEEE Trans. Microwave Theory & Technique.” .

[79] A. T. and K. Umashankar, “A hybrid moment method / finite-difference time-domain approach to electromagnetic coupling and aperture penetration into complex geometries.” .

[80] R. M. Wenhua Yu, “A Conformal Finite Difference Time Domain Technique for Modeling Curved Dielectric Surfaces,” IEEE Microw. Wirel. COMPONENTS Lett., vol. 11, no. 1, pp. 25–26, 2001.

[81] A. Farjadpour et al., “Improving accuracy by subpixel smoothing in the finite-difference time domain,” Opt. Lett., vol. 31, no. 20, p. 2972, 2006.

[82] V. Raulot, P. Gérard, B. Serio, M. Flury, and P. Meyrueis, “Comparison of the behavior of a subwavelength diffractive lens in TE and TM polarization allowing some nonstandard functions,” Opt. Lett., vol. 36, no. 7, p. 1194, 2011.

[83] A. C. Lesina, A. Vaccari, P. Berini, and L. Ramunno, “On the convergence and accuracy of the FDTD method for nanoplasmonics,” Opt. Express, vol. 23, no. 8, p. 10481, 2015.

[84] Bringer, J.-P., “A Perfectly Matched Layer for the Absorption of Electromagnetic Waves,” J. Comput. Phys., vol. 114, pp. 185–200, 1994.

[85] B. Rai, “Modeling of a Photonic Crystal Waveguide Modes with the FDTD Method ”. Master dissertation found online:

https://scholarworks.wmich.edu/cgi/viewcontent.cgi?article=1061&context=dissertations

[86] Jia Li†, Alexey V. Krasavin, Linden Webster, Paulina Segovia‡, Anatoly V. Zayats & David Richardson , Scientific Reports volume 6, Article number: 21349 (2016)

[87] A. O. Hamza, "Controlling Förster Resonance Energy Transfer Using Plasmonic Nano-gaps".

[88] A. B. Vasista, D. K. Sharma, and G. V. P. Kumar, "Fourier Plane Optical Microscopy and Spectroscopy," Digit. Encycl. Appl. Phys., pp. 1–14, 2019.

[89] S. Bernet, A. Jesacher, S. Fürhapter, C. Maurer, and M. Ritsch-Marte, "Quantitative imaging of complex samples by spiral phase contrast microscopy.," Opt. Express, vol. 14, no. 9, pp. 3792–3805, 2006.

[90] C. I. Osorio, A. Mohtashami, and a F. Koenderink, "K-space polarimetry of bullseye plasmon antennas.," Sci. Rep., vol. 5, p. 9966, 2015.

[91] Y. Zhang, Y. Chen, J. Yu, and D. JS Birch, "A surface plasmon enhanced FLIM-FRET imaging approach based on Au nanoparticles," Med. Devices Diagnostic Eng., vol. 2, no. 2, pp. 78–82, 2017.

[92] K. Suhling et al., "Fluorescence lifetime imaging," Handb. Photonics Biomed. Eng., vol. 330, pp. 353–405, 2017.

[93] W. Becker and A. Bergmann, "Lifetime Imaging Techniques for Optical Microscopy," Lecture, pp. 1–41, 2003.

[94] W. Becker, "The bh TCSPC Handbook,", pp. 1–566, 2010. Found here: https://www.becker-hickl.com/wp-content/uploads/2019/01/bh-TCSPC-Introduction.pdf

[95] C. J. Eling et al., "A Dual-Modal SERS/Fluorescence Gold Nanoparticle Probe for Mitochondrial Imaging," , Chempluschem, 31 Jan 2017, 82(5):674-680

[96] M. T. Clarke et al., "Synthesis of super bright indium phosphide colloidal quantum dots through thermal diffusion," Commun. Chem., vol. 2, no. 1, 2019.

[97] C. J. Eling, T. W. Price, A. R. L. Marshall, and N. Viscomi, "A Dual-Modal SERS / Fluorescence Gold Nanoparticle Probe for Mitochondrial Imaging" Chempluschem, 31 Jan 2017, 82(5):674-680

[98] B. Kasalica, S. Stojadinović, I. Belča, M. Sarvan, L. Zeković, and J. Radić-Perić, “The anomalous sodium doublet D2/D1 spectral line intensity ratio - A manifestation of CCD’s presaturation effect,” J. Anal. At. Spectrom., vol. 28, no. 1, pp. 92–97, 2013.

[99] S. TaMang, S. Lee, H. Choi, and S. Jeong, “Tuning size and size distribution of colloidal InAs nanocrystals via continuous supply of prenucleation clusters on nanocrystal seeds,” Chem. Mater., vol. 28, no. 22, pp. 8119–8122, 2016.

[100] S. Tamang, C. Lincheneau, Y. Hermans, S. Jeong, and P. Reiss, “Chemistry of InP Nanocrystal Syntheses,” Chem. Mater., vol. 28, no. 8, pp. 2491–2506, 2016.

[101] A. K. Gaigalas and L. Wang, “Measurement of the fluorescence quantum yield using a spectrometer with an integrating sphere detector,” J. Res. Natl. Inst. Stand. Technol., vol. 113, no. 1, pp. 17–28, 2008.

[102] M. D. Tessier, K. De Nolf, D. Dupont, D. Sinnaeve, J. De Roo, and Z. Hens, “Aminophosphines: A double role in the synthesis of colloidal indium phosphide quantum dots,” J. Am. Chem. Soc., vol. 138, no. 18, pp. 5923–5929, 2016.

[103] W. S. Song et al., “Amine-derived synthetic approach to color-tunable InP/ZnS quantum dots with high fluorescent qualities,” J. Nanoparticle Res., vol. 15, no. 6, 2013.

[104] K. Kim et al., “Halide-Amine Co-Passivated Indium Phosphide Colloidal Quantum Dots in Tetrahedral Shape,” Angew. Chemie - Int. Ed., vol. 55, no. 11, pp. 3714–3718, 2016.

[105] C. Rivas, G. J. Stasiuk, M. Sae-Heng, and N. J. Long, “Towards understanding the design of dual-modal MR/fluorescent probes to sense zinc ions,” Dalt. Trans., vol. 44, no. 11, pp. 4976–4985, 2015.

[106] F. Le, N. Z. Lwin, J. M. Steele, M. Käll, N. J. Halas, and P. Nordlander, “Plasmons in the metallic nanoparticle-film system as a tunable impurity problem,” Nano Lett., vol. 5, no. 10, pp. 2009–2013, 2005.

[107] Y. Fu, J. Zhang, and J. R. Lakowicz, “Plasmon-enhanced fluorescence from single fluorophores end-linked to gold nanorods,” J. Am. Chem. Soc., vol. 132, no. 16, pp. 5540–5541, 2010.

[108] M. Sawczak et al., “Nanoparticle Over Mirror plasmonic structures prepared with use of Au colloid produced by laser ablation in water,” 19th Int. Conf. Sch. Quantum Electron. Laser Phys. Appl., vol. 10226, p. 102260G, 2017.

[109] L. Z. Hsieh et al., “Metal nano-particles sizing by thermal annealing for the enhancement of surface plasmon effects in thin-film solar cells application,” Opt. Commun., vol. 370, pp. 85–90, 2016.

[110] H. T. Chorsi, Y. Lee, A. Alù, and J. X. J. Zhang, “Tunable plasmonic substrates with ultrahigh Q-factor resonances,” Sci. Rep., vol. 7, no. 1, pp. 1–9, 2017.

[111] S. A. Maier, “Plasmonic field enhancement and SERS in the effective mode volume picture,” Opt. Express, vol. 14, no. 5, p. 1957, 2006.

[112] A. R. L. Marshall et al., “Determining Molecular Orientation via Single Molecule SERS in a Plasmonic Nano-gap,” Nanoscale, pp. 17415–17421, 2017.

[113] H. Lee, G.-H. Kim, J.-H. Lee, N. H. Kim, J.-M. Nam, and Y. D. Suh, “Quantitative Plasmon Mode and Surface-Enhanced Raman Scattering Analyses of Strongly Coupled Plasmonic Nanotrimers with Diverse Geometries,” Nano Lett., vol. 15, no. 7, pp. 4628–4636, 2015.

[114] K. J. Russell, K. Y. M. Yeung, and E. Hu, “Measuring the mode volume of plasmonic nanocavities using coupled optical emitters,” Phys. Rev. B - Condens. Matter Mater. Phys., vol. 85, no. 24, pp. 1–4, 2012.

[115] R. Jurga, F. Della Sala, D. Pisignano, and C. Ciracì, “Enhancement of radiative processes in nanofibers with embedded plasmonic nanoparticles,” Opt. Lett., vol. 41, no. 7, p. 1632, 2016.

[116] V. G. Kravets et al., “Composite au nanostructures for fluorescence studies in visible light,” Nano Lett., vol. 10, no. 3, pp. 874–879, 2010.

[117] M. Kuttge, F. J. García De Abajo, and A. Polman, “Ultrasmall mode volume plasmonic nanodisk resonators,” Nano Lett., vol. 10, no. 5, pp. 1537–1541, 2010.

[118] S. Noda, “Recent progresses and future prospects of two- and three-dimensional photonic crystals,” J. Light. Technol., vol. 24, no. 12, pp. 4554–4567, 2006.

[119] T. Van Der Sar et al., “Deterministic nanoassembly of a coupled quantum emitter-photonic crystal cavity system,” Appl. Phys. Lett., vol. 98, no. 19, pp. 1–4, 2011.

[120] V. M. Apalkov, T. Chakraborty, N. Ulbrich, D. Schuh, J. Bauer, and G. Abstreiter, “Temperature-induced broadening of the emission lines from a quantum-dot nanostructure,” Phys. E Low-Dimensional Syst. Nanostructures, vol. 24, no. 3–4, pp. 272–

277, 2004.

[121] Anthony Peter Edwards, “Optical Properties of Organic plasmonic Devices,” Univ. Hull, no. September, 2015.

[122] A. M. Adawi et al., “Spontaneous Emission Control in Micropillar Cavities Containing a Fluorescent Molecular Dye ”, Advanced materials, pp. 742–747, 2006.

[123] R. Faggiani, J. Yang, and P. Lalanne, “Quenching, Plasmonic, and Radiative Decays in Nanogap Emitting Devices,” ACS Photonics, vol. 2, no. 12, pp. 1739–1744, 2015.

[124] E. Fermi, “Quantum theory of radiation,” Rev. Mod. Phys., vol. 4, no. 1, pp. 87–132, 1932.

[125] A. P. Edwards, A. M. Adawi, A. P. Edwards, and A. M. Adawi, “enhancement Plasmonic nanogaps for broadband and large spontaneous emission rate enhancement,” Journal of Applied Physics 115, 053101 (2014)

[126] P. K. Jain, K. S. Lee, I. H. El-Sayed, and M. A. El-Sayed, “Calculated Absorption and Scattering Properties of Gold Nanoparticles of Different Size, Shape, and Composition: Applications in Biological Imaging and Biomedicine,” J. Phys. Chem. B, vol. 110, no. 14, pp. 7238–7248, 2006.

[127] P. B. Johnson and R. W. Christy, “Optical Constant of the Nobel Metals,” Phys. L Re View B, vol. 6, no. 12, pp. 4370–4379, 1972.

[128] O. Gazzano et al., “Evidence for confined Tamm plasmon modes under metallic microdisks and application to the control of spontaneous optical emission,” Phys. Rev. Lett., vol. 107, no. 24, pp. 4–8, 2011.

[129] John B. Schneider, Understanding the Finite-Difference Time-Domain Method, Chapter 14: Near-to-Far-Field Transformation, (2010).

[130] https://support.lumerical.com/hc/en-us/articles/360034394234-Understanding-frequency-domain-CW-normalization

## Appendix A- LUMERICAL CODES EXAMPLES

In this paragraph we will see some of the fsp scripts used to design, perform FDTD simulations and post processing data extraction.

FAR FIELD PROJECTION

This script works as a post processing data extraction code. It can be recalled as external function too by using the proper % % syntax. Given a monitor name in input, the code calculates the far-field projection for each wavelength and save the results into a MATLAB .mat file.

```
################################################################################
```

```
# FAR FIELD PROJECTIONS

clear.

nonorm; # Remove the CW normalization

run.

# Variables for script recall

monitor="Five_micro_away".

phi=0.

name='FF_VerticalSize_4 nm Five_micro_away'.


#Calculate farfield coordinates in degrees

ux = farfieldux(monitor,1).

uy = farfielduy(monitor,1).

ux_degrees=asin(ux)*180/pi.

uy_degrees=asin(uy)*180/pi.


#Claculate number of frequency points and wavelength vector
```

```
f=getdata(monitor,"f").

f_points=length(f).


lambda=c/f.


#Init FF dataset

E = cell(f_points).


#Finde the calculateed phi point closest to the desired value

n=find (uy_degrees, phi).

E_theta_lambda=matrix(length(ux), f_points).


#Loop over all frequency points and extract E(theta) at fixed angle phi

for (i=1: f_points) {

E{i} = farfield3d (monitor, i).

E_theta_lambda (1: length(ux), i) =E{i}(1:length(ux),n);

}


matlabsave (name, ux, ux_degrees,uy_degrees,E_theta_lambda,E,lambda);


? ("SCRIPT DONE ").


EMAIL NOTIFICATION
```

Some simulations or post-processing codes can take up weeks before completion. As show off, I took the challenge to develop a Matlab script that be recalled by lumerical FDTD to send an email message when a certain process is completed.

```
##########################################################################

# Run a simulation or a post process script


message='MESSAGE TO SEND VIA EMAIL'

matlab #open Matlab

("

mail = 'nanophotonics.simulator@gmail.com'.

recipent=Youremail@yourprovider.com'.

password = 'Your secret password!'.

setpref('Internet','SMTP_Server','smtp.gmail.com').

setpref ('Internet','E_mail', mail).

setpref ('Internet','SMTP_Username', mail).

setpref ('Internet','SMTP_Password', password).

port='465'.

props = java. lang. System.getProperties.

props. setProperty ('mail. smtp. auth','true').

props. setProperty ('mail. smtp. socketFactory.class', 'javax.net.ssl.SSLSocketFactory');

props. setProperty ('mail. smtp. socketFactory.port', port);

sendmail (recipent,'LUMERICAL NOTIFICATION.', message)
```

");

“ONION” STRUCTURE BUILDING EXAMPLE

Cipolla(numberoflayers), onion in Italian, is a function that generates a core shell structure and has the number of layers as argument. The layer filling factor and layer thickness can be specified as well. This code has been used to generate the data for [108] and the work is shown in chapter 4.

```
################################################################

#Cipolla

###############

nl=%numberoflayers%.



tS=9e-9.

tAu=21e-9.

rCore=31e-9.

rAu=0.

rS=0.

R=0.

addstructuregroup.

set("name","cipolla").

set("x",0).

set("y",0).

set("z",0).
```

```
addsphere.

addtogroup("cipolla").

set ("material","Au (Gold) - Johnson and Christy").

set("name","core").

set ("radius”, rCore).

set("x",0).

set("y",0).

set("z",0).



R=rCore+tS.

morder=2.



for(i=1:nl) {



   #Silica

 addsphere.

 set ("override mesh order from material database",1);

 morder=morder+1; # mesh order gold

 set ("mesh order”, morder);
```

```
set("name","Silica").
addtogroup("cipolla").

set ("radius", R);    # Radius shell
set("x",0).
set("y",0).
set("z",0).
#set ("material","Au (Gold) - Johnson and Christy").
set("index",1.5).

##### Add gold thickness
R=R+tAu.
#Gold

addsphere.
set ("override mesh order from material database",1).
morder=morder+1.
set ("mesh order",morder);

set("name","Au").
addtogroup("cipolla").
```

```
set ("material","Au (Gold) - Johnson and Christy");

set("radius”, R);

set("x",0).

set("y",0).

set("z",0).



##Reset Radius for silica shell



R=R+tS.









}
```

## APPENDIX B- NEAR TO FAR FIELD MATLAB ANALYSYS CODE

```
clear all; clc;close all

%% Reference
% vert ref
load ('C:\Users\francesco.viscomi\Desktop\test code DBR bands\data\disk\Vacuum
Reference\Ref Vertical\FFrefV nm One_micro_away.mat');
% Horizontal ref
%load ('C:\Users\francesco.viscomi\Desktop\test code DBR bands\data\disk\Vacuum
Reference\Ref Horizontal\FFrefH nm One_micro_away.mat')

ref=E_theta_lambda.
refinte=trapz(ref).
%% Ref spectral interp
load('C:\Users\francesco.viscomi\Desktop\lumoyellowinterp.mat').
```

```
%% Report bit
d=dir ();
import mlreportgen. report.*
import mlreportgen.dom. *

report = Report('FATTICAZZITUA','docx').
t=cell(numel(d),2);   % Allocates table dimension for images to put in the document
figusize='3in'.


main=cd.

%%
imcont=1.
for k=3: numel(d)

   cd(d(k).name).
   %
   [filepath, fname, ext] = fileparts(d(k).name); % getfolder name
   %%
   m=dir('*.mat').
   for i=1: length(m)
      for j=1:1


            clf
            %farfieldplotnorm(m(i).name, ref);
            farfieldintegrate(m(i).name, refinte,vq1);
            sdf('francesco')
            fig = Figure(gcf).
            t{imcont,1} = Image(getSnapshotImage(fig, report));
            t{imcont,1}. Width = figusize;
            t{imcont,1}. Height = figusize;

         imcont=imcont+1.




   end

   end
   cd(main)

end


%% Report adding
tt = Table(t).
tt. Border = 'none';
tt. TableEntriesInnerMargin = '5pt';
add (report, tt);
```

```
close(report).
rptview(report)

% %%
%
%
function farfieldplotnorm(dataset, ref)

load(dataset).
[filepath, fname,ext] = fileparts(cd);     % folder name
[filepath, name,ext ] = fileparts(dataset); % file name
w=lambda. *1e9;
norm=E_theta_lambda. /ref;
norm=(norm*vq1).
%surf(w, ux_degrees,E_theta_lambda);  % Real plot
surf(w, ux_degrees,norm);            % Norm plot
view (2);shading interp;axis tight
colormap(jet (1024))
colorbar
% caxis ([0 1.1e-43])
%   caxis ([0 150])
a=gca.
a. XTick=a.XLim(1):50:a.XLim(2);
a. XLim=[400 800];

xlabel ('Wavelength (nm)');ylabel('Angle (Degrees)')
titolo=replace (name,'_',' ');
titol=strcat(fname,'-', titolo);
title(titol)
end



%
function farfieldplot(dataset)

load(dataset).
[filepath, fname,ext] = fileparts(cd);     % folder name
[filepath, name,ext ] = fileparts(dataset); % file name
w=lambda. *1e9;
norm=E_theta_lambda.
%surf(w, ux_degrees,E_theta_lambda);  % Real plot
surf(w, ux_degrees,norm);            % Norm plot
view (2);shading interp;axis tight
colormap(jet (1024))
colorbar
% caxis ([0 1.1e-43])
%   caxis ([0 150])
a=gca.
a. XTick=a.XLim(1):50:a.XLim(2);
a. XLim=[400 800];

xlabel ('Wavelength (nm)');ylabel('Angle (Degrees)')
```

```
titolo=replace (name,'_',' ');
titol=strcat(fname,'-', titolo);
title(titol)
end


function farfieldintegrate(dataset, ref,vq1)

load(dataset).
[filepath, fname,ext] = fileparts(cd);     % folder name
[filepath, name,ext ] = fileparts(dataset); % file name
w=lambda. *1e9;
norm=bsxfun (@rdivide, E_theta_lambda, ref);
norm=norm. *vq1';
%surf(w, ux_degrees,E_theta_lambda);  % Real plot
surf(w, ux_degrees,norm);            % Norm plot
view (2);shading interp;axis tight
colormap(jet (1024))
colorbar
axis ([450 700 -65 65])


xlabel ('Wavelength (nm)');ylabel('Angle (Degrees)')
titolo=replace (name,'_',' ');
titol=strcat(fname,'-', titolo);
%title(titol)
end
```